# FAULT DIAGNOSIS ON A THREE-PHASE INDUCTION MOTOR USING EXTENDED PARK VECTOR APPROACH

BY

IGOCHE, Sunday Enejo

MEng/SEET/2018/8390

DEPARTMENT OF ELECTRICAL AND ELECTRONICS ENGINEERING,

SCHOOL OF ELECTRICAL ENGINEERING AND TECHNOLOGY,

FEDERAL UNIVERSITY OF TECHNOLOGY MINNA, NIGER STATE.

June 2023

# FAULT DIAGNOSIS ON A THREE-PHASE INDUCTION MOTOR USING EXTENDED PARK VECTOR APPROACH

BY

IGOCHE, Sunday Enejo

MEng/SEET/2018/8390

A THESIS SUBMITTED TO THE POSTGRADUATE SCHOOL FEDERAL UNIVERSITY OF TECHNOLOGY MINNA, NIGERIA IN PARTIAL FULFILLMENT OF THE REQUIREMENTS FOR THE AWARD OF THE MASTER OF ENGINEERING (M.ENG) DEGREE IN ELECTRICAL AND ELECTRONIC ENGINEERING (POWER SYSTEM ENGINEERING OPTION).

June 2023

# DECLARATION

I hereby declare that this thesis titled: "**Fault Diagnosis on a Three-phase Induction Motor Using Extended Park Vector Approach**" is a collection of my original research work and it has not, to the best of my knowledge, been presented for any other qualification anywhere. All sources of information (published and unpublished) have been duly acknowledged by means of references.

IGOCHE, Sunday Enejo                                        ……………………………

MEng/SEET/2018/8390                                    SIGNATURE/DATE

FEDERAL UNIVERSITY OF TECHNOLOGY

MINNA, NIGERIA

# CERTIFICATION

The thesis titled: "**Fault Diagnosis on a Three-phase Induction Motor Using Extended Park Vector Approach**" by: Igoche Sunday Enejo (MEng/SEET/2018/8390) meets the regulations governing the award of the degree of MEng of the Federal University of Technology, Minna and it is approved for its contribution to scientific knowledge and literary presentation.


ENGR. PROF. B. A. ADEGBOYE                          …….………………...
MAJOR SUPERVISOR                                    Signature and Date



ENGR. DR ODUNAYO IMORU                              …….………………...
CO-SUPERVISOR                                       Signature and Date



ENGR. DR. L. OLATOMIWA                              …….………………...
HEAD OF DEPARTMENT                                  Signature and Date



ENGR. PROF. E.N ONWUKA                              …….………………...
DEAN OF SCHOOL OF ELECTRICAL                        Signature and Date
ENGINEERING AND TECHNOLOGY



ENGR. PROF. O. K. ABUBAKRE                           …….………………...
DEAN OF POSTGRADUATE                                Signature and Date
SCHOOL

# ACKNOWLEDGEMENTS

# ABSTRACT

As a need to reduce cost and minimise losses associated with downtime, early fault diagnosis in Induction Motors (IM) has become necessary for more reliable, efficient and productive industrial maintenance practices. This research is based on the Extended Park Vector Approach (EPVA) in diagnosing one of the earliest manifestations of stator faults - stator Inter-Turn Short Circuit (ITSC) fault. The conventional EPVA maintains the record among many other techniques as best in isolating load oscillation harmonics from incipient short circuit faults. However, the conventional EPVA uses frequency spectra analysis that requires complex computations and signal processing expertise for the interpretation of results. The EPVA technique used in this research maximized the advantage of the Park Vector Modulus (PVM). To diagnose faults, the PVM data were plotted as Park Vector Plot (PVP) and the visualized distortion was used to diagnose ITSC faults. Furthermore, the severities of faults were studied using means, variance, standard deviation and Root Mean Square Error (RMSE) as performance metrics to determine how much the ITSC occurrence in the IM has caused deviation from the original healthy state (when there is no ITSC). The research was simulation-based. The mathematical model of a three-phase IM with variable winding parameter, $m$, was designed and simulated in a MATLAB environment. The winding parameter, $m$, was varied from 0% − 10% to demonstrate different levels of ITSC fault severity. The datasets of winding currents were obtained and used in the EPVA for fault diagnoses. Furthermore, the impacts of faults on the torque, speed and Park currents were studied. The result shows that ITSC faults introduced AC ripples signals in the IM that were visibly seen on the speed, torque and currents waveforms. The result also shows that ITSC faults gradually prolonged the transient time from 0.7s at 0% fault operation to more than 3s at 9% − 10% ITSC faults under no load condition. It also shows that ITSC faults induced negative torques in the IM that affect the motor operation quadrant. The PVP distortion accurately detected and reflected the severity of ITSC faults in the IM. The plots of the means, variance, standard deviation and RMSE show how progressively, the ITCS faults caused deviations in the IM. The RMSE was more accurate to point to the ITSC level that could cause total failure in the IM which is at 6% and 5% under no load and 5 Nm load respectively. The study of ITSC fault in IM using the mathematical model was successful.

# TABLE OF CONTENTS

**APPENDICES**

# LIST OF TABLES

# LIST OF FIGURES

# ABBREVIATIONS

| | |
|---|---|
| AE | Acoustic Emission |
| AMB | Active Magnetic Bearing |
| ANFIS | Adaptive Neuro-Fuzzy Inference System |
| ANN | Artificial Neural Network |
| DE | Dynamic Eccentricity |
| DFT | Discrete Fourier Transform |
| DQ | Direct-Quadrature |
| DWT | Discrete Wavelet Transform |
| EPVA | Extended Park Vector Approach |
| EPRI | Electric Power Research Institute |
| FEM | Finite Element Method |
| FEPVA | Filtered Extended Park Vector Approach |
| FL | Fuzzy Logic |
| FFT | Fast Fourier Transform |
| FPVA | Filtered Park Vector Approach |
| IEEE | Institution of Electrical and Electronics Engineers |
| IM | Induction Motor |
| ITSC | Inter-turn Short Circuit |
| MCSA | Motor Current Signature Analysis |
| NSDP | Negative Sequence Differential Protection |
| RMSE | Root Mean Square Error |
| PCA | Principle Component Analysis |
| PVA | Park Vector Approach |
| PVM | Park Vector Modulus |

| | |
|---|---|
| PVP | Park Vector Plot |
| SE | Static Eccentricity |
| STFT | Short Time Fourier Transform |
| SVM | Support Vector Machines |
| TTF | Turn-to-Turn Fault |

<center>**CHAPTER ONE**</center>

**1.0**          **INTRODUCTION**

**1.1      Background to Study**

Induction Motors (IM) are the workhorse of power generation stations and processing industries. Statistically, Mustafa (2015) reported that more than 80% of electromechanical conversions in industrial drive applications employ the induction machine. This statistic has increased up to 95% in recent years due to the extreme penetration of new emerging technologies like lift systems, wind power generation, electric washing machines, and electrical-powered transportation systems (Irfan *et al.*, 2015; Mani *et al.*, 2021; Yang *et al.*, 2015). Some of the characteristic features that make IM more suitable for industrial applications are low cost, longer durability, high reliability, simplicity, ruggedness and easy maintainability. IM are electrical machines that inert flux in their corresponding coils by electromagnetic induction. The three-phase IM does not require field windings or DC voltage for excitations, making these electrical machines simpler in design and energy efficient at a lower cost.  Most commercial and household appliances like electric pumps and fans use these machines for their diverse operations. Hence, the occurrence of failure in these machines affects a wide area of human affairs, causes great economic losses and cripples many engineering processes resulting in downtime.

As reported by Imoru *et al.,* (2018), the financial burden for maintenance and repairs of industrial equipment averaged about 50% of total industrial expenditures annually. Fault diagnosis, therefore, is an optimal priority in other to cut costs, minimise losses, and ensure a safer operation of IM. Also, maintenance operations can be more decisive and productive on a ground of a good diagnostic process.

<center>1</center>

In recent years, diagnostic operations have become incorporated into the operational systems of IM. Some IM characteristic parameters have been employed to develop several diagnostic techniques to have good and reliable diagnostic techniques. Parameters such as currents (Choqueuse and Benbouzid, 2015; Gangsar and Tiwari, 2017; Han *et al.*, 2019), stray flux (Ishkova and Vítek, 2016; Panagiotou *et al.*, 2018; Ramirez-Nunez *et al.*, 2018), instantaneous power factor (Akar and Gercekcioglu, 2017) and harmonic index of the fault frequencies (Burriel-Valencia *et al.*, 2017; Gyftakis *et al.*, 2020; Sapena-Bano *et al.*, 2015) have been used to diagnose faults in IM. Also, machine learning techniques have been reportedly used to enhance the automated diagnosis of faults in IM (Ali *et al.*, 2019; Imoru *et al.*, 2021; Jia *et al.*, 2016; Lashkari *et al.*, 2015; Razavi-Far *et al.*, 2018; Wen *et al.*, 2017). Some of the techniques developed on these accounts have been found to express strength in some kinds of faults and highly unreliable results in others.

Also, the operating conditions (whether steady or transient state) of the machine have been found to have significant effects on the techniques used (Gritli *et al.*, 2017). However, as reported in the experiment conducted on thirteen (13) widely known and used techniques, the Extended Park Vector Approach (EPVA) was reported as the second-best reliable technique in diagnosing faults and the best in diagnosing faults of low magnitude (Gyftakis *et al.*, 2017). The EPVA is more suitable to differentiate emerging faults from transient load oscillation conditions that may occur in the machine due to high starting torque (Hameed *et al.*, 2016). This has given great credit to the EPVA techniques in IM condition monitoring since most IM faults start as incipient faults of low magnitude.

The EPVA technique is fundamentally based on the Park Vector Approach (PVA) but with an advanced spectral analysis using soft signal processing to analyse the Park Vector Modulus (PVM). With the PVM analysis, the result from the PVA is more efficient and

reliable (Cruz and Cardoso, 2001). EPVA utilises the IM's current parameters to diagnose various kinds of faults in the IM. As a result, it is an online diagnostic technique that does not interfere with machine operations (Mostafaei *et al.*, 2018).

Theoretically, a fault presence in an IM distorts the Park Vector Plot (PVP) in the direct-quadrature (*dq*) plane, resulting in an elliptical plot. The degree of distortion is directly proportional to the magnitude of the fault. In this research, the EPVA technique was used to diagnose winding faults in an IM and used to develop indices to appropriately check the level of fault severity in the IM.

## 1.2 Statement of the Research Problem

Induction motors are prone to fault due to their frequent and continuous use in industrial applications (Gyftakis and Cardoso, 2017). Several effective techniques have been proposedly used to diagnose these faults in condition monitoring operations. These methods rarely comprise computation of the severity of these faults (Bouras *et al.*, 2018; Corne *et al.*, 2018; Hameed *et al.*, 2016). There is a need to compute the severity of these faults as indicative of the extent to which the faults have caused a deviation from the normal healthy state of the IM. This research is targeted towards the computation of fault severity corresponding to occurring faults by maximizing the advantage of the visualized Park vector plot using EPVA. This entails the diagnosis of faults using the Park Vector Plot (PVP) and the computation of the Park Vector Modulus (PVM) corresponding to each diagnosis. These values were used to compute the deviation, dispersion, and correlation of the datasets in comparison to the healthy state of the motor to measure the severity of the fault in the motor.

**1.3   Aim and Objectives**

The research aims to diagnose faults in a three-phase induction motor using EPVA.

The objectives of this research are:

i.   To mathematically model a three-phase induction motor using dynamic mathematical equations.

ii.  To simulate the mathematical model of a three-phase induction motor using MATLAB R2019a.

iii. To analyse the torque, speed and winding currents of the simulation model.

iv.  To diagnose the winding fault using the Park vector plot and mathematically compute the PVM.

v.   To measure the severity of the fault using the deviation, dispersion and correlation of the PVM as performance metrics

**1.4   Research Justification**

For every engineering design and application, the primary purpose is to ease work done at maximum efficiency, minimise cost and ensure the safety of lives and equipment. Induction machines of no doubt make the engineering process of electromechanical conversions in industrial electrical drives easy. Hence, they are essential components of generation plants and processing companies. However, they are prone to faults that are incipient and in the long run result in catastrophic damages, pose threats to lives and cause substantial financial losses.

The financial burden for maintenance and repairs of industrial equipment averaged about 50% of total industrial expenditures annually as reported (Imoru *et al.*, 2018). To minimize these financial losses and ensure a safer working environment, it is important

to carry out diagnostic testing on industrial induction machines for early checks of possible faults developing in the machines. Also, it has become increasingly necessary to optimize the maintenance operations associated with fault diagnosis as most induction machine failures are due to poor maintenance practices. A diagnostic technique that can gauge the level of severity of diagnosed faults will help guide operatives on the choice to make during maintenance operations.

Considering the vastly available techniques used for diagnosing faults, it is more suitable to use EPVA for its non-invasiveness, simplicity and efficiency. It is also one of the best techniques that can be used to appropriately compare the severities of the faults and distinguish between the types of faults. The choice of MATLAB for this research is because it is a good engineering software with the appropriate tools for modelling and analyses in real-time processes.

## 1.5    Scope of Research

The study covers the diagnosis of inter-turn short circuit (ITSC) winding faults in a three-phase IM and the computation of the deviation and correlation of the diagnosed faults with respect to the healthy IM. It shows how to model and simulate the operation of a three-phase induction motor in MATLAB. The study demonstrates how to transform the phase currents into the Park's Vector currents and properly diagnose the presence of ITSC fault. It further covers how to use the simulations to measure and analyse the PVPs which were used to compute the deviation and correlation of each diagnosed fault.

# CHAPTER TWO

## 2.0                        LITERATURE REVIEW

Fault diagnosis is a condition monitoring process that is used to detect the presence of a fault and identify the type of fault in the machine. Fault diagnosis uses the deviation in values of the induction machine's characteristic properties or parameters to detect and identify faults (Mustafa, 2015). The effects of faults in induction machines have resulted in many manifestations such as decreased efficiency, unbalanced phase currents and voltages, pulsation in torque and speed, unbalanced eccentricity, and overheating of the machine (Bhattacharyya *et al.*, 2015). In this chapter, the concept, types, causes and effects of faults in induction machines are discussed. The reviews of major diagnostic methods used in diagnosing faults with the unique signature associated with them are also highlighted. Furthermore, the advantages and limitations of various diagnostic methods are highlighted. This chapter ended with a chapter summary.

## 2.1    Concepts, Causes and Effects of Faults in Induction Machines

A fault is defined as an unpermitted deviation of at least one characteristic property or parameter of the system from the acceptable, usual and standard condition (Mustafa, 2015). IMs are designed to operate within an acceptable limit or value of their parameters or characteristics. The importance of such design consideration is to have a precise controlling system associated with the machine and to determine what system the machine can be used in, based on the predicted output required. Therefore, there are diverse sizes of IMs based on different values of their rated parameters needed for a particular operation. At normal operation, it is, therefore, expected that IMs operate within their rated characteristics properties or parameters. Any unpermitted deviation from these limits or values is an indication of a fault's presence (Mustafa, 2015).

Faults in IMs start as build-up or emerging faults as the machine is constantly subjected to electrical, magnetic, thermal, environmental and mechanical stresses (Al-Deen *et al.*, 2018; Gyftakis and Cardoso, 2017). Stresses cause deterioration, wear and tear of the machine components and eventually result in machine fault and failure. These stresses result from possible manufacturing defects, poor installation, poor working environment, deterioration of components and ineffective schedule maintenance (Sadeghi *et al.*, 2017). Some of the major causes of faults in induction machines as reviewed are manufacturing defects, imbalance in phase voltages, phase over-supplied voltage, magnetic over fluxing; improper installation, contamination of lubricant, misalignment of the shaft, shaft overloading, under-supplied voltages, and poor maintenance (Choudhary *et al.*, 2019).

Due to the various causes of induction machine faults, several faults originate within and outside of the IM framework that directly affects the performance. These faults can be grouped as internal and external faults. Based on the nature of a fault, internal and external faults could be further categorized as mechanical, electrical, electromagnetic and environmental faults as shown in Figure 2.1 (Choudhary *et al.*, 2019)
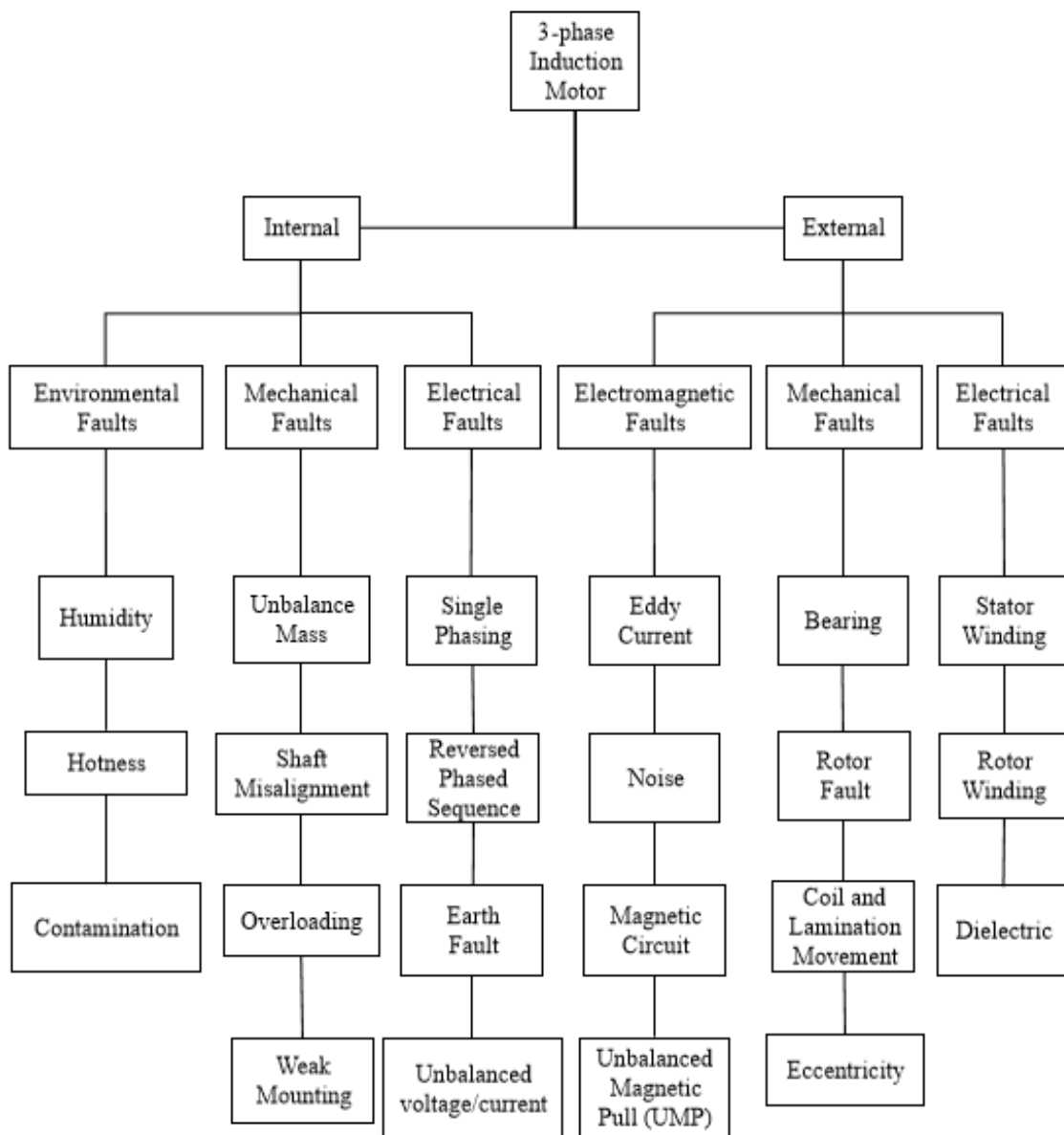
**Figure 2.1:** Categories of faults in induction motors and their classifications

(Choudhary *et al.*, 2019).

## 2.2    Overview of the Common Types of Faults in IM

Several studies have categorised the most common faults in IM as stator faults, rotor faults, bearing faults and other faults (air-gap eccentricity) based on the major components affected (Amanuel *et al.*, 2021; Sarikaya *et al.*, 2019). In studying the magnitude of these common faults in a medium-voltage IM, the Institution of Electrical

and Electronics Engineers (IEEE) and the Electric Power Research Institute (EPRI) presented a statistic that shows that bearing and stator related faults are the most common types of IM faults as shown in Figure 2.2 (Agyare *et al.*, 2019).

Further studies by Zhang *et al* (2011); Nandi *et al* (2005); and Tavner (2008) as shown in Figure 2.3, indicate that the magnitude of the faults in various components of IM also dependent on the voltage size of the machine.

The statistics further revealed that mechanical faults are significantly high in low-voltage IM, where bearing faults contributed 75% of total machine faults as compared to medium- and high-voltage induction machines which are 44% and 13% respectively. While faults of electrical nature, such as stator-related faults increase gradually as the voltage level of the machine increases. This is due to an increase in the electrical and thermal stresses as the voltage level of the machine increases (Zhang *et al.*, 2011).

Another possible cause of the variations is the strength of the materials used in the manufacturing of the machine's components. Gyftakis and Cardoso (2020), have reported that the use of sleeve bearings in large machines, reduces the degradation process, compared to the rolling element bearings applied in low and medium-voltage induction machines (Gyftakis and Cardoso, 2020). This account for the reduced bearing faults in high-voltage IM.
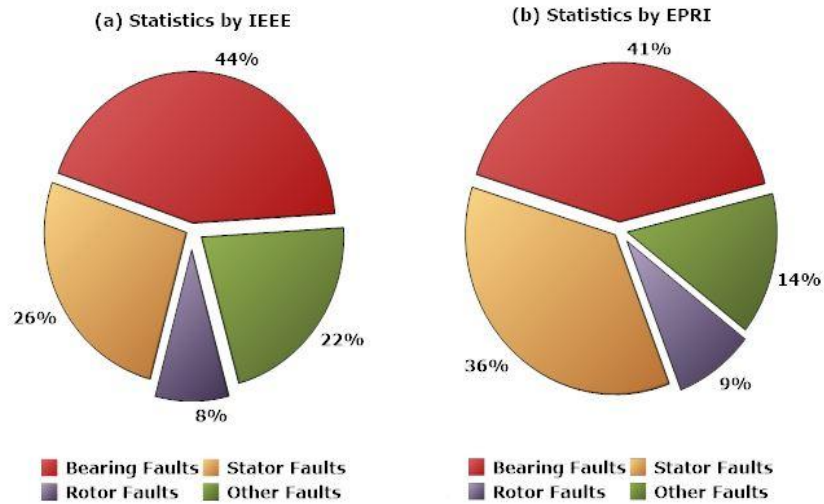
**Figure 2.2:** Percentage (%) component of IM failure in medium IM by IEEE and

EPRI (Agyare *et al.*, 2019)
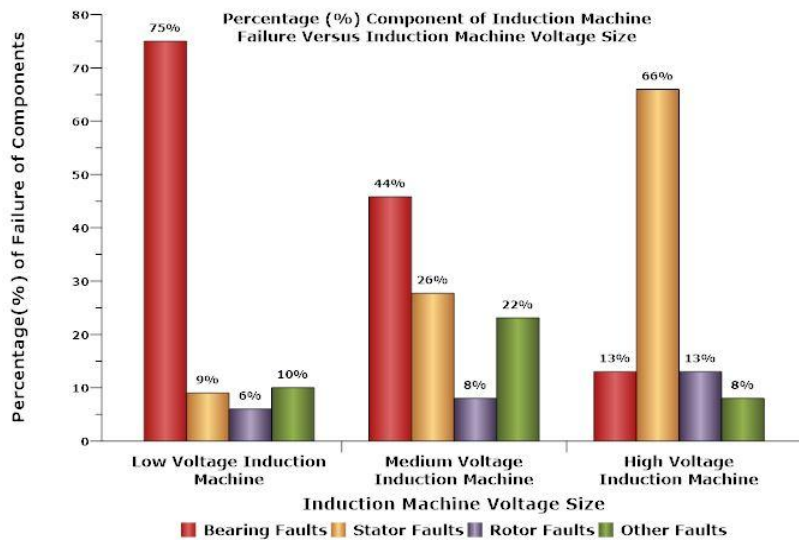


**Figure 2.3:** Magnitude of faults in IM in correlation to machine sizes (Nandi *et al.*,

2005; Tavner, 2008; Zhang *et al.*, 2011)

### 2.2.1   Bearing related faults

Bearings are important components of an induction machine. They are made of an inner

and outer race, separated by rotating metallic balls and cages that are furnished in a ring-

like structure as shown in Figure 2.4.
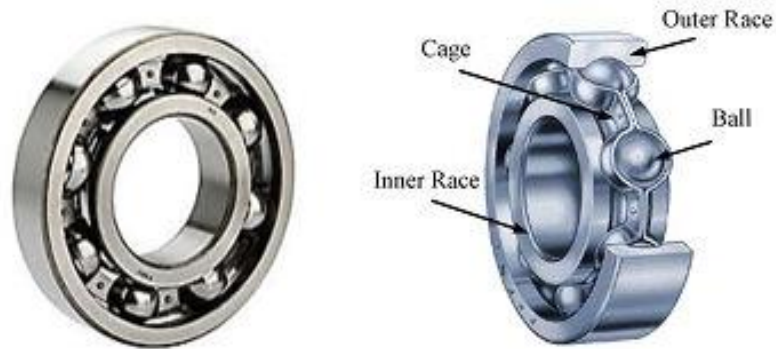
**Figure 2.4:** Structural section of a bearing (Yadav *et al.*, 2013)

Bearings are used primarily as supports for the rotating shafts of the rotor fixed at both ends of the shafts (Bharti *et al.*, 2020). They are essential for the rotating mechanical system of the induction machine to be fully operational. They create allowance between the rotating components (rotor) and the stationary components (stator and stator cage) to reduce friction and make mechanical movement easy (Jung *et al.*, 2017). Bearing faults are the most common faults in three-phase IM. The statistics presented by IEEE and EPRI show that bearing-related faults range from 40 – 44% of total faults in medium voltage IM. Research has also revealed that this fault can increase up to 90% of total faults in small-size IM (Jiang *et al.*, 2017; Kompella *et al.*, 2018). Bearing faults are seen as bearing corrosion, wear debris on either the inner race or outer race and defects in the ball cage (Malla and Panigrahi, 2019).

Bearing failure could be localized or distributed (Irfan, 2019; Liu and Shao, 2018). Bearing failure has been reported as the major cause of rotor deterioration (Önel and Benbouzid, 2008). Therefore, an early diagnosis of bearing faults is necessary to prevent distributed fault effects on other components.

Some of the highlighted causes of bearing fault or failure are under/over lubrication causing abrasive and overheating, misalignment of bearing and rotor shaft,

11

contamination, moisture presence leading to corrosion, overloading of the shaft, the vibration of the machine due to poor mounting increasing shear stress in bearing, and manufacturing defect (Kudelina *et al.*, 2021; Malla and Panigrahi, 2019; Ozigis *et al.*, 2021).



**Figure 2.5:** Manifestation of bearing faults

Vibration monitoring, current monitoring, acoustic monitoring and lubrication analysis have all been used as good signals to diagnose bearing faults (Chandra and Rao, 2019; Liu *et al.*, 2020; Poddar and Tandon, 2019; Wang *et al.*, 2019). Vibration monitoring has been identified as the best and most sensitive condition monitoring in diagnosing bearing faults (Stief *et al.*, 2019).

### 2.2.2 Rotor related faults

The IM rotor is the rotating part of the IM that drives other external loads. The rotor bar could be wound type (that is, containing windings) or cage type. Most small-size IMs are made of wound-type and cast cage rotors while large machines are made of fabricated cage rotors (Sharma *et al.*, 2018). Rotor faults contribute to about 10% of total IM faults (Halder *et al.*, 2022). The manifestation of rotor faults is seen in broken rotor bars, cracked rotor bars, bent rotor bars, damaged rotor winding and lamination (Anish Kumar *et al.*, 2022; Antonino-Daviu *et al.*, 2020; Singh, 2019). The effects of these faults are seen in the reduced performances of the machine such as reduced, and pulsating speed and torque, vibrations of the machine, and arcing in the rotor.

Rotor faults are majorly due to faults distribution from other components of the IM like bearing. Studies have shown that bearing faults majorly contribute to rotor deterioration (Liu *et al.*, 2022). Other causes of rotor faults are due to thermal stress, overloading of the rotor shaft, mass unbalances, manufacturing defects, and UMP (Gangsar and Tiwari, 2020; Sheikh *et al.*, 2022).

### 2.2.3 Stator related faults

Stator Faults are majorly classified as stator winding faults and stator core faults. Stator winding faults have been reported as the major stator fault in IM (Maraaba *et al.*, 2018; Verma *et al.*, 2018). ITSC faults are the early manifestation of stator winding faults (Afshar *et al.*, 2019; Pietrzak and Wolkiewicz, 2021b). As a result, short circuit current recycles within the coil, building up excessive heat that may lead to other distributed faults like coil-to-coil faults, phase-to-phase faults and phase-to-ground faults of higher magnitude. Such high magnitude faults have being reported to be the cause of stator core

faults and other machine failures like open circuit, causing an abrupt shutdown of the machine (Singh, 2019).

It has been reported that the initial cause of winding faults is due to winding insulation breakdown (Ashok *et al.*, 2021; Pietrzak and Wolkiewicz, 2021a). Other causes are slacking of the coil and excessive surge current or voltage in the coil leading to burns. These effects lead to inter-turn faults, hotspots, open circuits and possible burns.

### 2.2.4    Air-gap eccentricity faults

Air-gap eccentricity fault is a type of mechanical fault that is rotational axis related. It creates a non-uniform air gap between the stator and the rotor. In a healthy machine, the axis of rotation of the machine rotor will be in alignment with the rotor and stator axes as shown in Figure 2.6a.
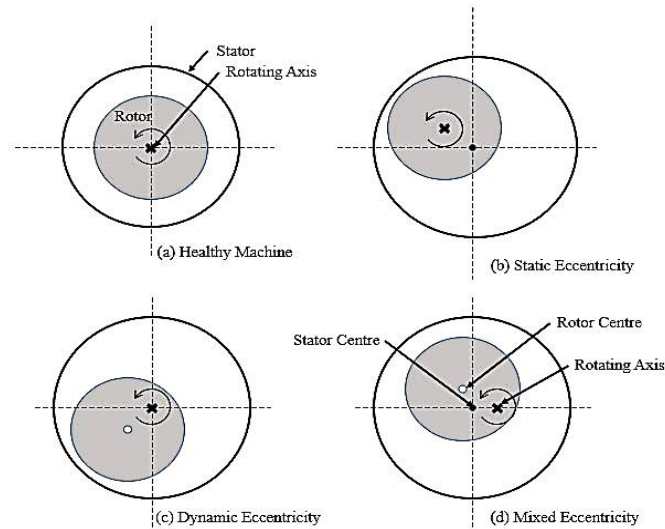


**Figure 2.6:** Types of eccentricity in induction machines (Faiz and Moosavi, 2016)

In this case, the centre of rotation, the rotor and the stator centres are the same (or aligned) making the air gap (or air space) between the rotor and the stator uniform. Any deviation that causes the misalignment of the centre of rotation from either the rotor or stator axes

or both results in one of these types of eccentricity faults as shown in Figures 2.6b, 2.6c and 2.6d.

Static Eccentricity (SE) fault is when the axis of rotation correlates with the centre of the rotor but is misaligned from the stator centre. The rotor will rotate about the rotor axis but shifted from the centre of the stator (Aggarwal and Strangas, 2019), thereby creating an unbalanced air gap that is fixed in the machine. In this case, the rotor will be tilted closer to one side of the stator than the other, however, that position remains fixed even when rotating (Mirzaeva and Saad, 2018).

Dynamic Eccentricity (DE) fault is when the axis of rotation correlates with the centre of the stator but is misaligned from the rotor centre. The rotor will rotate about the stator axis but not in its centre. This will create an unbalanced air gap that is constantly changing from side to side between the stator and the rotor. Some of the causes of DE are related to torque oscillation faults like bearing faults, rotor misalignment, and rotor faults (Shin *et al.*, 2021). Faiz and Moosavi, (2016), deduced that this is because DE eccentricity and torque oscillation normally occur simultaneously. It has also been reported that about 80% of many mechanical faults (bearing faults, rotor misalignment, mass unbalance, and rotor faults) eventually lead to eccentricity faults (Nath *et al.*, 2021).

## 2.3    Fault Diagnosis in IM

As earlier stated in section 2.0, fault diagnosis is a condition monitoring process that uses deviation in the machine's characteristic parameters or properties to identify the presence of faults based on a reference signature pattern. IM characteristics such as winding voltages (Alloui *et al.*, 2022) and currents (Burriel-Valencia *et al.*, 2018a), torque (Gyftakis *et al.*, 2013; Hemamalini, 2018), instantaneous power factor (Akar and Gercekcioglu, 2017), instantaneous power (Irfan *et al.*, 2017), harmonics index (Sapena-

Bano *et al.*, 2018; Sapena-Bano *et al.*, 2016), eccentricity property (Sadeghi *et al.*, 2017) have been successfully used in past researches to diagnose faults in induction machine. The common diagnostic techniques used in monitoring machine parameters to diagnose the common types of faults are; vibration monitoring, acoustic emission monitoring, motor current signature analysis, air-gap torque monitoring, infrared thermography, artificial neural network, fuzzy logic, adaptive neuro-fuzzy inference system and support vector machines (Choudhary *et al.*, 2019; Malla and Panigrahi, 2019; Wang *et al.*, 2019). A few of these techniques are briefly discourse below.

## 2.3.1 Vibration monitoring

All IMs have vibration signatures external or internal to the machine during operation (Gangsar and Tiwari, 2019). Vibration monitoring is based on the vibration analysis of the vibration signature of the motor as it operates. This monitoring technique has been reviewed as one of the best and most effective techniques in monitoring mechanical-related faults (De Sousa *et al.*, 2019; Salameh *et al.*, 2018). This technique uses vibration sensors to capture raw vibration signals as the motor is in operation. To extract the fault vibration signal, signal processing analyses such as Short Time Fourier Transform (STFT), Discrete Wavelet Transform (DWT), and Fast Fourier Transform (FFT) are used (Ali *et al.*, 2019). The signals are used to generate vibration spectrum. Vibration signal are manifested as frequency, acceleration or phase displacement. For healthy motor, the IM produces weak vibration and for faulty motor, the IM generate high vibration signal.

The limitation of using this monitoring technique is the cost associated with the purchase of vibration sensors. This makes this technique one of the most costly condition-monitoring techniques (Li *et al.*, 2019; Ostachowicz *et al.*, 2019).

### 2.3.2 Acoustic emission monitoring

The sounds produced by IM as the result of the vibration of the machine have been used in diagnosing a fault in the motor (AlShorman *et al.*, 2021). This process is called Acoustic Emission (AE) monitoring. The process of diagnosing faults using AE monitoring requires transducers to sense emitted sounds (Appana *et al.*, 2018). These acquired sound data are combined with audible frequency monitoring techniques to produce high frequencies (about 100 kHz to 1MHz) which can be analysed for faults (Salameh *et al.*, 2018). Therefore, AE monitoring requires a good understanding of acoustics and frequency processing techniques.

The limitation of this method is that background noise is part of the noise components captured by the transducers and this affects the accuracy of this technique (AlShorman *et al.*, 2021; Beale *et al.*, 2020). Compared with other techniques, AE monitoring is regarded as less efficient (Choudhary *et al.*, 2019).

### 2.3.3 Motor current signature analysis

Motor Current Signature Analysis (MCSA) is a current signal-based technique. It is the most popular technique for diagnosing windings faults. In most industrial IM applications, current and voltage data are constantly and easily measured. These data are used as parameters to diagnose faults in the IM. MCSA monitoring technique is therefore easy to implement and cost-effective. The current and voltage data are used to develop a power spectrum which can be analysed for fault. MCSA has been combined with many signal-processing techniques for further improvement in efficiency (Drakaki *et al.*, 2020). It is also a good technique that has been combined with other machine-learning techniques to develop automated diagnosing techniques (Quabeck *et al.*, 2021; Sunal *et al.*, 2022).

As reported by Marzebali *et al*., (2018) mechanical faults do appear as electrical signals and can be used to diagnose the corresponding mechanical faults in the machine using MCSA (Marzebali *et al.*, 2018). MCSA is now used in monitoring mechanically developed faults like bearing faults, broken rotor faults and misalignment.

### 2.3.4    Machine learning monitoring techniques

In modern IM monitoring techniques, a more computational technique that involves machine learning models (or algorithm) are used to automate the diagnostic process (Burriel-Valencia *et al.*, 2018b). Machine learning techniques rely on other techniques to acquire data on IM parameters. Then the system is trained to learn patterns within the data and act when the pattern is abnormal. Such machine learning techniques that are commonly used are Artificial Neural Networks (ANN), Fuzzy Logic (FL), Adaptive Neuro-Fuzzy Inference System (ANFIS) and Support Vector Machines (SVM) (Altaf *et al.*, 2018; Chouidira *et al.*, 2021; Mohamed *et al.*, 2021; Wang *et al.*, 2020). Each of these learning techniques has its advantages and disadvantage which affects the effectiveness and accuracy of their implementations.

### 2.4    Diagnostic–Based Maintenance Operation

One major goal of carrying out fault diagnosis is to optimize the maintenance stage of condition monitoring. Formerly, industrial machine maintenance was based on schedule maintenance (which is periodically carried out at a stipulated time) and maintenance due to an abrupt system failure (Kumar *et al.*, 2018).

These two ways of system maintenance result in larger costs if the system is allowed to fail or develop a serious stage of faults before they are addressed. Therefore, to reduce the cost of repairs associated with scheduled maintenance and prevent total failure of the

system, it is needful as a matter of necessity, to always carry out constant fault diagnosis on the machine to help in the early detection of emerging faults within the machine framework or components. Therefore, IM maintenance based on diagnosis is a recommendation to prevent failure and reduce losses and costs as shown in Figure 2.7.
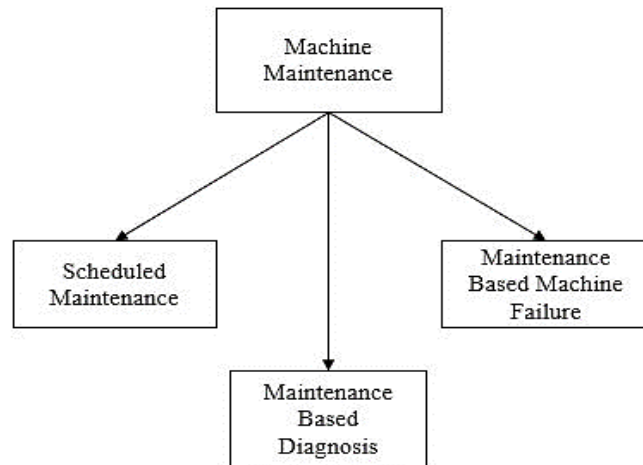


**Figure 2.7:** Induction motor maintenance (Choudhary *et al*., 2019)

Furthermore, the choice of diagnostic techniques largely depends on the simplicity, cost, effectiveness and accuracy of the technique. EPVA as widely reported is the second best widely used fault diagnostic technique and the best for diagnosing low-level faults (Gyftakis and Marques-Cardoso, 2019). Therefore, for emerging faults, the EPVA proves to be an acceptable choice. In this research, the EPVA technique is adopted to develop computational indices that appropriately check for the level of fault severity.

## 2.5    Related Works on EPVA Techniques

Alaoui *et al*., (2015), worked on an extended Park vector for the detection of inter-turns faults in an induction motor. The research was based on the detection of inter-turn faults in IM during the transient operation of the motor. According to the report, most diagnostic techniques detect faults during steady-state operation, however, induction motors do not

always operate completely under steady-state conditions. The research, therefore, used the EPVA to detect inter-turn faults in the induction motor during transients operation.

The study was conducted both simulation-based and experimental-based. To achieve the simulation, the induction motor was modelled mathematically in the stationary reference frame with an insulation failure resistance, depicting the insulation breakdown during inter-turn fault occurrence. The stator currents were extracted from the stator frame reference (stationary reference frame) and were converted to the rotor frame reference using the Park transformation equations. These Park transformed stator currents were plotted in MATLAB to study the Lissajous forms (PVP) for inter-turn faults of 5% and 10%. The experimental test rig was set up for the same machine parameters used for the simulation. The stator inter-turn fault was created on one of the stator windings by shorting it at 5% and 10% of the turns. And the stator currents were extracted through measurement for further analysis.

The results of the Lissajous form for both simulation and experimental studies show that the plot is circular when there is no fault. For 5% fault, the shape of the Lissajous (PVP) form has a thick circumference. And for 10% shorted turns, the thickness is greater. To demonstrate the severity of each shorted inter-turn fault, a comparison between the 5% and 10% shorted turns was obtained by plotting the stator currents of the stator reference frame. The result shows that at 10%, the Lissajous shape is more elliptical and wider in magnitude than the 5% inter-turn fault (Alaoui *et al.*, 2015).

The research proved that the EPVA technique can be used to study inter-turn faults in the transient states by observing the Lissajous form. However, the research did not provide any numerical computation or data to help compute the fault severity. Also, it fails to

prove the effectiveness of using insulation breakdown resistance in the machine model in diagnosing faults at a lower percentage of shorted turns.

Oliveira and Cardoso, (2016), conducted a study on transformer turn-to-turn faults protection methods. The study compared the performance of the negative sequence component method and the performance of the space vector protection algorithms in detecting several internal and/or external fault conditions. The authors highlighted the limitation of the conventional differential protection scheme used for transformer protection as unable to detect low-level turn-to-turn faults since such protection schemes only operate at pre-set values of about 20-25 % rated currents. The solution is to use protection schemes that can detect inter-turn faults at lower magnitudes and this study compared the negative sequence component and the space vector protection algorithms.

The negative sequence was based on the theory that during inter-turn faults, there is an asymmetry in the three-phase currents that manifest as the negative sequence components. By monitoring this manifestation, the detection of fault was achieved. In the space vector method, the monitoring of the second harmonic frequency ($2f$) that occurred during faults was used to achieve the detection of faults. As executed by the authors, in both methods turns ratio compensation, vector group adaption and zero-sequence component filtering were applied to the primary- and secondary sides for differential current computation. In the negative sequence method, Discrete Fourier Transform (DFT) was used to extract the fundamental components and the Fortescue transformation was used to determine the symmetric components. Under this method, the negative sequence of the primary or secondary is compared to a predefined threshold of about 4% of rated currents. If they exceed this threshold, the angle between them was used to determine if the resulting fault is an external or internal fault. In the space vector algorithm, the EPVA

was used to extract the Park vector current components and the DFT algorithm was used to transform the Park modulus into a frequency spectrum. For this method, the spectra were analysed for AC signals that occurred at 2*f* of the fundamental frequency. And in the case of no fault, a pure DC signal was seen.

Both methods were tested in simulation using a derived transformer model and by experiment using a three-phase, two-winding, core-type, 10.3 kVA, 230/132 V transformer connected to a current transformer (CT) for winding currents extraction and protection. The shorted turn was achieved by connecting a short resistor to the fault windings. This system was tested under varying conditions: balanced load with turn-to-turn fault, unbalanced load with turn-to-turn fault, external fault with turn-to-turn and unbalanced supply voltage with turn-to-turn fault.

The result shows that both methods have similar sensitivity to highly severe inter-turn faults. However, the EPVA is about 14% more sensitive in detecting low-level turn-to-turn faults in the transformer. It also revealed that EPVA has a better advantage in discriminating between external and internal faults (Oliveira and Cardoso, 2016). The research proved very successful, however, no numerical computation was given to compute the severity of the faults in the transformer using EPVA. Also, the use of DFT has more lagging time than other signal processing algorithms like Fast Fourier Transform (FFT). It is indicative that the result of this research can be further improved.

To reduce the high number of frequency spectrum computations employed in the EPVA for the detection of faults in induction motors, Hameed *et al*, 2016, suggested the combined use of Park's Vector Approach (PVA) and Principle Component Analysis (PCA) for detection of faults in a synchronous machine.

The research was simulation-based using real datasets of a synchronous machine. The misalignment of the rotor shaft was studied as the reference fault. To use the PVA, the two phase currents obtained from the datasets were averaged to get the third phase current. Fault currents obtained from the datasets were injected at the 100,000th sample. The Park transformation was applied to obtain the Lissajous pattern of the currents. The shapes of the Lissajous pattern were observed. In the case of no fault, the shape formed a perfectly circular pattern and during faults, the shape observed was distorted. The PCA was further used to create a standard model and then process monitoring statistics were used to check any deviation from the standard model. The result of the PCA shows that when there is no fault in the motor, the principal value is within the threshold of the standard model. And when fault data are injected into the model, the principal value exceeded the model threshold (Hameed *et al.*, 2016).

The combined methods significantly improved computational time. However, studies have shown that the EPVA yields better results in differentiating broken bar faults from load oscillation and is also a better technique in fault detection under low load operation (Pezzani *et al.*, 2010). Therefore, it employed a higher number of frequency spectrum computations (Hameed *et al.*, 2016). The use of a calculated third-phase current does not give a realistic approach to the research. Also, the research failed to estimate the severity of the misalignment and the sensitivity of the method to low-level misalignment could not be ascertained.

Gyftakis *et al*, (2017), introduced the Filtered Park's Vector Approach (FPVA) and the Filtered Extended Park's Vector Approach (FEPVA) to resolve the unreliability of the PVA in detecting broken rotor bars in IM. The study reported that the conventional PVA uses the thickness of the Park circumference in diagnosing broken rotor bars faults and is

unreliable because PVA depends on the magnetic poles and the number of rotor slots. The study proposed the combined use of FPVA and FEPVA to resolve this issue and provide a low computational diagnostic method for broken rotor bars detection.

The FPVA implemented involves monitoring the three-phase currents of the windings. The currents are used to calculate the Park Vector current components. The elliptic filter was used to filter frequencies greater than 370 Hz and the notch filter was used to filter the fundamental frequency at 50 Hz leaving the fundamental fault components along with other harmonics. The result obtained from this process was used as the first indication of faults. The output of the notch filter was used to compute the Park modulus. And the spectral of the Park modulus was analysed using FFT to further diagnose the severity of the fault by measuring the amplitude of the higher harmonics. This study was investigated using Finite Element Method (FEM) simulation and through experimental testing on a 3-phase, 4-pole, 4 kW, 400 V induction motor with 24, 28, 30, 40, 41 and 48 rotor slots each having one broken rotor bar.

The results show that due to the use of elliptic and notch filters, only faults harmonics and other harmonics were observed on the circumference when there is a fault. And in the absence of fault, the circumference of the Park plot only indicated other harmonics with hollowed centres making this method to be able to discriminate between fault conditions and other conditions that produce harmonic signals. Also, the applied filters made the frequency spectral clearer for better analysis. The results satisfactorily proved the reliability and effectiveness of the combined FPVA and FEPVA over PVA  (Gyftakis *et al.*, 2017). However, the results were still dependent on the number of rotor slots and to measure severity, there must be complex FFT computation.

Sharma *et al*, (2017), proposed a novel Park's vector approach for the investigation of incipient stator fault in three-phase squirrel cage induction motors. The study was an experimentally based research using a 0.75 horsepower modified squirrel cage induction motor. The inter-turn fault was created in the motor by shorting the modifiable phase at the 13th, 23rd and 30th turn corresponding to 2.2%, 4% and 5.1% turn. The mechanical loading system was loaded at 40% and 80%. The three-phase currents were measured using a setup of CT and a current measurement module. The entire setup was connected to a PC through the NI-DAQ card. The measured phase currents were transformed to Park current components using LabVIEW graphical program. The obtained values were normalized and plotted using the XY graph.

The observed XY graph corresponded to the Lissajous pattern. The results show that the graph is perfectly circular when there is no fault and elliptical when a fault occurs in the motor. The shape produced similar results when the motor was loaded at 40% and 80%.

The research further developed an index based on the ratio of the distance from the centre to the circumference in the xy axes of the Lissajous pattern. The sine inverse of this ratio was plotted and used to estimate the fault severity of the inter-turn fault in the motor. It was reported that during faults, this value decreases as the fault percentage increases. Also, the loading of the motor further decreases the value of this index (Sharma *et al.*, 2017).

Although the applied PVA technique used was able to diagnose the inter-turn fault and estimate the fault severity level based on the developed index, it still could not resolve the original challenges of PVA in terms of insensitivity to low-level faults and is unable to differentiate between load oscillation and transient conditions.

Corne *et al*, (2018), studied the reflection of bearing faults on the stator currents in an induction machine using EPVA.

The research was experimental-based using a test rig of an 11kW induction machine. To model mechanical faults in the machine, the mechanical drive-end-side bearing was replaced by an Active Magnetic Bearing (AMB). By adjusting the AMB, different rotor movements were achieved to demonstrate the case of single-point outer race bearing, single-point inner race bearing and bearing cage problems. The relation between the mechanical fault severity and the spectral signature of the Park modulus was studied.

The result shows that bearing faults of any type result in the presence of all bearing fault characteristic frequencies in the spectrum of the Park modulus. The study proved successful and confirmed that evolving bearing faults are reflected in the stator current, and stator current analysis of faults in IM can become the most effective condition monitoring technique in investigating mechanical faults (Corne *et al.*, 2018). However, the research did not provide further information on how to estimate fault severity in the machine. Also, the research used complex spectral computation which is a limitation in terms of quick and easy diagnosis.

Bouras *et al,* (2018) worked on the prediction of the mass unbalance of a variable speed induction motor by carrying out the analysis of the stator currents using multiple combined techniques. The authors experimented to check for the reliable detection of mass unbalance and changes in its severity if, by the necessity of service, the induction motor is subjected to a speed variation.

The multiple techniques reported involved the use of Park orbit to identify the distortion and the use of Fourier transforms (STFT and FFT) to help identify the type of degradation. The authors reported that external mechanical faults create torque oscillation that affects

the sinusoidal wave pattern of the stator currents. These currents were measured from an experimental test rig on a 270W, 220/380V induction motor using current sensors. The motor was also attached to a speed aviator to regulate the speed at a lower frequency of $35 - 25$ Hz. The stator currents were captured and using MATLAB, the spectra were analysed with FFT and STFT. Also, the experimental test rig was tested with unbalanced load of 50g. The characteristic frequency induced for such case of unbalanced load were studied.

The results show that the presence of an unbalanced mass induced frequencies that appeared on either side of the fundamental frequency (50 Hz). The research also reported that the amplitude of these frequencies measured in dB increases as the speed were reduced to $35 - 25$ Hz (Bouras *et al.*, 2018). The research has shown that the combined use of Park Vector and Fourier transforms was able to successfully identify faults at low frequency and minimal load. However, the research failed to compute the severity associated with the diagnosed faults and there was no further report on the criticality of the faults diagnosed.

Many other studies have been carried out in detecting turn-to-turn faults (TTF) in transformer windings using negative sequence components and EPVA (Farzin *et al.*, 2019; Meira *et al.*, 2018; Mostafaei *et al.*, 2018).

Farzin *et al*, (2019) carried out an experimental study to evaluate the performance of negative sequence and space vector-based methods in detecting transformer turn-to-turn faults. The transformer under different operating conditions such as normal operation, no-load operation, external phase faults and open conductor faults was studied.

To investigate the performance of NSPD and EPVA-based methods, some experimental tests were carried out on a three-phase 2kVA, 400/400 V, 50 Hz, three-leg core

transformer, with designed resistor taps on both HV and LV sides. By taping through 1-25% of the turns, different turn-to-turn faults were introduced. The currents were measured using 6 CTs and digital storage scope. DFT was further used to extract the current phasors.

The results show that to prevent fault trip of the NSDP- and EPVA-based methods for external faults, a proper and fixed security count of the TTF detection characteristic curve has to be determined. It also stated that this security count is difficult to have a fixed setting and it can endanger the reliability and secure performance of the protection scheme. For a low-level fault at 1%, the NSPD and EPVA-based methods were able to identify the fault after 16.2ms and 19.4ms, respectively (Farzin *et al.*, 2019). The research was very successful, however, the use of DFT required complex computation.

Gyftakis and Marques-Cardoso, (2019), proposed a method for the detection of inter-turn stator faults in induction machines at a very low severity level, which other classical methods have proved incapable and unreliable in detecting.

The author has reported that most conventional techniques diagnose fault at level high enough to cause the failure of the machine. The research proposed the detection of faults less than 1% (that is, at 0.25%, 0.50% and 0.75%). The proposed method relied on the measurement of stray flux in the machine when a short circuit fault occurs. An experimental test bed was set up using a 4kW 380V induction machine. One of the windings was modified to allow for the injection of shorted turns using switches. Three stray flux sensors positioned at 120 degrees were used to accurately capture the stray flux data. For each shorted turn, the stray flux was captured and the stator and short circuit current were measured using multimeters and current clamps. The PVA was applied to calculate the Park flux components of the stray flux.

The author reported that the Park plots of the raw calculated Park flux components were blurry and unreliable. To filter these results, an elliptic filter was used at 60 Hz and 160 Hz cut-off frequencies. The result shows that the Park flux components with filtered frequencies, was elliptical in cases of fault. And better visualize elliptical shapes are seen for 160 Hz. This technique proved that the PVA detected faults at lower fault severity (less than 1%). However, the use of filters and the need for accurate placement of flux sensors at 120 degrees makes it highly susceptible to inaccuracies. Also, the experimental set up needed for data capturing makes the system cumbersome for application.

From the foregoing review, it becomes obvious that the EPVA technique has recorded many successes in the field of fault diagnosis. However, these methods rarely comprise computation of the severity of these faults. Hence, there is a need to compute the severity of these faults as indicative of the extent to which the faults have caused a deviation from the normal healthy state of the IM. This research is targeted towards the computation of the fault severity corresponding to occurring faults by maximizing the advantage of the visualized PVP using EPVA. This entails the diagnosis of faults using the shape of the PVP and the measurement of the PVM corresponding to each diagnosis. These values were used to compute the deviation, dispersion and correlation of the PVM as the measured fault severity.

## 3.0          RESEARCH METHODOLOGY

This chapter presents the methodology adopted for this research in the diagnosis of faults in IM using the EPVA technique. Detailed descriptions of the methodological steps were presented and the flow chart was also presented. Figure 3.1 presents the overview of the research methodology.
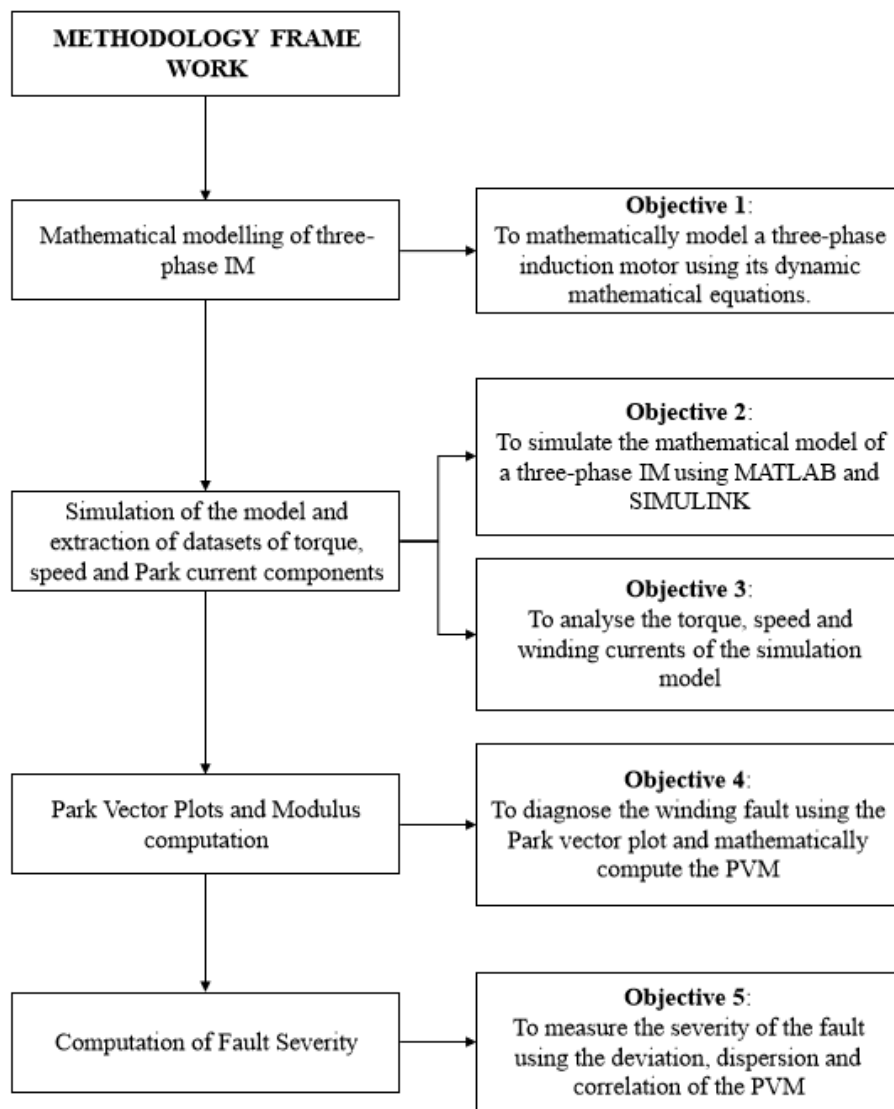


**Figure 3.1:** Block diagram of research methodology framework.

## 3.1      Mathematical Modelling of an ITSC Fault in a Three-phase Induction Motor

The mathematical model of a three-phase IM is described by the voltages, currents, flux linkages, speed and torque equations. Mathematical modelling is best required to accurately analyse the dynamic and steady-state performances of the motor such that a variation of any of its characteristics properties can accurately reveal its impact on the performance of the motor.

Normally, IM is modelled in the ABC reference frame system, however, for research using the EPVA which is built on the conventional Park Vector Approach, there is a need to transform the modelling to the Park vector reference frames systems. The sequence of transformation is illustrated in Figure 3.2.
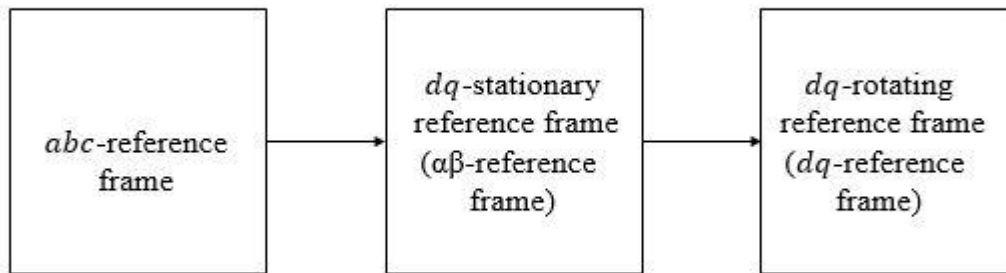


**Figure 3.2:** Transformation sequence from $abc$ to $dq0$ system

An ITSC fault is a fault condition as a result of insulation breakdown leading to contacts of the stator windings. For this research, it is assumed:

     i.    The three-phase system is a balance and uniform system.

     ii.    The induction motor has identical sinusoidal distributed windings displaced from each at 120 degrees.

     iii.   The ideal state of the motor is considered, that is, the effect of saturation, eddy current, friction and winding losses are neglected.

31

iv. The motor has a uniform air gap between the stator and the rotor cores.

v. Higher harmonics are neglected. (Ratnani and Thosar, 2014; Samir *et al.*, 2008)

### 3.1.1 Mathematical modelling of an ITSC fault in ABC reference frame system

Consider a three-phase squirrel cage induction motor with an ITSC fault on the a-phase stator windings supplied by a three-phase voltage, $v_a$, $v_b$ and $v_c$ as shown in Figure 3.3.
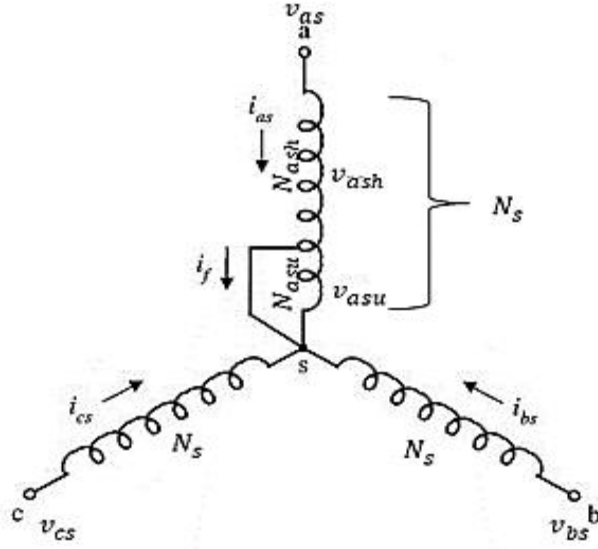


**Figure 3.3:** ITSC fault on a stator winding

Where,

$N_{asu}$, numbers of shortened $a$–phase stator windings,

$N_{ash}$, numbers of unshortened $a$–phase stator windings,

$i_f$, the circulating fault currents flowing in the shorted resistive path.

$i_{as}$, the current flowing through the healthy stator windings of the $a$–phase.

Using Kirchhoff Current Law (KCL), the current flowing through the shorted-turns, $i_{asu}$, is expressed as:

$$i_{asu} = i_{as} - i_f \qquad (3.1)$$

32

By symmetrical three-phase winding, the number of windings on each phase is equal. Therefore, the stator and rotor resistances are respectively equal.

The total number of turns, $N_s$ on the stator a–phase winding is expressed in terms of shortened turns, $N_{asu}$, and unshortened turns, $N_{ash}$ as:

$$N_s = N_{ash} + N_{asu} \qquad (3.2)$$

Similarly, the total resistance, $R_s$ on the stator a-phase winding is expressed in terms of the resistance, $R_{asf}$ on the shortened winding and the resistance, $R_{ash}$ on the unshortened winding as:

$$R_s = R_{ash} + R_{asf} \qquad (3.3)$$

During ITSC faults, the current in the a-phase circulates in the shortened turns, creates hot-spot and causes further insulation breakdown.

Let $m$ represent the ratio of shortened turns to the total number of turns $\left(\text{that is, } m = \frac{N_{asu}}{N_s}\right)$ then, the ratio of unshortened turns to the total turns is expressed as:

$$\frac{N_{ash}}{N_s} = \frac{N_s - N_{asu}}{N_s} = 1 - m \qquad (3.4)$$

By interpolation, the resistance of the shortened and unshortened turns expressed in terms of $m$ are $mR_s$ and $(1 - m)R_s$ respectively.

### 3.1.1.1 Voltage equations

As described by Krause *et al.*, (2013), the general voltage equations for a three-phase squirrel-cage IM under normal operating condition is expressed as (Krause *et al.*, 2013):

$$v_{abcs} = R_s i_{abcs} + \rho \psi_{abcs} \qquad (3.5)$$

$$0 = R_r i_{abcr} + \rho\psi_{abcr} \qquad (3.6)$$

where $v_{abcs}$ is a matrix of supplied voltages on the stator *abc* windings, $i_{abcs}$ is the matrix of the corresponding stator *abc* windings currents, $\psi_{abcs}$ is the matrix of the corresponding flux linkages of the stator *abc* windings, $i_{abcr}$ is the matrix of the rotor currents on its corresponding *abc* windings, $\psi_{abcr}$ is the matrix of the corresponding flux linkages of the rotor *abc* windings, $R_r$ is the rotor windings resistance and $\rho$ is the derivative with respect to time.

In the case of ITSC fault, the voltage equation is expressed as:

$$v'_{abcs} = R'_s i'_{abcs} + \rho\psi'_{abcs} \qquad (3.7)$$

$$0 = R_r i_{abcr} + \rho\psi'_{abcr} \qquad (3.8)$$

where $v'_{abcs}$ is the matrix of supplied voltages on the stator *abc* winding during ITSC fault, $i'_{abcs}$ is the matrix of the stator currents on its corresponding *abc* windings during ITSC fault, $\psi'_{abcs}$ is the corresponding flux linkage matrix during ITSC fault on the stator *abc* windings and $R'_s$ is the stator resistance during ITSC fault.

The matrices of voltages, currents and flux linkage can be defined as:

$$v'_{abcs} = [v_{ash} \quad v_{asu} \quad v_{bs} \quad v_{cs}]^T \qquad (3.9)$$

$$i'_{abcs} = [i_{as} \quad i_{as} - i_f \quad i_{bs} \quad i_{cs}]^T \qquad (3.10)$$

$$i_{abcr} = [i_{ar} \quad i_{br} \quad i_{cr}]^T \qquad (3.11)$$

$$\psi'_{abcs} = [\psi_{ash} \quad \psi_{asu} \quad \psi_{bs} \quad \psi_{cs}]^T \qquad (3.12)$$

$$\psi'_{abcr} = [\psi_{ar} \quad \psi_{br} \quad \psi_{cr}]^T \qquad (3.13)$$

$$R'_s = R_s \text{diag}[1 - m \quad m \quad 1 \quad 1] \qquad (3.14)$$

34

$$R_r = R_r \text{diag}[1 \quad 1 \quad 1] \tag{3.15}$$

where,

$v_{ash}, v_{asu}$ are voltages across shortened turns and unshortened turns of the $a$-phase of the stator winding respectively,

$v_{bs}, v_{cs}$ are voltages across the $b$- and $c$-phase of the stator windings respectively,

$i_{bs}, i_{cs}$ are currents flowing through the $b$- and $c$-phase stator windings respectively,

$i_{ar}, i_{br}, i_{cr}$ are currents flowing through the $a$-, $b$- and $c$-phase of the rotor windings respectively,

$\psi_{ash}, \psi_{asu}$ are flux linkages in the shortened and unshortened turns of the $a$-phase of the stator windings respectively.

$\psi_{bs}, \psi_{cs}$ are flux linkages in the $b$- and $c$-phase of the stator windings respectively.

$\psi_{ar}, \psi_{br}$ and $\psi_{cr}$ are flux linkages in the $a$-, $b$- and $c$-phase of the rotor windings respectively.

Substituting (3.9) – (3.15) in (3.7)

$$\begin{bmatrix} v_{ash} \\ v_{asu} \\ v_{bs} \\ v_{cs} \end{bmatrix} = R_s \begin{bmatrix} 1-m & 0 & 0 & 0 \\ 0 & m & 0 & 0 \\ 0 & 0 & 1 & 0 \\ 0 & 0 & 0 & 1 \end{bmatrix} \begin{bmatrix} i_{as} \\ i_{as} - i_f \\ i_{bs} \\ i_{cs} \end{bmatrix} + \rho \begin{bmatrix} \psi_{ash} \\ \psi_{asu} \\ \psi_{bs} \\ \psi_{cs} \end{bmatrix} \tag{3.16}$$

Adding row (1) and (2) of equation (3.15), the voltage equations of the IM with a shorted $a$-phase are expressed as:

$$v_{abcs} = R_s i_{abcs} + \rho \psi_{abcs} + m U_1 i_f \tag{3.17}$$

$$0 = R_r i_{abcr} + \rho \psi_{abcr} \tag{3.18}$$

where the matrix $U_1$ is expressed as:

$$U_1 = [-R_s \quad 0 \quad 0]^T \tag{3.19}$$

### 3.1.1.2 Flux linkages

The matrix expression for the stator and rotor flux linkages under an ITSC fault is given as (Tallam *et al.*, 2002):

$$\begin{bmatrix} \psi'_{abcs} \\ \psi_{abcr} \end{bmatrix} = \begin{bmatrix} L'_{ss} & L'_{sr} \\ L'_{rs} & L_{rr} \end{bmatrix} \begin{bmatrix} i'_{abcs} \\ i_{abcr} \end{bmatrix} \tag{3.20}$$

Where $L'_{ss}$ and $L_{rr}$ are the stator and rotor winding self-inductances matrices due to their respective winding currents. $L'_{sr}$ and $L'_{rs}$ are the stator and rotor winding mutual inductances matrices due to the corresponding current flowing in other windings.

As given by (Sang-Hoon, 2017), the expression for the inductance between two windings $x$ and $y$ can be described by the expression:

$$L_{xsys} = \frac{N_{xs}N_{ys}L_{ms}\cos\alpha}{N_s{}^2} \tag{3.21}$$

Where $L_{xsys}$ is the inductance between the *xs* and *ys* windings, $N_{xs}$ and $N_{ys}$ are the number of turns in the *xs* and *ys* windings respectively, $\alpha$ is the angular displacement between the two windings, and $L_{ms}$ is the mutual flux linkage between the windings.

When $x = y$, it results in a self-inductance and $\alpha = 0°$ and when $x \neq y$, it results in mutual inductance and $\alpha$ is shifted through angle $0°, 120°$ or $240°$ depending on the axis of the corresponding winding.

Using equation (3.21) to solve for the self-inductances and mutual inductances, $L'_{ss}, L_{rr}, L'_{rs}$ and $L'_{sr}$ is given in equations (3.22), (3.23) and (3.24).

$$L'_{ss} = L_{ls} \begin{bmatrix} 1-m & 0 & 0 & 0 \\ 0 & m & 0 & 0 \\ 0 & 0 & 1 & 0 \\ 0 & 0 & 0 & 0 \end{bmatrix} + L_{ms} \begin{bmatrix} (1-m)^2 & m(1-m) & -0.5(1-m) & -0.5(1-m) \\ m(1-m) & m^2 & -0.5m & -0.5m \\ -0.5(1-m) & -0.5m & 1 & -0.5 \\ -0.5(1-m) & -0.5m & -0.5 & 1 \end{bmatrix} \qquad (3.22)$$

$$L_{rr} = \begin{bmatrix} L_{lr} + L_{ms} & -0.5L_{ms} & -0.5L_{ms} \\ -0.5L_{ms} & L_{lr} + L_{ms} & -0.5L_{ms} \\ -0.5L_{ms} & -0.5L_{ms} & L_{lr} + L_{ms} \end{bmatrix} \qquad (3.23)$$

$$L'_{sr} = {L'}_{rs}{}^{T} = L_{ms} \begin{bmatrix} (1-m)cos\theta_r & (1-m)cos\left(\theta_r + \frac{2\pi}{3}\right) & (1-m)cos\left(\theta_r - \frac{2\pi}{3}\right) \\ mcos\theta_r & mcos\left(\theta_r + \frac{2\pi}{3}\right) & mcos\left(\theta_r - \frac{2\pi}{3}\right) \\ cos\left(\theta_r - \frac{2\pi}{3}\right) & cos\theta_r & cos\left(\theta_r + \frac{2\pi}{3}\right) \\ cos\left(\theta_r + \frac{2\pi}{3}\right) & cos\left(\theta_r - \frac{2\pi}{3}\right) & cos\theta_r \end{bmatrix} \qquad (3.24)$$

Where $L_{ls}$ and $L_{lr}$ are the self-inductance due to the corresponding self-currents flowing in the stator and rotor windings respectively. $L_{ms}$ is the mutual inductance in the stator windings due to currents flowing in adjacent windings and $\theta_r$ is the rotor winding angular displacement.

Substituting equations (3.22) – (3.24) in equation (3.20) and adding row (1) and (2) of the resulting equations.

$$\psi_{abcs} = L_{ss}i_{abcs} + L_{sr}i_{abcr} + mU_2i_f \qquad (3.25)$$

$$\psi_{abcr} = L_{rs}i_{abcs} + L_{rr}i_{abcr} + mU_3i_f \qquad (3.26)$$

Where,

$$U_2 = [-(L_{ls} + L_{ms}) \quad 0.5L_{ms} \quad 0.5L_{ms}]^T \qquad (3.27)$$

$$U_3 = -L_{ms} \left[cos\theta_r \quad cos\left(\theta_r + \frac{2\pi}{3}\right) \quad cos\left(\theta_r - \frac{2\pi}{3}\right)\right]^T \qquad (3.28)$$

### 3.1.2 Mathematical modelling of ITSC fault in stationary DQ reference frame system

The flux linkages of the $abc$ IM model contain time-varying mutual inductances seen in the alternating values of $\theta_r$ in equation (3.24). The $DQ$ reference frame transformation reduces the complexity of the IM model by transforming the time-varying parameters into an orthogonal system (Sang-Hoon, 2017).

For any three-phase system, the transformation to an orthogonal stationary DQ reference frame is given by the generic equation:

$$\begin{bmatrix} v_\alpha \\ v_\beta \end{bmatrix} = \frac{2}{3} \begin{bmatrix} 1 & -\frac{1}{2} & -\frac{1}{2} \\ 0 & \frac{\sqrt{3}}{2} & -\frac{\sqrt{3}}{2} \end{bmatrix} \begin{bmatrix} v_a \\ v_b \\ v_c \end{bmatrix} \tag{3.29}$$

where $v_\alpha$ and $v_\beta$ are the two orthogonal $dq$ stationary alpha- and beta-phase systems respectively, and $v_a$, $v_b$ and $v_c$ are the three-phase $abc$ corresponding system.

Applying the stationary $dq$ reference frame (Clarke transformation), equations (3.16) and (3.17) become:

$$v_{\alpha\beta s} = R_s i_{\alpha\beta s} + \rho \psi_{\alpha\beta s} - \frac{2}{3} m R_s i_f \tag{3.30}$$

$$0 = R_r i_{\alpha\beta r} + \rho \psi_{\alpha\beta r} + \omega_r \begin{bmatrix} 0 & 1 \\ -1 & 0 \end{bmatrix} \psi_{\alpha\beta r} \tag{3.31}$$

Where

$v_{\alpha\beta s}$ is a matrix of alpha- and beta-phase supplied voltage of the stator winding of the stationary $dq$ orthogonal system.

$i_{\alpha\beta s}$ and $i_{\alpha\beta r}$ are the currents matrices of the stator and rotor windings in the stationary $dq$ orthogonal system respectively.

$\psi_{\alpha\beta s}$ and $\psi_{\alpha\beta r}$ are the flux linkage matrices of the stator and rotor in the stationary $dq$ orthogonal system respectively.

$\omega_r$, is the rotor speed.

From equation (3.16), the voltage drop across the shorted windings, $v_{asu}$ in stationary $dq$ is expressed as:

$$v_{\alpha su} = mR_s(i_{\alpha s} - i_f) + \rho\psi_{\alpha su} \qquad (3.32)$$

where $i_{\alpha s}$ is the alpha-phase current and $\psi_{\alpha su}$ is the flux linkage in the alpha-phase shorted turns.

However, the voltage across a short circuit is zero, therefore, $v_{\alpha su} = 0$. Hence,

$$\rho\psi_{\alpha su} = -mR_s(i_{\alpha s} - i_f) \qquad (3.33)$$

Solving for the value of flux linkages in equations (3.30), (3.31) and (3.33)

$$\psi_{\alpha s} = \int (v_{\alpha s} - R_s i_{\alpha s} + \tfrac{2}{3}mR_s i_f)dt \qquad (3.34)$$

$$\psi_{\beta s} = \int (v_{\beta s} - R_s i_{\beta s})dt \qquad (3.35)$$

$$\psi_{\alpha r} = \int (-\omega_r\psi_{\beta r} - R_r i_{\alpha r})dt \qquad (3.36)$$

$$\psi_{\beta r} = \int (\omega_r\psi_{\alpha r} - R_r i_{\beta r})dt \qquad (3.37)$$

$$\tfrac{1}{m}\psi_{\alpha su} = \int -R_s(i_{\alpha s} - i_f)\, dt \qquad (3.38)$$

Where $\psi_{\alpha s}$ and $\psi_{\beta s}$, are respective alpha- and beta-phase flux linkages in the stator windings of the stationary $dq$ system, $\psi_{\alpha r}$ and $\psi_{\beta r}$ are respective alpha- and beta-phase fluxes linkages in the rotor windings of the stationary $dq$ system. $i_{\beta s}, i_{\alpha r}$ and $i_{\beta r}$ are the

beta-phase current in the stator winding, alpha-phase current in the rotor winding and beta-phase current in the rotor winding in the stationary $dq$ system respectively.

Applying the stationary $dq$ reference frame transformation to equations (3.25) and (3.26) to eliminate time-varying mutual inductances, the expressions become:

$$\psi_{\alpha\beta s} = L_s i_{\alpha\beta s} + L_m i_{\alpha\beta r} - \frac{2}{3} m L_s i_f \tag{3.39}$$

$$\psi_{\alpha\beta r} = L_r i_{\alpha\beta r} + L_m i_{\alpha\beta s} - \frac{2}{3} m L_m i_f \tag{3.40}$$

Where $L_m = \frac{3}{2} L_{ms}$, $L_s = L_{ls} + L_m$ and $L_r = L_{lr} + L_m$

Also, the flux linkage of the shorted windings is described by the equation (Dongare *et al.*, 2020).

$$\psi_{\alpha su} = m L_s i_{\alpha s} + m L_m i_{\alpha r} - m \left( L_{ls} + \frac{2}{3} m L_m \right) i_f \tag{3.41}$$

Solving for the value of $i_{\alpha s}$, $i_{\beta s}$, $i_{\alpha r}$, $i_{\beta r}$ and $i_f$ in equation (3.39) – (3.41).

$$i_{\alpha s} = \frac{L_r \psi_{\alpha s} - L_m \psi_{\alpha r}}{L_s L_r - L_m^2} + \frac{2}{3} m i_f \tag{3.42}$$

$$i_{\beta s} = \frac{L_r \psi_{\beta s} - L_m \psi_{\beta r}}{L_s L_r - L_m^2} \tag{3.43}$$

$$i_{\alpha r} = \frac{L_s \psi_{\alpha r} - L_m \psi_{\alpha s}}{L_s L_r - L_m^2} \tag{3.44}$$

$$i_{\beta r} = \frac{L_s \psi_{\beta r} - L_m \psi_{\beta s}}{L_s L_r - L_m^2} \tag{3.45}$$

$$i_f = \frac{L_s i_{\alpha s} + L_m i_{\alpha r} - \frac{1}{m} \psi_{\alpha su}}{(L_s - L_m) + \frac{2}{3} m L_m} \tag{3.46}$$

The electromagnetic torque, $T_{em}$, in stationary $dq$ system under ITSC fault in the IM is given by the expression (Dongare *et al.*, 2020).

$$T_{em} = \frac{P}{2} L_m \left( \frac{3}{2} \left( i_{\beta s} i_{\alpha r} - i_{\alpha s} i_{\beta r} \right) - m i_f i_{\beta r} \right)$$ (3.47)

where $P$ numbers of poles

### 3.1.3 Mathematical modelling of ITSC fault in rotating DQ reference frame system

The transformation of the stationary DQ reference frame to the rotating DQ reference frame for any orthogonal system is generally given as:

$$\begin{bmatrix} v_d \\ v_q \end{bmatrix} = \begin{bmatrix} cos\theta & sin\theta \\ -sin\theta & cos\theta \end{bmatrix} \begin{bmatrix} v_\alpha \\ v_\beta \end{bmatrix}$$ (3.48)

where $v_d$ and $v_q$ are the two orthogonal $dq$ rotating direct- and quadrature-phase systems respectively, while $v_\alpha$ and $v_\beta$ are the corresponding $dq$ stationary system and $\theta$ is the angular displacement between the rotating and stationary phases.

Applying the rotating $dq$ reference frame transformation to equation (3.30) – (3.31) and equation (3.39) – (3.40), the voltage and flux linkages can be expressed as:

$$v_{dqs} = R_s i_{dqs} + \rho \psi_{dqs} \pm \omega \psi_{qds} - \frac{2}{3} m R_s i_f \begin{bmatrix} cos\theta \\ -sin\theta \end{bmatrix}$$ (3.49)

$$0 = R_r i_{dqr} + \rho \psi_{dqr} \pm (\omega - \omega_r) \psi_{qdr}$$ (3.50)

$$\psi_{dqs} = L_s i_{dqs} + L_m i_{dqr} - \frac{2}{3} m L_s i_f \begin{bmatrix} cos\theta \\ -sin\theta \end{bmatrix}$$ (3.51)

$$\psi_{dqr} = L_r i_{dqr} + L_m i_{dqs} - \frac{2}{3} m L_m i_f \begin{bmatrix} cos\theta \\ -sin\theta \end{bmatrix}$$ (3.52)

Where

$v_{dqs}$ is a matrix of direct- and quadrature-phase supplied voltage of the stator winding of the rotating $dq$ system.

$i_{dqs}$ and $i_{dqr}$ are the currents matrices of the stator and rotor windings in the rotating $dq$ system respectively.

$\psi_{dqs}$ and $\psi_{dqr}$ are the flux linkage matrices of the stator and rotor in the rotating $dq$ orthogonal system respectively.

Computing for the integral of the flux linkages, equations (3.49) – (3.52) becomes:

$$\psi_{ds} = \int (v_{ds} - R_s i_{ds} - \omega \psi_{qs} + \tfrac{2}{3} m R_s i_f \cos\theta) dt \qquad (3.53)$$

$$\psi_{qs} = \int (v_{qs} - R_s i_{qs} + \omega \psi_{ds} - \tfrac{2}{3} m R_s i_f \sin\theta) dt \qquad (3.54)$$

$$\psi_{dr} = \int (-(\omega - \omega_r)\psi_{qr} - R_r i_{dr}) dt \qquad (3.55)$$

$$\psi_{qr} = \int ((\omega - \omega_r)\psi_{dr} - R_r i_{qr}) dt \qquad (3.56)$$

$$\tfrac{1}{m}\psi_{\alpha su} = \int -R_s(i_{ds} - i_f)\cos\theta\, dt \qquad (3.57)$$

where $\psi_{ds}$ and $\psi_{qs}$, are respective direct- and quadrature-phase flux linkages in the stator windings of the rotating $dq$ system, $\psi_{dr}$ and $\psi_{qr}$ are respective direct- and quadrature-phase flux linkages in the rotor windings of the rotating $dq$ system. $i_{ds}, i_{qs}, i_{dr}$ and $i_{qr}$ are the direct-phase current in the stator winding, quadrature-phase current in the stator winding, direct-phase current in the rotor winding and quadrature-phase current in the rotor winding in the rotating $dq$ system respectively. And $\omega$ is the electromagnetic speed.

By solving for the currents in equations (3.49) – (3.50), the stator currents in rotating $dq$ become:

$$i_{ds} = \frac{L_r \psi_{ds} - L_m \psi_{dr}}{L_s L_r - L_m^2} + \tfrac{2}{3} m i_f \cos\theta \qquad (3.58)$$

$$i_{qs} = \frac{L_r \psi_{qs} - L_m \psi_{qr}}{L_s L_r - L_m^2} + \tfrac{2}{3} m i_f \sin\theta \qquad (3.59)$$

The rotor currents in stationary and rotating reference frames are the same for an ITSC fault on a stator winding of a squirrel cage IM.

The electromagnetic torque in this rotating $dq$ reference frame is given by:

$$T_{em} = \frac{P}{2} L_m \left( \frac{3}{2} (i_{qs} i_{dr} - i_{ds} i_{qr}) - m i_f (i_{qr} sin\theta - i_{dr} cos\theta) \right) \quad (3.60)$$

### 3.1.4 Mathematical equations of the speed

The rotor speed, $\omega_r$ of the IM is given by the relationship:

$$\omega_r = P \int \frac{T_{em} - T_L}{2J} dt \quad (3.61)$$

Where $T_L$ is the load torque in Nm, and J is the moment of inertia in kg.m$^2$

The angular displacement and electromagnetic speed are related as:

$$\theta = \int \omega dt \quad (3.62)$$

Where, $\omega = 2\pi f$, $f$ is the frequency of the power network.

The synchronous speed, $N_s$ is given as:

$$N_s = \frac{120f}{P} \quad (3.63)$$

### 3.2    Simulation and Extraction of Torque, Speed and Currents Datasets

The mathematical model of the three-phase IM, described by the equation of flux linkages, currents, voltages, speed and torque in section 3.1, was simulated on the MATLAB environment (precisely MATLAB version 9.6 R2019a) as shown in Figure 3.4.
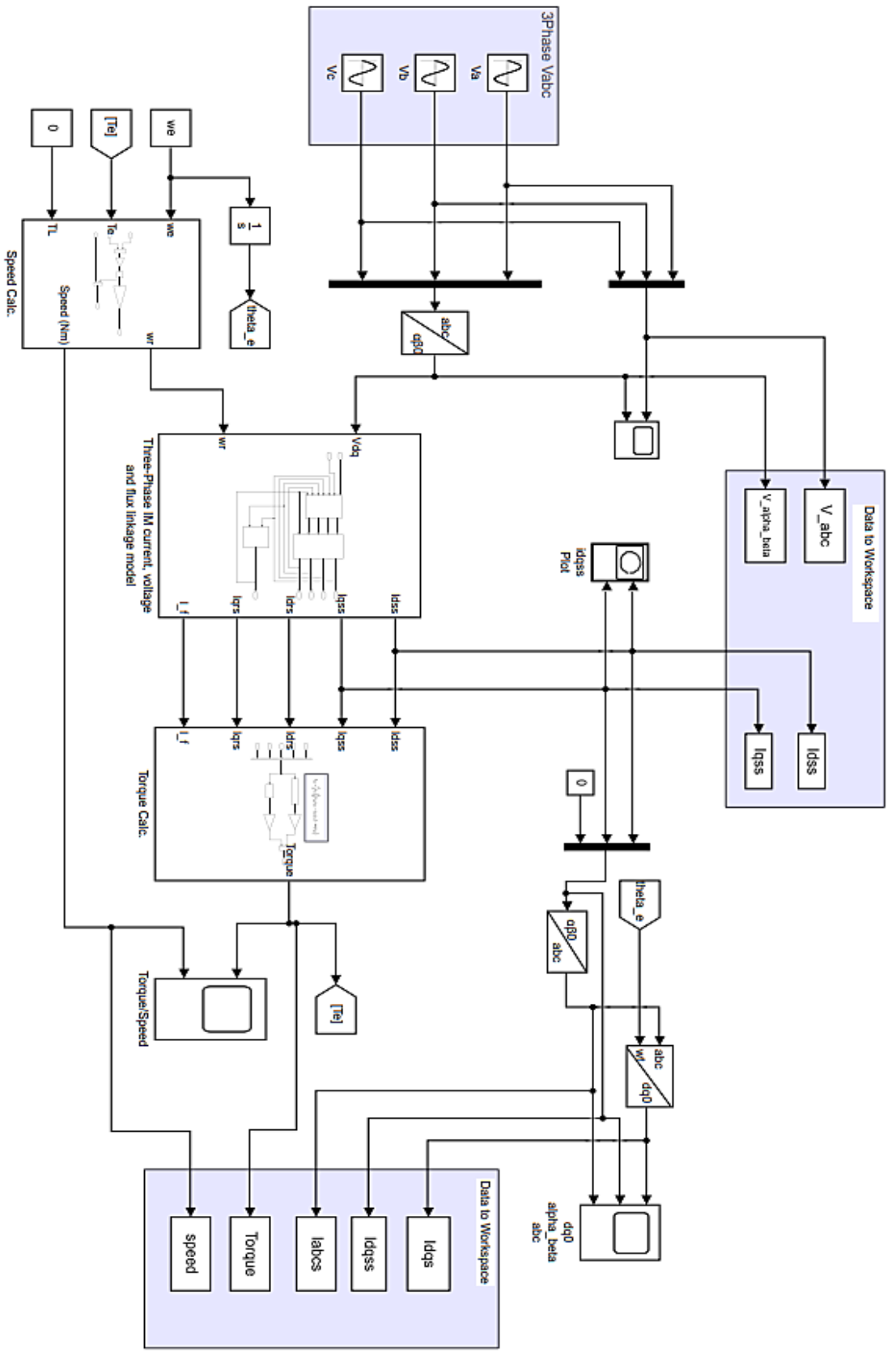
**Figure 3.4:** Simulation of IM in Simulink

For the proper simulation of the IM, the values of winding resistances, inductances (self and mutual), the moment of inertia, and numbers of poles, motor operating frequency and voltages have to be given. These values can be extracted experimentally by performing a short circuit test. However, for this research, these parameters were obtained from the research done by Arunachalam and Arumugam (2018). Table 3.1 presents the values of the three-phase squirrel cage IM used (Arunachalam and Arumugam, 2018).

**Table 3.1: Parameter of a three-phase squirrel cage IM**

| Machine Input Parameters | Values |
|---|---|
| Nominal Power, L-L Voltage, frequency | 4kW, 400V, 50Hz |
| Stator ($R_s$, $L_{ls}$) | 1.405$\Omega$, 0.005839H |
| Rotor ($R_r$, $L_{lr}$) | 1.395$\Omega$, 0.005839H |
| Mutual Inductance, $L_m$ | 0.1722H |
| Moment of Inertia, J and Poles, P | 0.089kg.m$^2$, 4 |

To illustrate the condition of ITSC faults of varying degrees, the value of the ratio of shortened turns to total turns, $m$, was arbitrarily varied from $0 - 10$ %. Under each variation of $m$, the datasets of torque, speed and Park vector currents components were obtained from the SIMULINK to the MATLAB workspace. These obtained data were further processed by programming to study and analyze the impact of ITSC faults on the torque, speed and Park current waveforms of the three-phase IM. The relevant MATLAB M-files are given in Appendices A, B, C and D.

## 3.3    Park Vector Plot (PVP) and Computation of PVM

In other to obtain the PVP without transient harmonics or interference, the datasets of the Park currents were processed using matrix slicing to obtain the steady-state currents such that:

$$i_{\alpha\beta s} = i_{dqs} = \begin{cases} 0, & t \leq t_t \\ i_{dqs}, & t > t_t \end{cases} \qquad (3.64)$$

where $t$, is the simulation time and $t_t$, transient time.

The PVM is the modulus of Park vector currents components in a complex plane.

Let the PVM be denoted as $I_M$, then in a $dq$ complex plane ($I_{ds} + jI_{qs}$), the modulus is given as:

$$I_M = \sqrt{I_{ds}^2 + I_{qs}^2} \qquad (3.65)$$

$$\delta = \tan^{-1}\left(\frac{i_{qs}}{i_{ds}}\right) \qquad (3.66)$$

Where $\delta$ is the angle of displacement of the PVM as it rotates in the complex plane.

The PVP on the XY plane is the plot of the stationary $i_{\alpha s}$ current versus the stationary $i_{\beta s}$ current or the plot of the PVM, $I_M$ and angular displacement, $\delta$ in a complex plane. To simplify this, the former was used. Under each variation of $m$, the $i_{\alpha s}$ were plotted against $i_{\beta s}$ to obtain the PVP. The distortions of the shapes of the PVP were observed to vary proportionately to the values of $m$. This visualized distortion was used to diagnose the presence of ITSC fault in the three-phase IM.

## 3.4 Computation of Fault Severity

A non-faulty IM operating in a steady state (after the transient noise has been removed) contains only DC components in the Park Vector reference transformation. However, under an ITSC fault, the introduction of a negative sequence into the IM as the result of the ITSC fault, causes it to have other AC signals along with the DC component. As reported by Cruz and Cardoso (2001), the AC signal varies with the degree of the fault.

Many computation techniques involving the measurement of the peak of the AC spectrum, the maximum and minimum PVM and the angle of the PVM have been used to estimate fault severity in an IM. However, the characteristic of an IM under ITSC fault has shown that the PVM differs along its elliptical locus making it difficult to use only the extreme values to accurately judge the severity of the abnormality in the IM.

In this research, to measure the severity of the ITSC fault in the IM, the variance, and standard deviation were used to measure the deviation, and dispersion of the PVM data on its elliptical loci, and Root Mean Square Error (RMSE) values were used to compare the correlation between faults PVM and the unfaulty PVM.

The variance, $I_{var}$ for an N number of $I_M$ is given as:

$$I_{var} = \frac{\sum_{i=1}^{N}(I_M - \overline{I_M})^2}{N-1} \tag{3.67}$$

Where, the mean PVM, $\overline{I_M}$ is given as:

$$\overline{I_M} = \frac{\sum_{i=1}^{N} I_M}{N} \tag{3.68}$$

The standard deviation, $I_{std}$ for the same N number of $I_M$ datasets is given as:

$$I_{std} = \sqrt{I_{var}} = \sqrt{\frac{\sum_{i=1}^{N}(I_M - \overline{I_M})^2}{N-1}} \tag{3.69}$$

The RMSE value denoted as $I_{RMSE}$ is given as:

$$I_{RMSE} = \sqrt{\frac{\sum_{i=1}^{N} |(\overline{I_{M m\neq 0}} - \overline{I_{M m=0}})|^2}{N}}$$

(3.70)

Where,

$\overline{I_{M m=0}}$ is the mean PVM when the IM is not faulty (that is, ITSC faults = 0%).

$\overline{I_{M m\neq 0}}$ is the mean PVM when the IM is faulty (ITSC faults $\neq$ 0%).

The flow chart diagram for the methodology is shown in Figure 3.5.
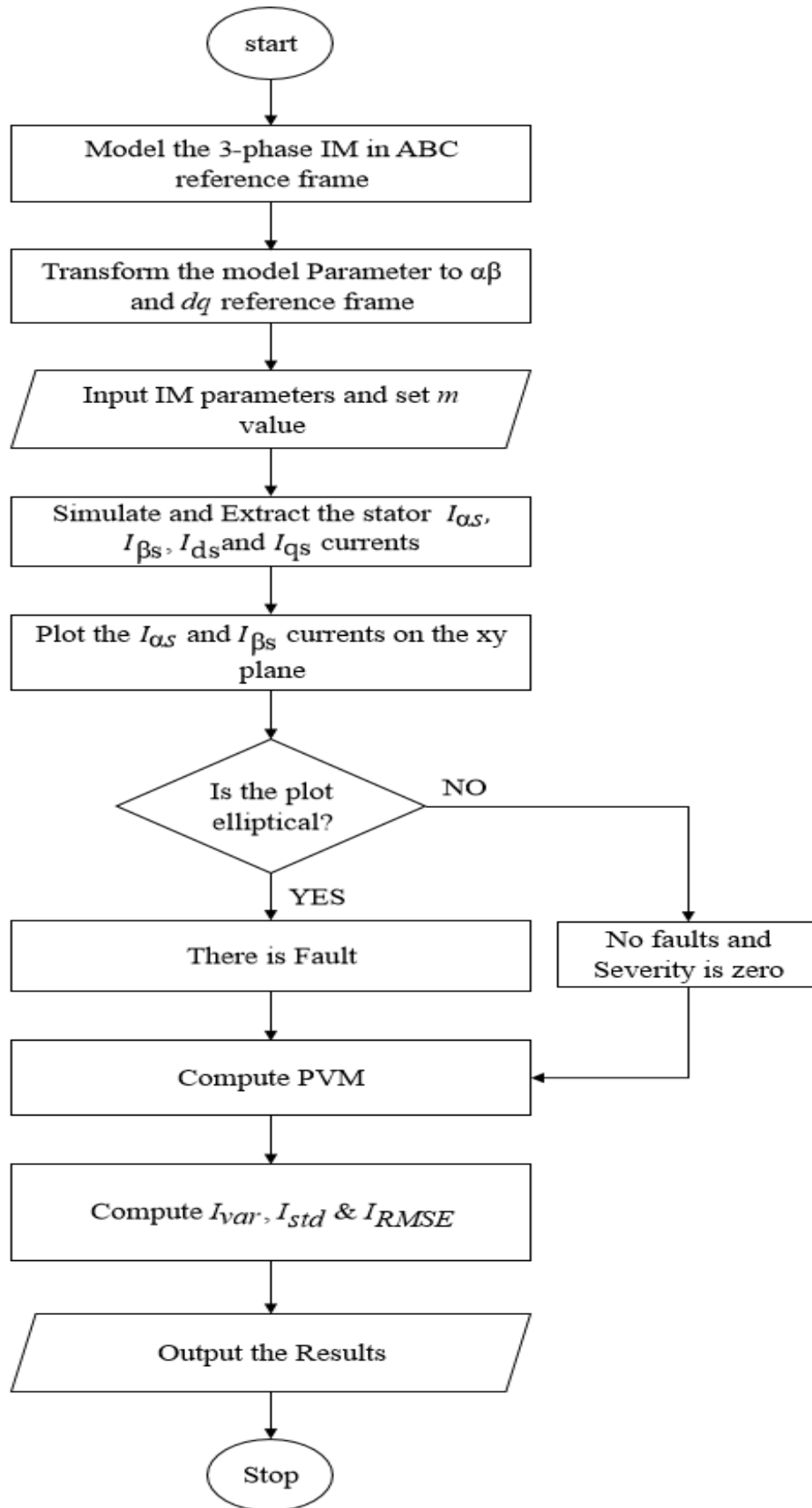
**Figure 3.5:** Flowchart for the research methodology

49

**CHAPTER FOUR**

**4.0**                      **RESULTS AND DISCUSSION**

This chapter presents the research results based on the simulation of the mathematical model of the three-phase squirrel cage IM described in chapter three. The simulation was done using MATLAB codes and SIMULINK blocks. The chapter concluded by presenting the safe allowable fault zone that the machine is allowed to operate beyond which, a total machine failure is imminent.

**4.1**     **Results**

As presented in section 3.2, the SIMULINK model of the IM was simulated with a varying winding parameter, *m* over a simulation time of 3 seconds. The results obtained are presented as follows.

**4.1.1**    **Supply voltage in ABC and stationary Park vector**
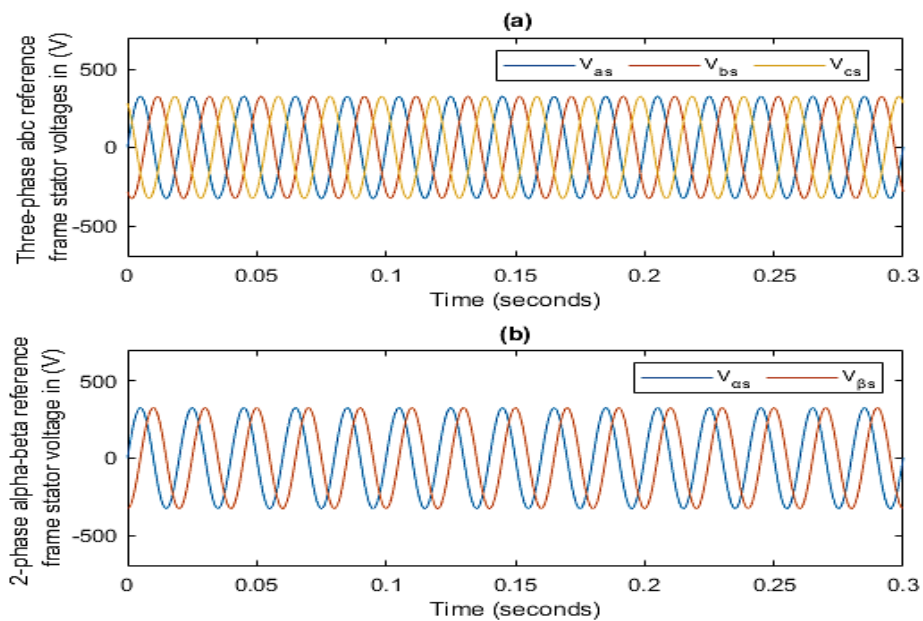


**Figure 4.1:** IM source voltages in (a) three-phase *abc* reference frame and (b) two-phase alpha-beta reference frame

The three-phase IM was supplied with an ideal three-phase alternating voltage source with the waveform as shown in Figure 4.1a. Figure 4.1b shows the transformation of the ABC reference source voltage to the stationary Park reference frame, which is the applied voltage to the transformation equations of flux linkages, currents, speed and torque.

### 4.1.2   Electromagnetic torque and speed

A state of no ITSC fault was simulated in the three-phase IM by setting the ratio of faulty turns to total turn, $m$ equals 0, under no load condition (that is, $T_L = 0$). The electromagnetic torque under this condition is shown in Figure 4.2a.
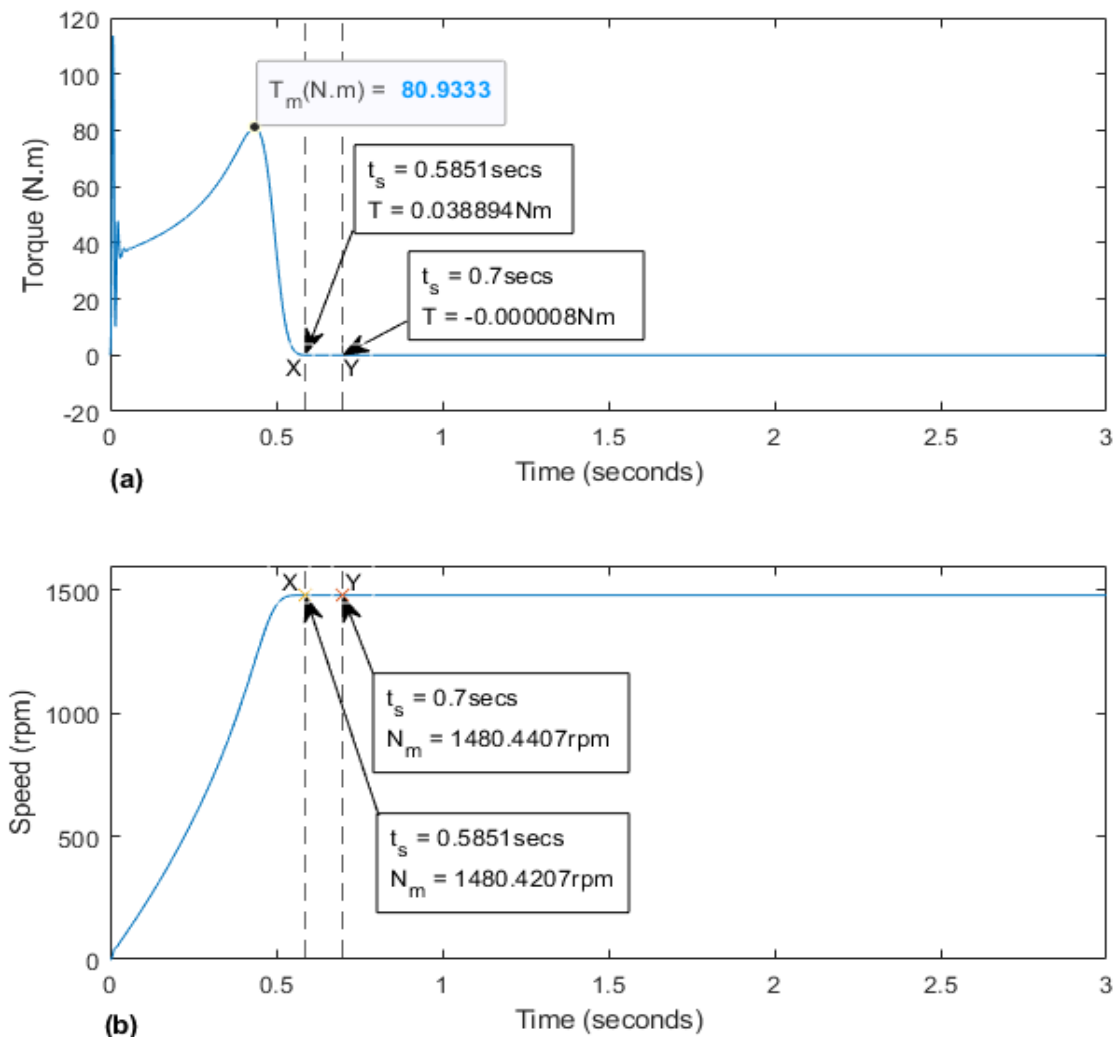


**Figure 4.2:** Graph of (a) electromagnetic torque and (b) rotor speed of the IM under healthy condition at no load.

51

Similarly, under no load condition and no ITSC fault, the rotor speed of the IM is as shown in Figure 4.2b.

The plot of the electromagnetic torque-speed characteristic under no-fault conditions is presented in Figure 4.3.
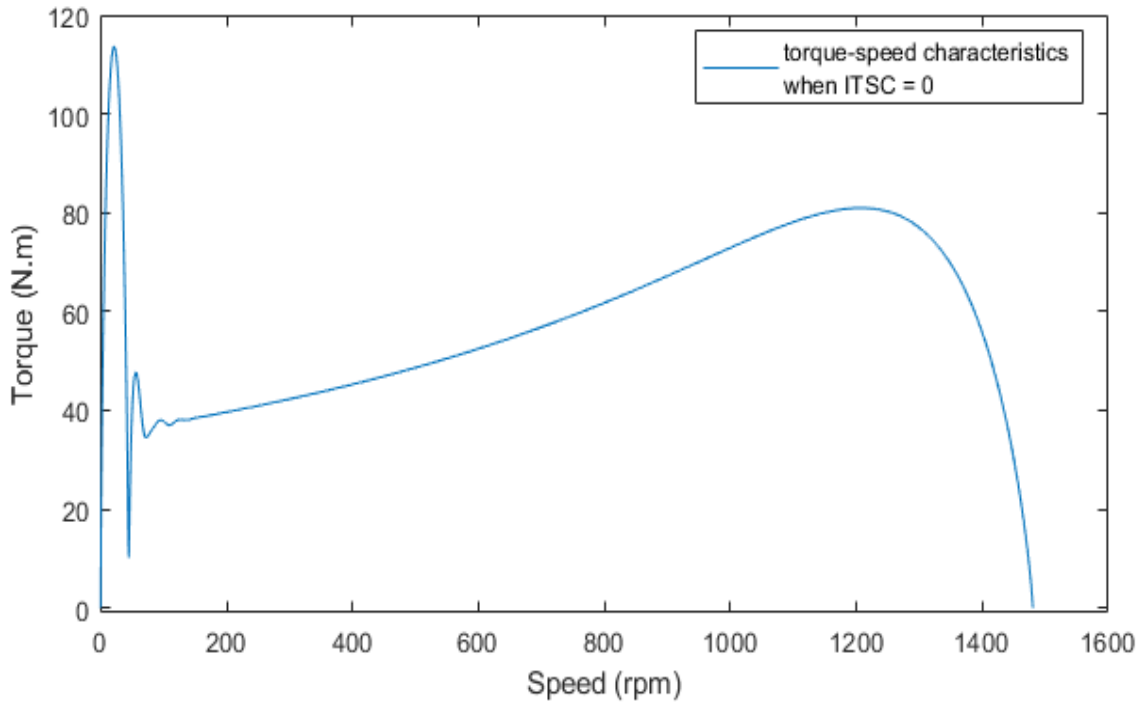


**Figure 4.3:** Torque-speed characteristic under no ITSC fault (m = 0%)

Simulating the IM SIMULINK model for a no-load condition and at 1% ITSC fault (that is, m = 1%), the plot of the torque and speed parameters obtained are shown in Figure 4.4. Similarly, the torque-speed characteristics of the IM under 1% ITSC fault is presented in Figure 4.5.
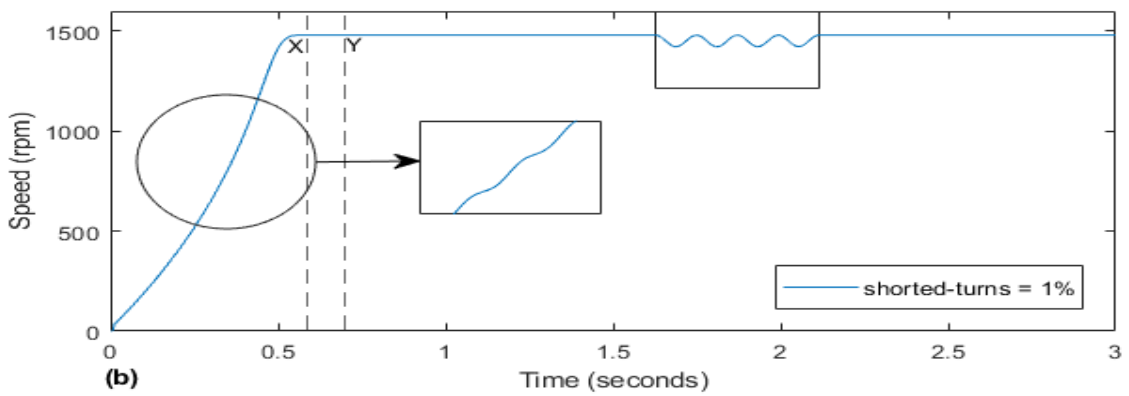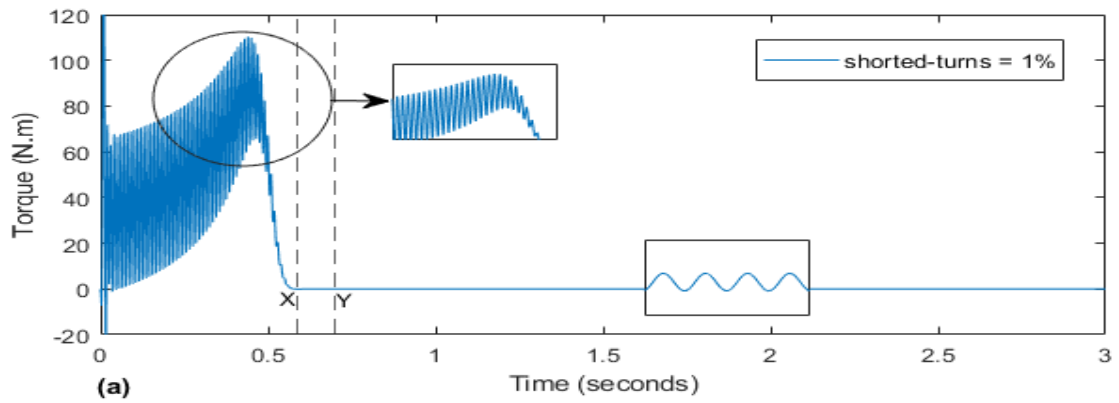
**Figure 4.4:** Graph of (a) electromagnetic torque and (b) rotor speed of the IM under 1%

ITSC fault at no load
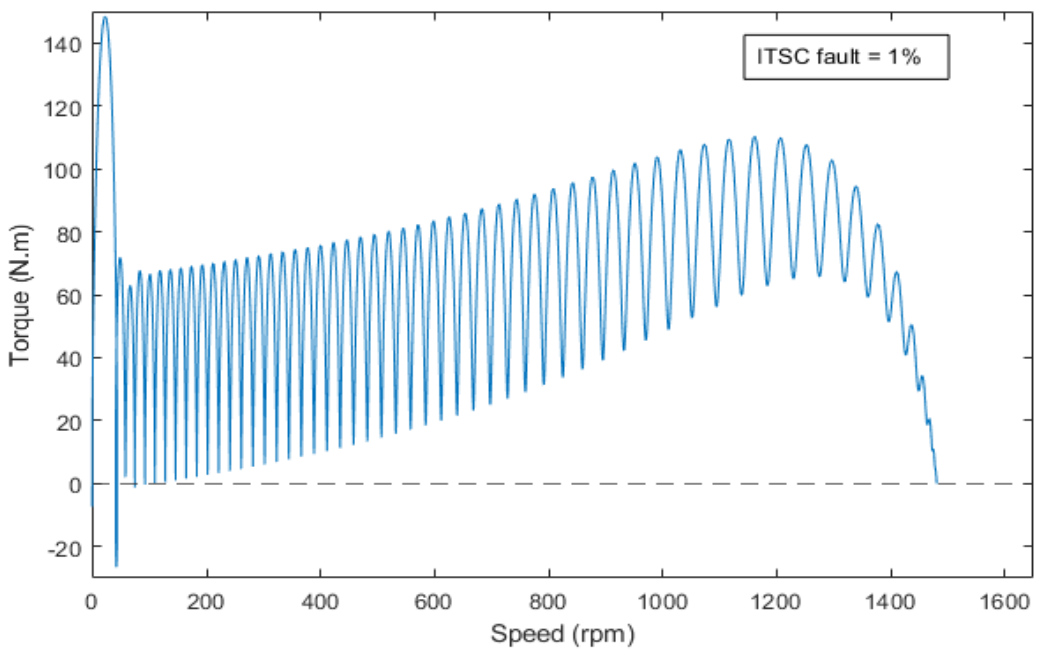


**Figure 4.5:** Torque-speed characteristic under 1% ITSC faults

Varying the value of *m* to 2%, 3%, 4%, 5%, 6%, and 7% to demonstrate the occurrence

of higher ITSC faults, the electromagnetic torque and speed plots are presented in Figure

4.6 and Figure 4.7 respectively.
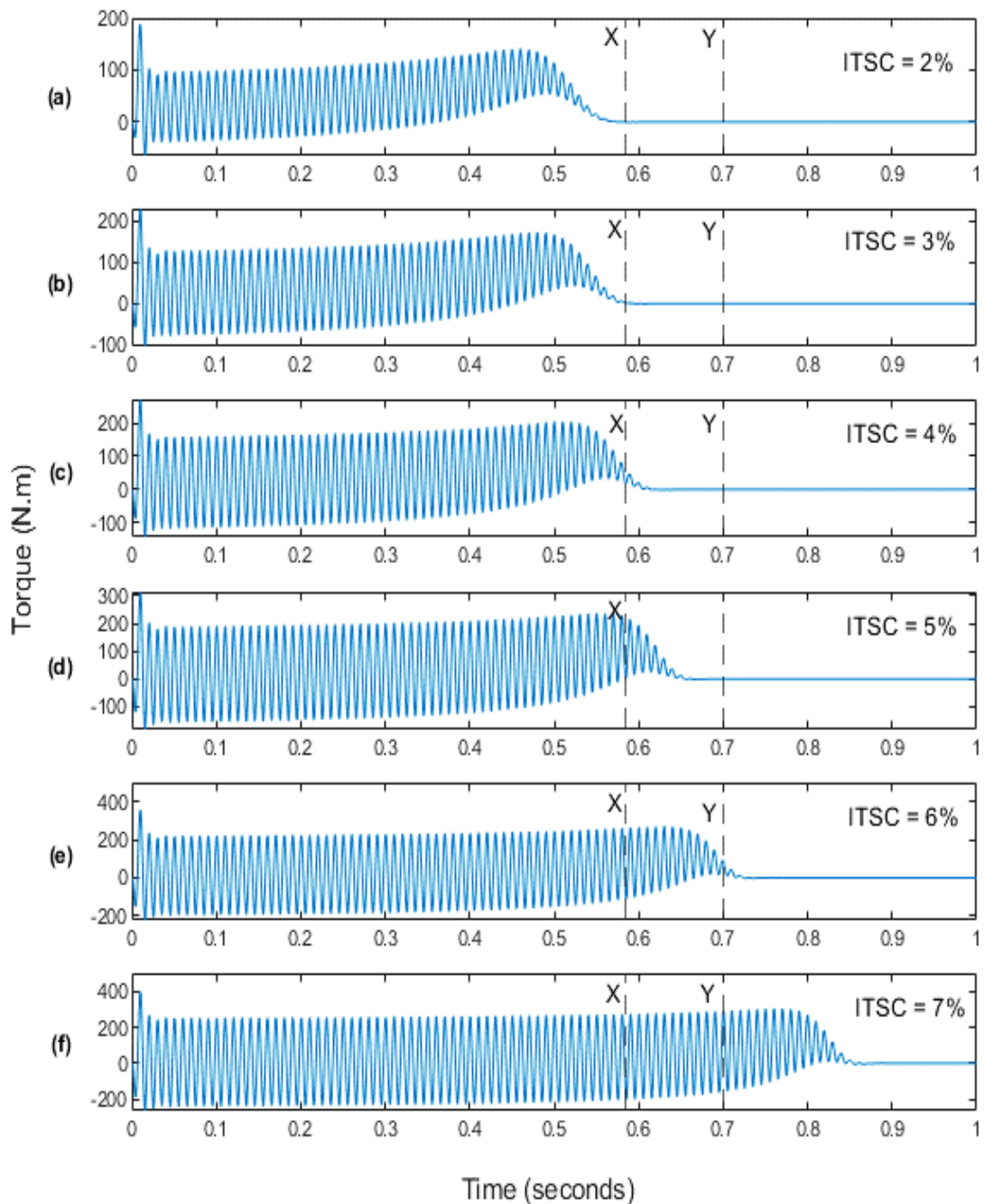


**Figure 4.6:** Torque for 2%, 3%, 4%, 5%, 6% and 7% ITSC fault respectively
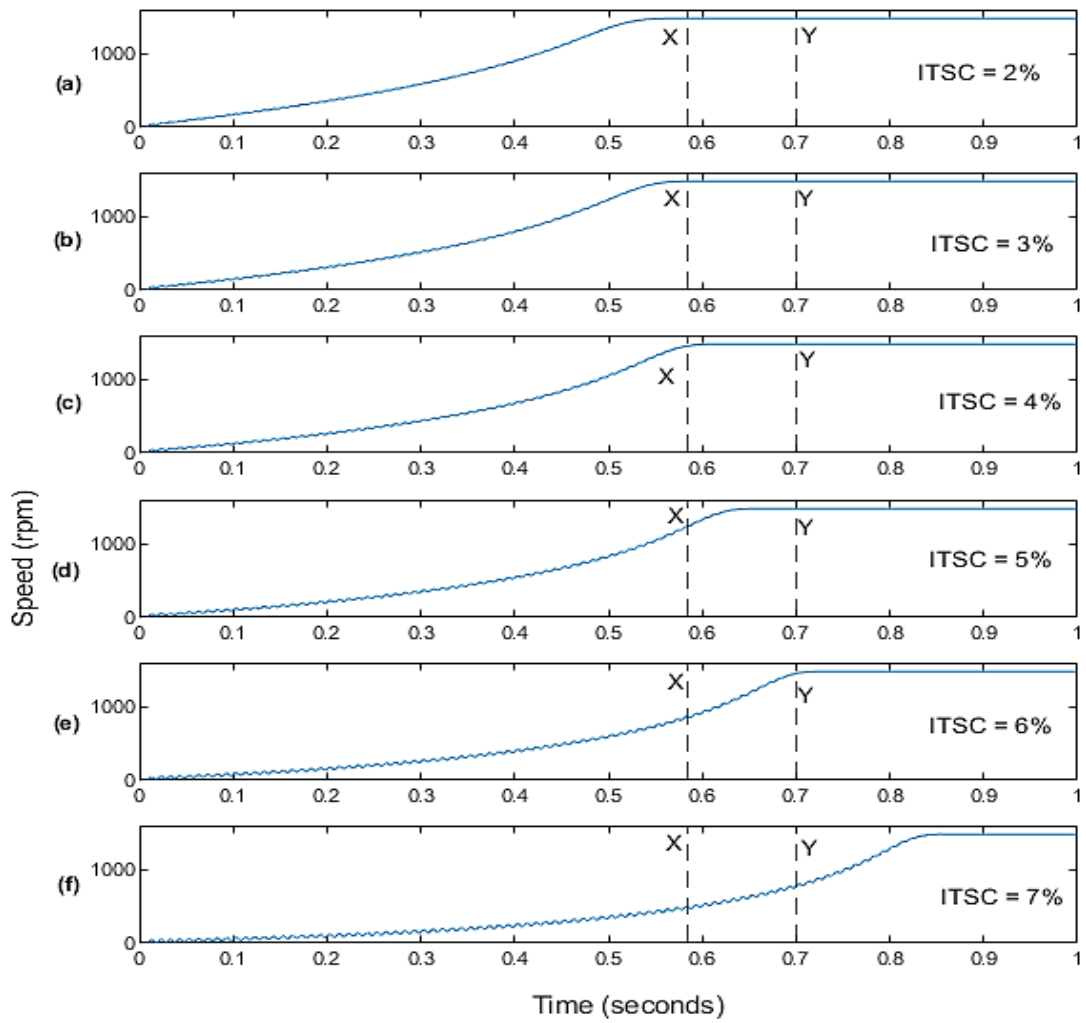
**Figure 4.7:** Rotor speed for 2%, 3%, 4%, 5%, 6% and 7% ITSC faults respectively
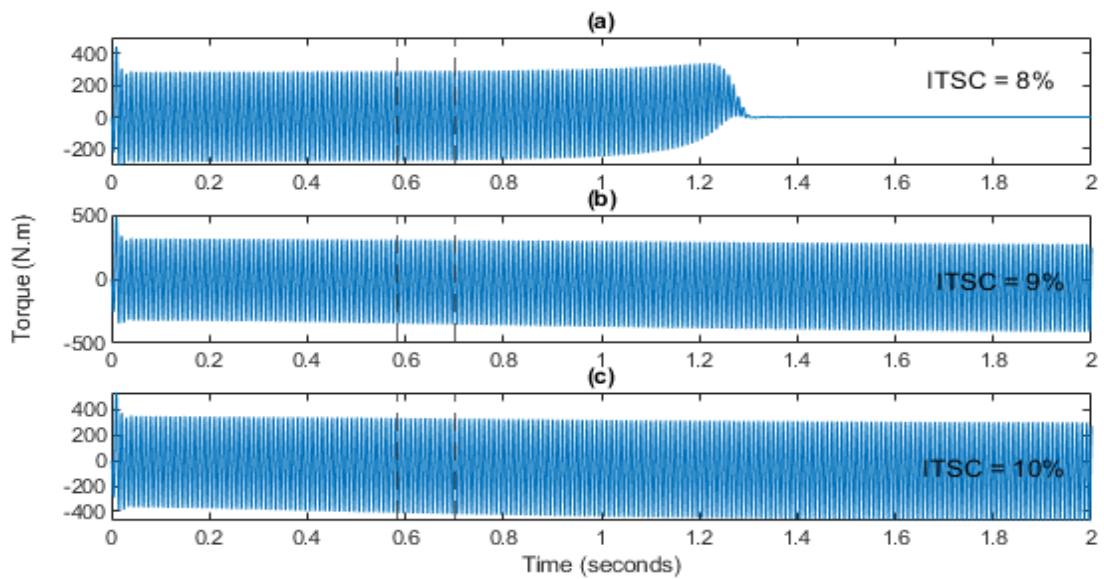


**Figure 4.8:** Torque for 8%, 9% and 10% ITSC faults respectively

The electromagnetic torque and speed waveforms under 8%, 9% and 10% ITSC faults are also presented in Figure 4.8 and Figure 4.9 respectively.
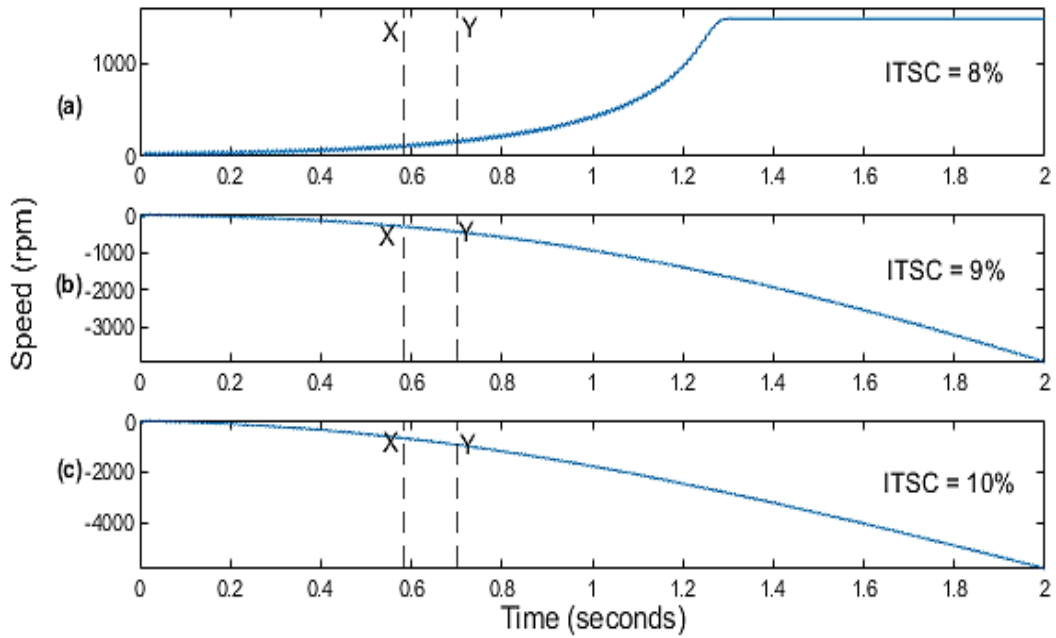


**Figure 4.9:** Rotor speed for 8%, 9% and 10% ITSC faults respectively

A special scenario was observed for ITSC fault level equals to 9% and 10%. To better understand the behaviour of the IM under these higher percentage of fault, the torque-speed characteristics of the IM at 9% ITSC fault was plotted as shown in Figure 4.10.
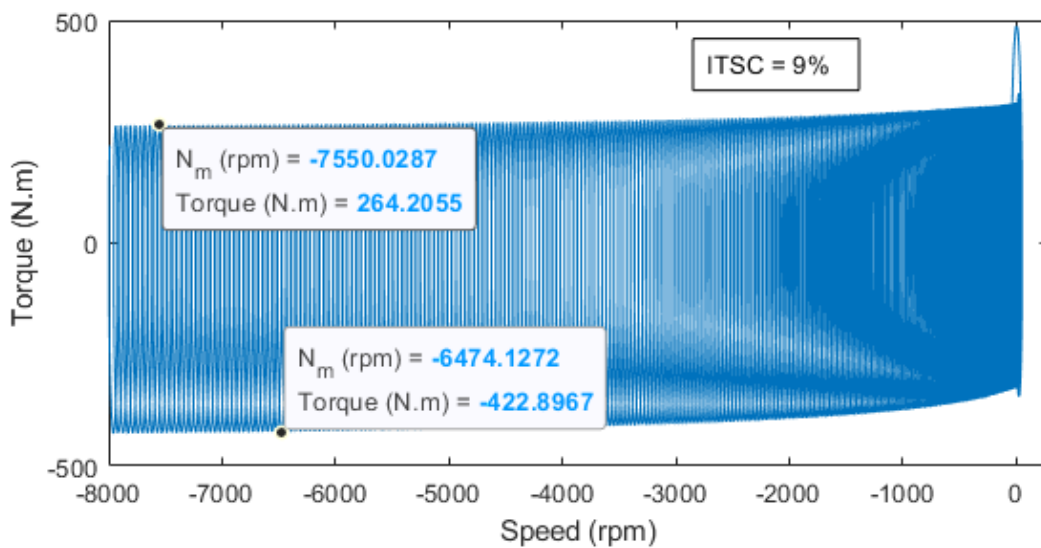


**Figure 4.10:** Torque-speed characteristics of IM for 9% ITSC Fault

56

### 4.1.3 Waveform of Park current components

Simulating $m = 0\%$ in the SIMULINK model of Figure 3.5, and extracting the waveform of the stationary and rotating Park currents components using M-files given in Appendix B, the results are presented in Figure 4.11a and 4.11b respectively.
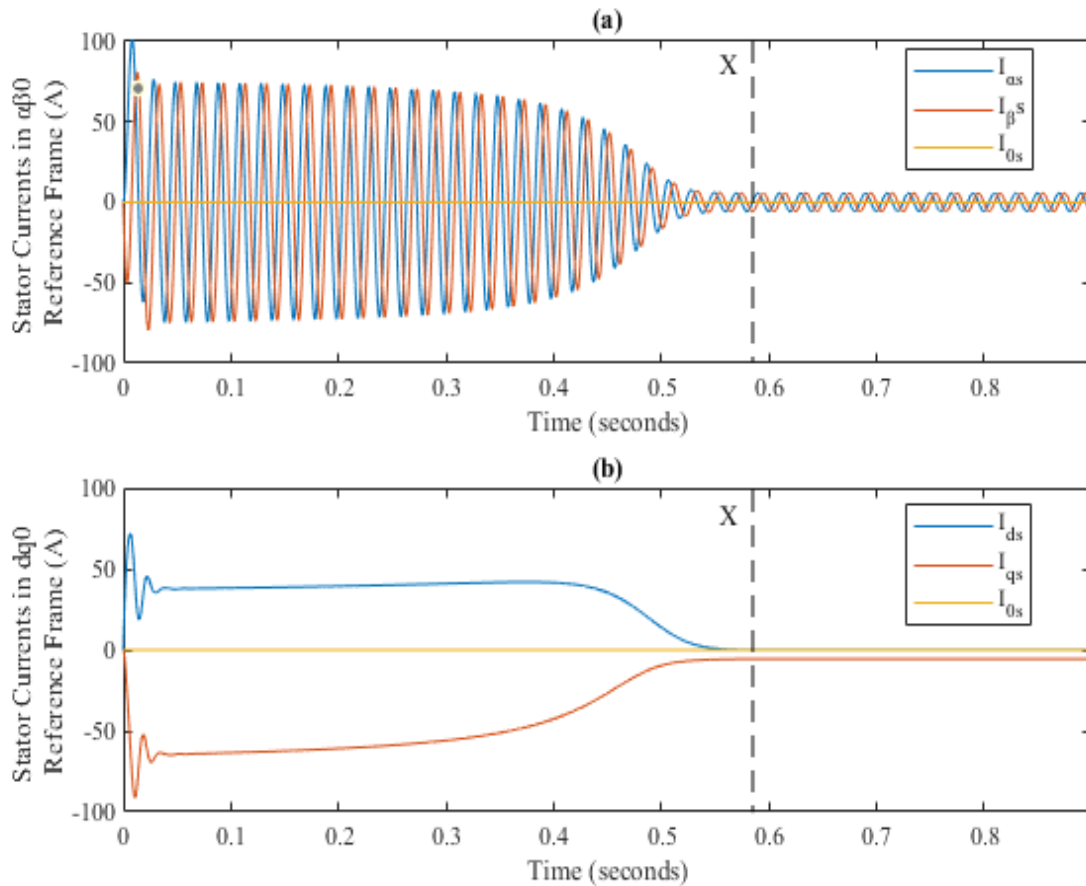


**Figure 4.11:** Stator currents for ITSC = 0% in (a) Park stationary plane and (b) Park rotating plane

The "X" dotted marked position is the same position marked on the torque and speed plot to indicate the end of the transient state in the IM.

By simulating the model for an ITSC fault of 1%, the Park currents waveform in the stationary and rotating reference frame is shown in Figure 4.12a and Figure 4.12b respectively.
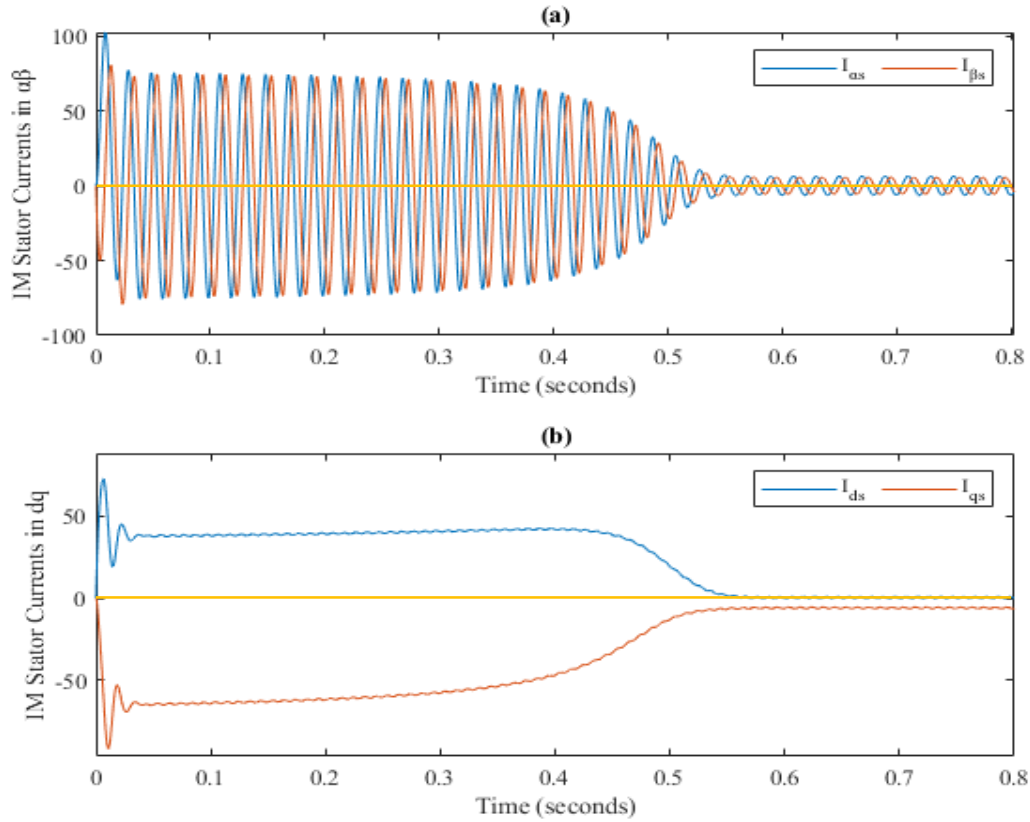
**Figure 4.12:** Stator currents for ITSC = 1% in (a) Park stationary plane and (b) Park

rotating plane

The wave patterns of the stationary and rotating Park currents for higher fault levels (2%

- 7%) are presented in Figure 4.13 and Figure 4.14 respectively. Using the M-files in

Appendix C, only the steady-state currents data were considered to better understand the

impact of higher ITSC fault on the Park current waveform.
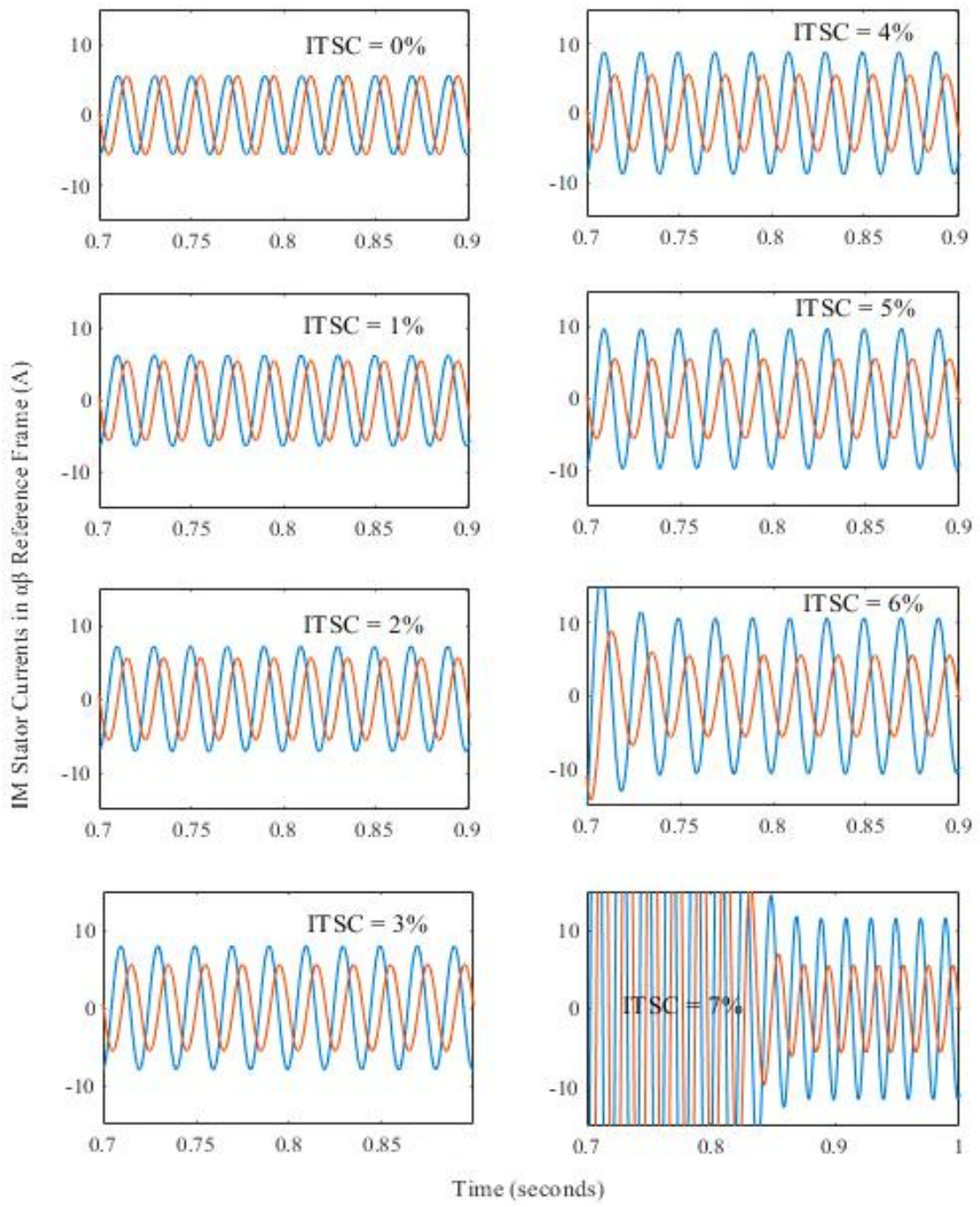
**Figure 4.13:** Steady – state stationary Park currents for 0%, 1%, 2%, 3%, 4%, 5%, 6%
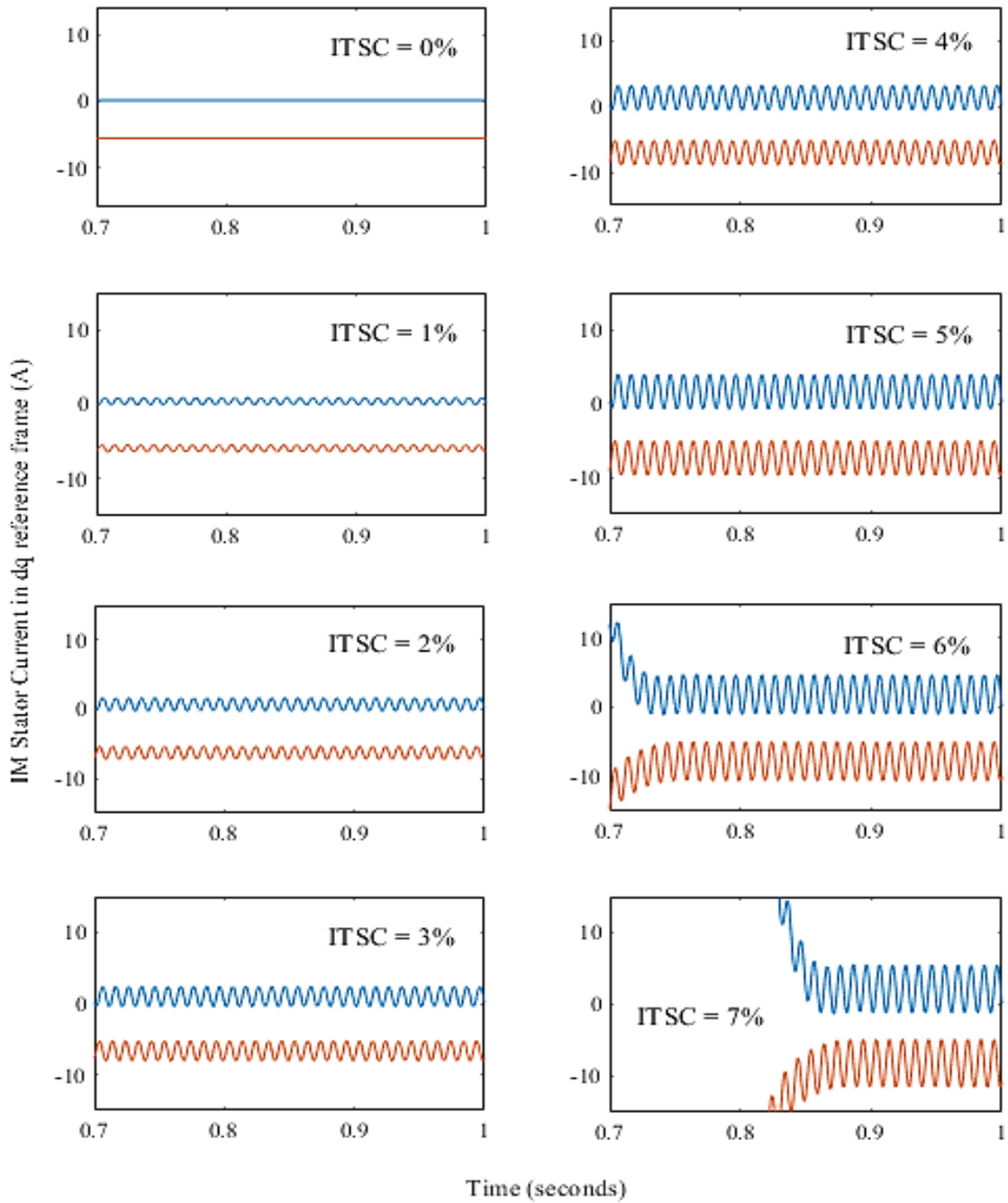
and 7% ITSC faults

**Figure 4.14:** Steady – state rotating Park currents for 0%, 1%, 2%, 3%, 4%, 5%,

6%, and 7% ITSC faults

### 4.1.4   Park vector plots

From the datasets of stationary and rotating Park currents components extracted, the PVPs

were obtained. The PVP is based only on the steady-state currents of the Park currents

component in other to remove the transient harmonics. Maintaining the same simulation time of 3 seconds and transient time of 0.7 seconds, the steady Park currents data were obtained using the M-file in Appendix C. The M-file in Appendix D was used to generate the PVP for each variation of *m* values.

To demonstrate the effect of transient state data on the visualized PVP, the plot of *m* = 0% (no fault in the IM) and m = 1% (that is, 1% ITSC fault) were compared as shown in Figure 4.15.
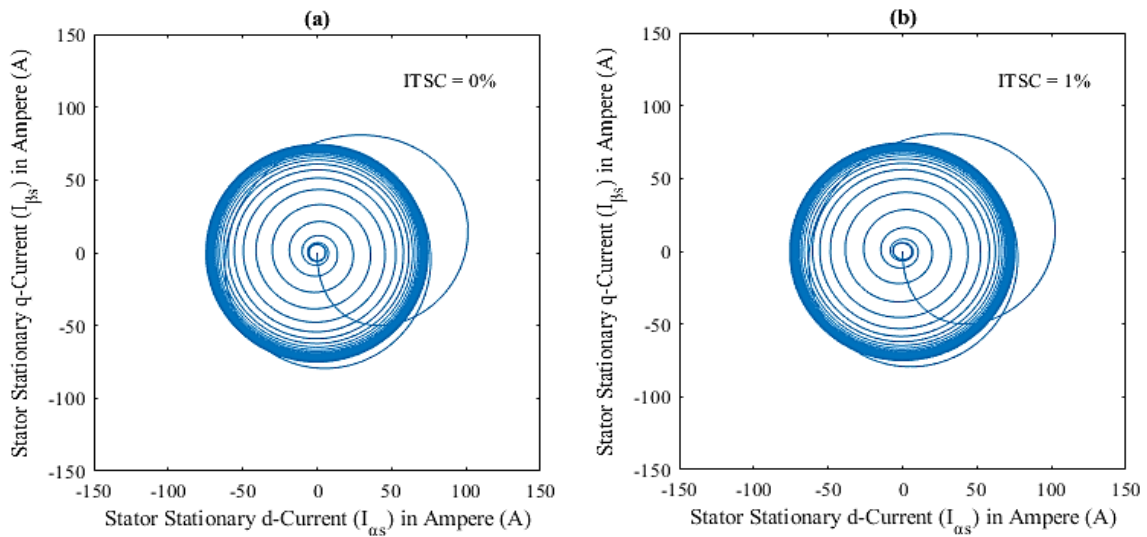


**Figure 4.15:** PVP for ITSC faults of (a) 0% and (b) 1% with transient harmonics

The transient data were removed to obtain only the steady-state currents, and the PVPs at 0% and 1%, in this case, were also presented as shown in Figure 4.16.

The shortened-turn ratio, *m*, was increased to indicate higher percentages of ITSC fault in the IM. The transient time of 0.7s was maintained in removing transient state harmonics. The visualized PVP for each variation are shown in Figure 4.17, Figure 4.18 and Figure 4.19.
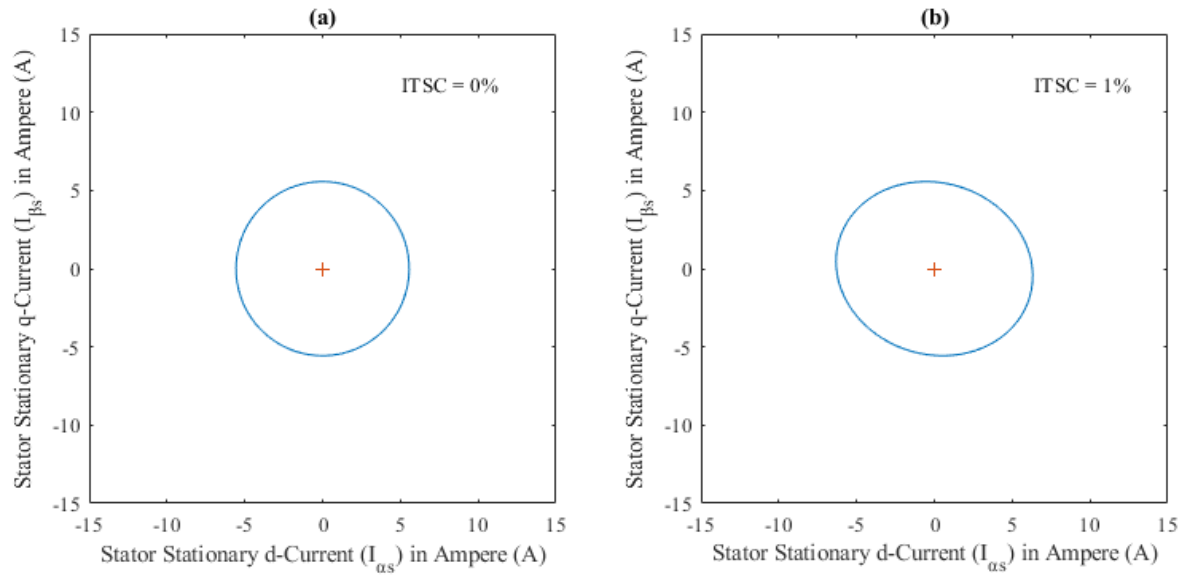
**Figure 4.16:** PVP for ITSC faults of (a) 0% and (b) 1% without transient harmonics
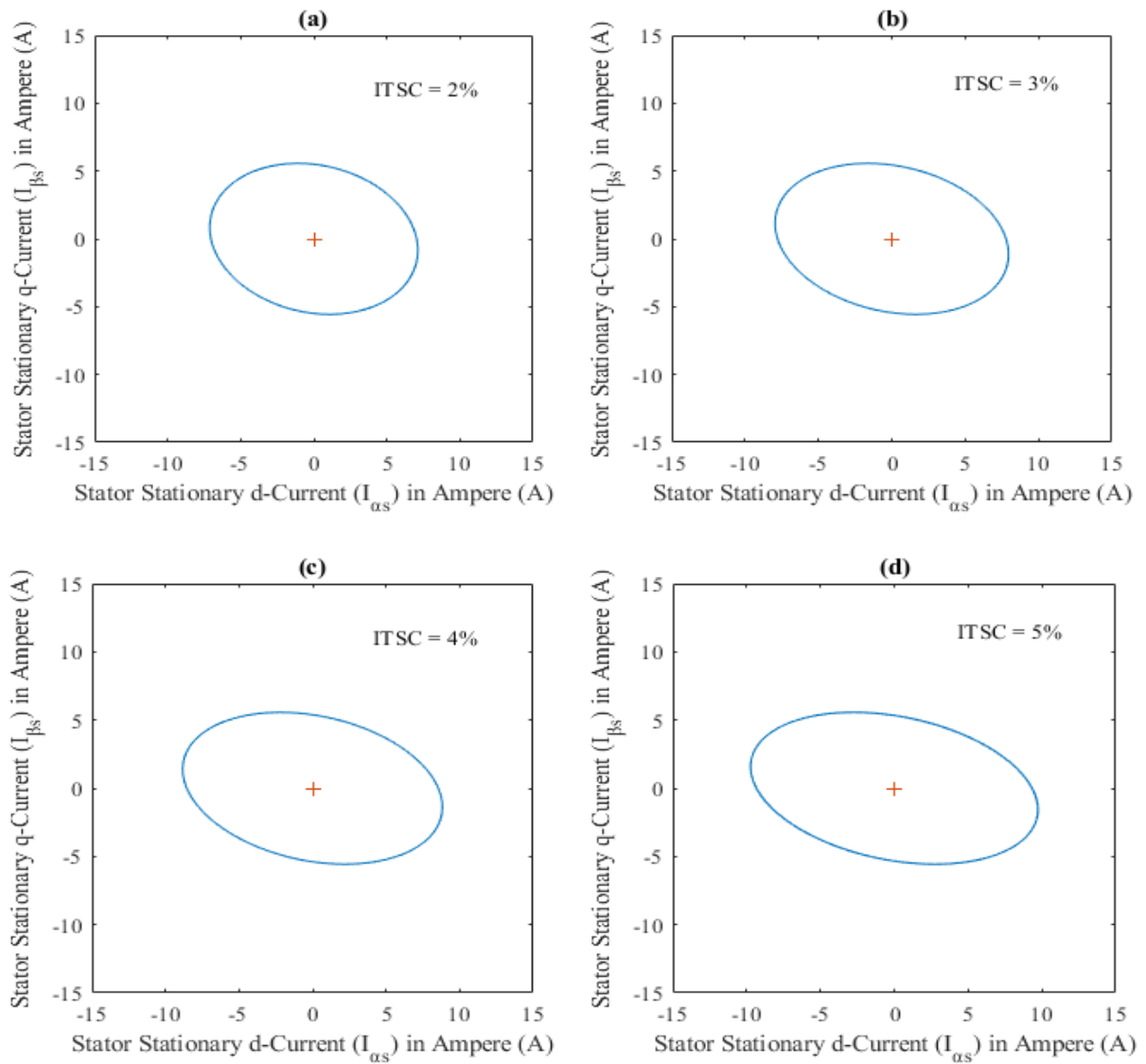


**Figure 4.17:** PVP for 2%, 3%, 4% and 5% ITSC faults
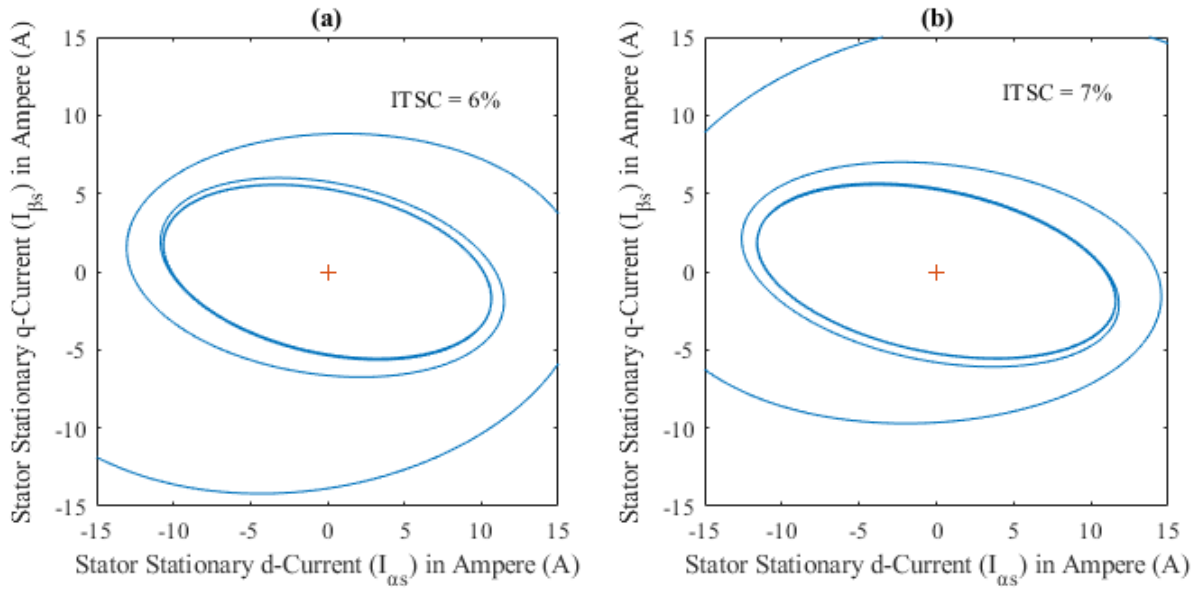
**Figure 4.18:** PVP for 6% and 7% ITSC faults
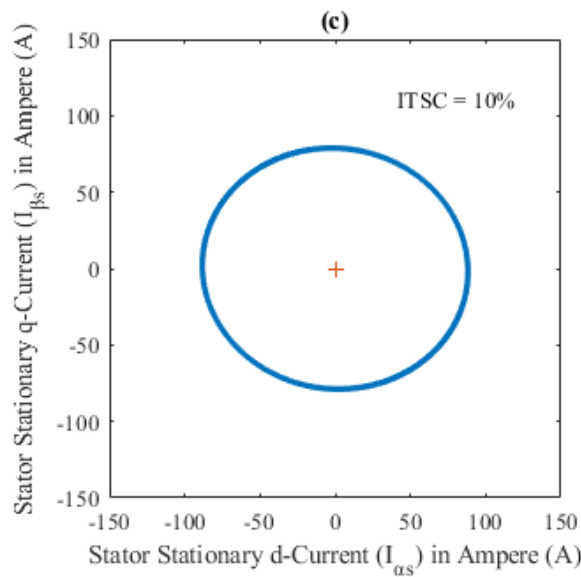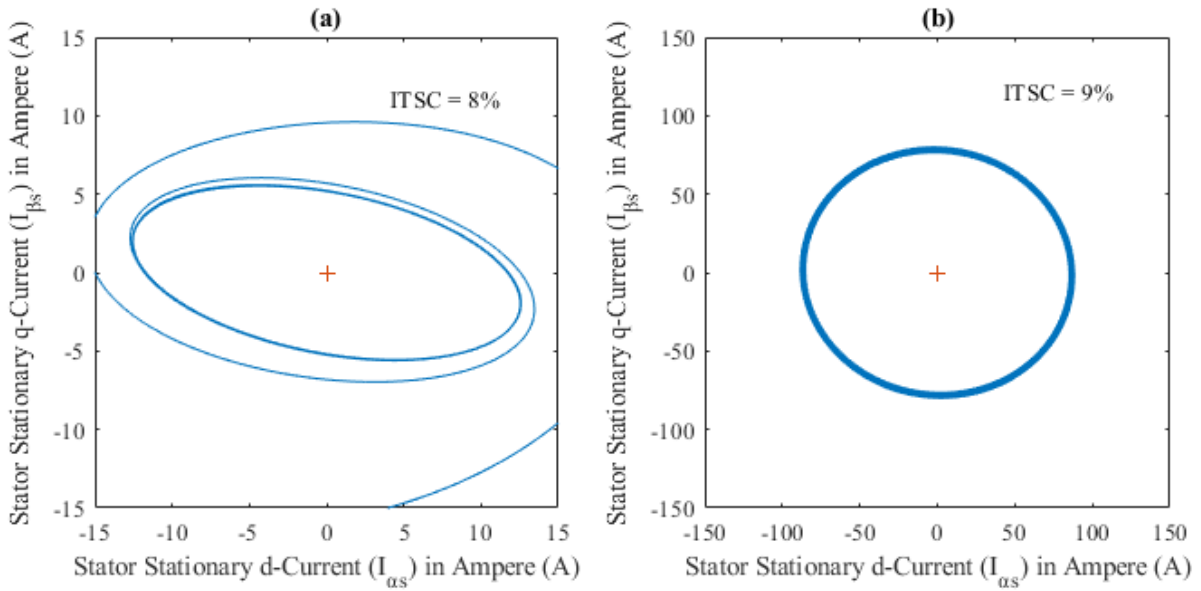


**Figure 4.19:** PVP for 8%, 9% and 10% ITSC faults

### 4.1.5   Computation of PVM

Using the M-file in Appendix D, the PVM, which is the radius of the PVP along its circular or elliptical locus was computed and used to compute the mean, variance, standard deviation and RMSE as described by equation $3.67 - 3.70$. Table 4.1 presents the results obtained.

**Table 4.1: Computation of mean, variance, standard deviation and RMSE values under no-load condition**

| % of ITSC Fault | Mean, $\overline{I_M}$ (A) | Variance, $I_{var}$ (A) | Standard Deviation, $I_{std}$ (A) | RMSE, $I_{RMSE}$ (A) |
|---|---|---|---|---|
| 0 | 5.5620 | 0 | 0 | 0 |
| 1 | 5.9430 | 0.1028 | 0.3207 | 0.4980 |
| 2 | 6.3556 | 0.4158 | 0.6448 | 1.0225 |
| 3 | 6.7963 | 0.9444 | 0.9718 | 1.5709 |
| 4 | 7.2621 | 1.6938 | 1.3014 | 2.1410 |
| 5 | 7.7508 | 2.6686 | 1.6336 | 2.7312 |
| 6 | 8.3141 | 4.1513 | 2.0375 | 3.4242 |
| 7 | 11.5942 | 141.7204 | 11.9046 | 13.3455 |
| 8 | 25.3598 | 786.9049 | 28.0518 | 34.3340 |
| 9 | 83.1437 | 10.2628 | 3.2036 | 77.6478 |
| 10 | 84.1568 | 12.1560 | 3.4866 | 78.6721 |

From Table 4.1 obtained above, by plotting the percentage (%) of ITSC faults versus the

Mean PVM, $\overline{I_M}$, and RMSE, $I_{RMSE}$ values, a graph as shown in Figure 4.20 was obtained.
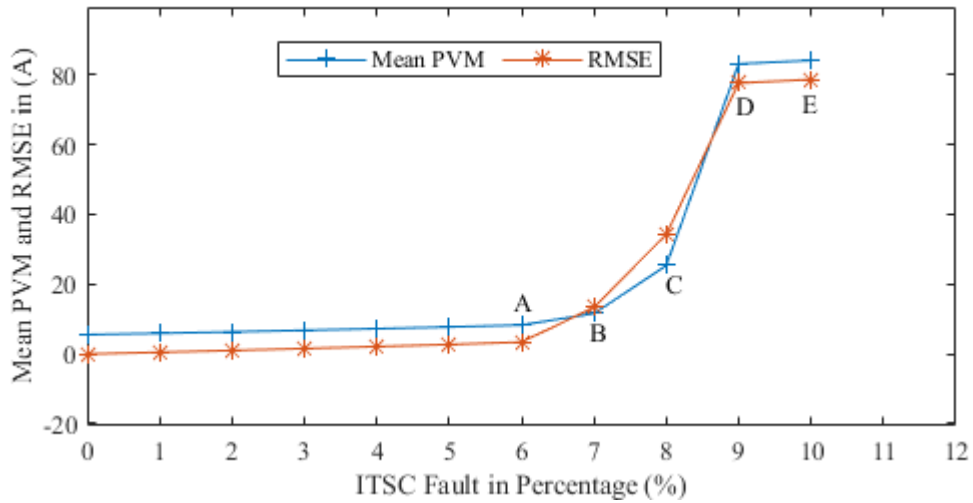


**Figure 4.20:** No-load ITSC fault versus mean PVM and RMSE

Similarly, the percentage of ITSC faults plotted against the variance, $I_{var}$, and standard

deviation, $I_{std}$, presented a graph as shown in Figure 4.21.
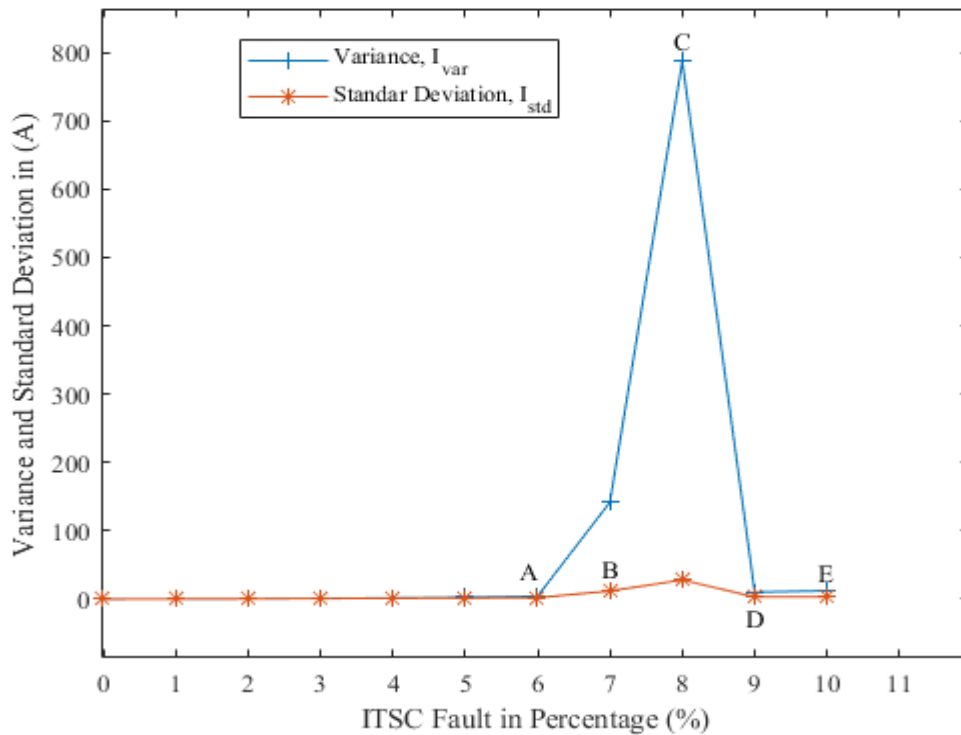


**Figure 4.21:** No-load ITSC faults versus variance and standard deviation

To further study how the severity of faults behaves under load conditions, a rated load with a torque of 5N.m (that is, $T_L = 5N.m$) was simulated with varying $m$ values (that is, $0 - 10\%$ ITSC faults) and the results of mean PVM, variance, standard deviation and RMSE are tabulated in Table 4.2.

**Table 4.2: Computation of mean, variance, standard deviation and RMSE values with rated load torque**

| % of ITSC Fault | Mean, $\overline{I_M}$ (A) | Variance, $I_{var}$ (A) | Standard Deviation, $I_{std}$ (A) | RMSE, $I_{RMSE}$ (A) |
|---|---|---|---|---|
| 0 | 6.0275 | 0 | 0 | 0 |
| 1 | 6.4276 | 0.1130 | 0.3361 | 0.5225 |
| 2 | 6.8462 | 0.4940 | 0.7028 | 1.0790 |
| 3 | 7.3216 | 1.0370 | 1.0183 | 1.6467 |
| 4 | 7.8076 | 1.8597 | 1.3637 | 2.2424 |
| 5 | 8.3266 | 2.9404 | 1.7148 | 2.8681 |
| 6 | 11.2075 | 118.9644 | 10.9071 | 12.0744 |
| 7 | 25.3711 | 825.4171 | 28.7301 | 34.6346 |
| 8 | 86.4447 | 8.9322 | 2.9887 | 80.4727 |
| 9 | 87.4943 | 10.6923 | 3.2699 | 81.5324 |
| 10 | 88.2946 | 13.0661 | 3.6147 | 82.3464 |

Under this load condition, a plot of ITSC faults versus the Mean PVM and the RMSE was obtained as shown in Figure 4.22.
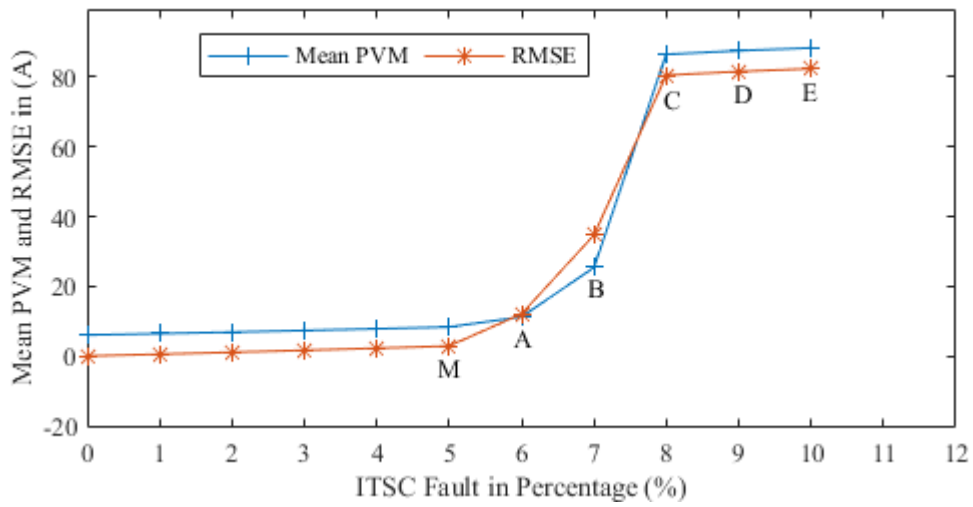


**Figure 4.22:** ITSC faults versus mean PVM and RMSE under a rated load torque

Similarly, a plot of ITSC faults versus variance and standard deviation under the load condition is shown in Figure 4.23.
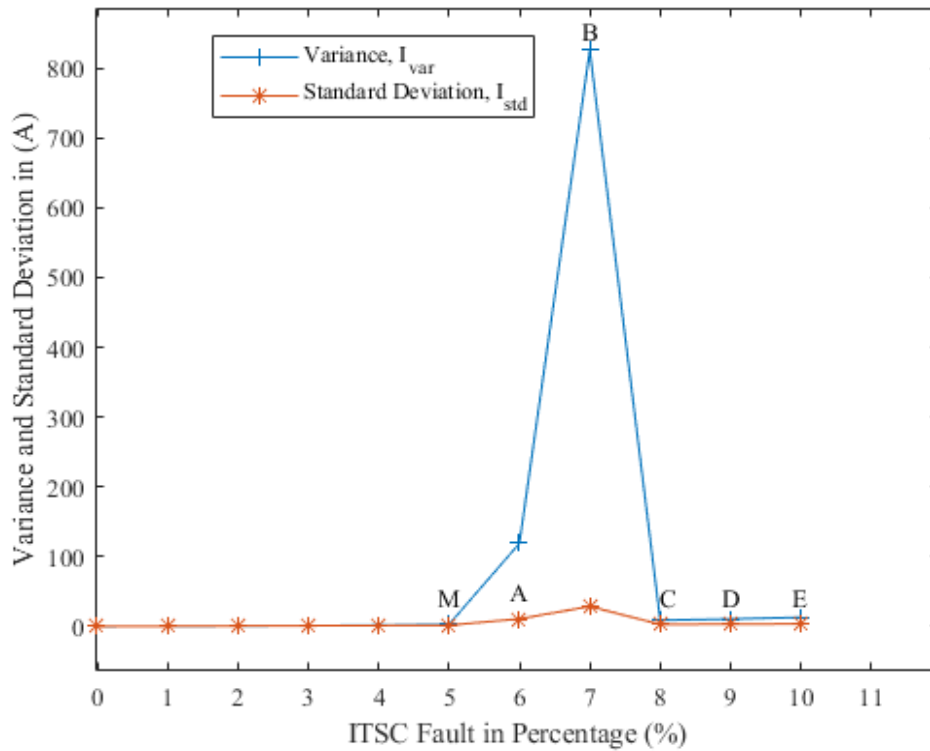


**Figure 4.23:** ITSC faults versus variance and standard deviation under a rated load condition

The Mean PVM and RMSE under the no-load and the rated load conditions were combined in a single plot to observe the difference as shown in Figure 4.24a and Figure 4.24b respectively.
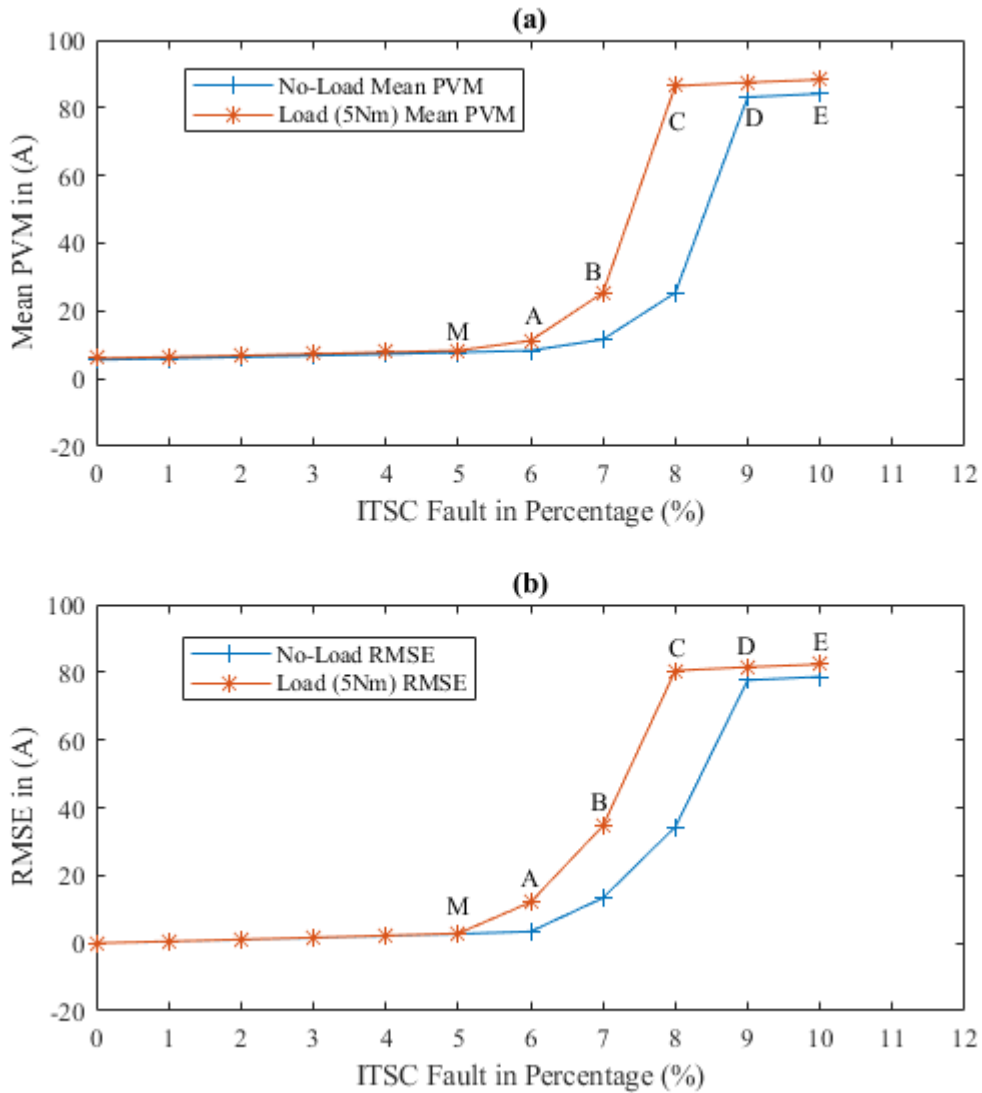


**Figure 4.24:** ITSC faults versus no-load and rated load (a) mean PVMs and (b) RMSEs

## 4.2 Discussion of Results

To understand the behaviour of the IM under varying faults conditions, the elaborate discussion of the results presented in section 4.1 are given as follows:

### 4.2.1 Voltage transformation

As shown in Figure 4.1, the input source voltage to the IM is an ideal three-phase sinusoidal alternating voltage which is the ideal voltage source found in most power systems.

Using the line-to-line voltage rating of the IM given in section 3.2, the SIMULINK model was fed with 230V line-to-neutral equivalent at 50 Hz. The voltage source waveform in the normal ABC reference frame system is given in Figure 4.1a. As stated earlier in section 3.1, EPVA uses Park current components, therefore, the need to transform the voltage source from the ABC reference frame to the Park reference frame as shown in Figure 4.1b. This transformed voltage source was applied to the stationary and rotating Park modelling of the flux linkage, currents, speed and torque to completely simulate the IM mathematical model done in section 3.1.

### 4.2.2 Impact assessment of ITSC faults on electromagnetic torque and rotor speed

As shown in Figure 4.2a, the electromagnetic torque of the IM at m = 0% (non-faulty IM) oscillated rapidly to its maximum value of 80. 9333Nm as the machine moves from its transient state to its steady state (where the $T_{em}$ becomes approximately 0). This behaviour is expected because IMs have high starting torque which is normally experienced during its transient state operation and the torque becomes zero when maximum speed is reached and the IM has stabilized or is operating in its steady state.

Also, as shown in Figure 4.2b, during the transient state of the machine, that is, before the torque becomes approximately 0, the rotor speed of the IM is seen to accelerate gradually to its maximum speed of 1480.4207 rpm as marked by the point "X" under no load condition. As the IM reaches stability, it maintains a steady speed of 1480.4407 rpm

(starting from the point marked "Y") of which the waveform can be seen as a pure DC waveform under no load condition in steady state operation.

The plot of the torque-speed characteristic of the IM as shown in Figure 4.3 indicates that it is operating in the motoring region (i.e., $0 < Nm < Ns$) where the source voltage is converted into mechanical energy to drive the rotor of the machine.

In the advent of 1% ITSC faults (that is, $m = 1\%$) as shown in Figure 4.4a, the electromagnetic torque behaves partially normal, maintaining the same wave pattern. However, there can be seen to be some ripples in the waveform of torque. When the machine begins to transition to its steady state from point "X" and "Y", the ripples persist as shown in the zoomed window indicating that an IM having ITSC faults experience continuous instability in the machine performance. Also, there can be seen some negative torque values of about -20 Nm in the machine as it transitions from transient to steady state.

Similarly, the rotor speed of the IM under no load ITSC faults also contains ripples during both transient and steady-state operation as shown in Figure 4.4b experiencing instability in both transient and steady-state regions.

As shown in Figure 4.5, the electromagnetic torque-speed characteristics for the IM under 1% ITSC fault shows that the IM is acting as a motor majorly however, due to the negative torque, it will force the IM to transmit power contrary to the conventional behaviour of IM.

As shown in Figure 4.6a – f and Figure 4.7a – f for 2%, 3%, 4%, 5%, 6%, and 7% respectively, the ripples in the electromagnetic torque and rotor speed increase significantly as the fault level increases in the machine under no load condition. These

show that an IM under ITSC fault will experience some irregularities in the speed and torque characteristics making it physically pulsate as it rotates and these effects increase with respect to the fault level. Comparing the points marked "X" and "Y" on each plot for each ITSC fault, it can be seen that the transient states are prolonged differently for each fault level. This shows that ITSC faults increase the transient time and delay the steady state.

For 8%, 9% and 10% ITSC faults, the ripple level of the electromagnetic torque and speed waveform as shown in Figure 4.8 and Figure 4.9 respectively becomes increasingly higher. Particularly, for the 9% and 10% ITSC faults, the IM is seen to experience a high magnitude of instability and developed an unusually negative and positive torque, which spanned through the simulation time of 3s without converging, contrarily to what is seen for the lower level of faults (less than 9% of ITSC fault). For these same fault levels, the rotor speed waveform started developing negative speed profiles with ripples. A close look at the torque-speed characteristics in Figure 4.10 for one of such fault levels (ITSC = 9%) shows that the IM is operating within the 2nd and 3rd quadrants where the machine is behaving alternatively as a prime mover and as a motor. This process is very fast, happening within microseconds, therefore, the physical behaviour of the rotor will appear to be standing still or jittering and may even produce heat signatures within the core.

### 4.2.3   Current assessments of the three-phase IM

As shown in Figure 4.11, for an IM with no ITSC fault in the stator winding, the Park currents components maintain high currents level during the transient phase and that is attributed to the effect of the high starting torque of the IM. During the steady state (marked by the region after the "X"), when the torque is approximately zero and the rotor speed is at maximum, the Park current components maintain a stable and lower current

71

level. The stationary Park current is an orthogonal two-phase AC (for a balance three-phase IM) while the rotating Park current is an orthogonal two-phase DC as shown in Figure 4.11a and 4.11b respectively.

In the advent of ITSC fault of 1%, the stationary and rotating Park currents components show some distortion and peak shift in their currents waveforms as shown in Figure 4.12. The stationary plot has a peak shift in the currents as shown in Figure 4.12a and has some distortion or AC ripples in the rotating current waveform as shown in Figure 4.12b. This is expected due to the introduction of faults in the IM. The theory of fault occurrence in an IM is that fault introduces some harmonics in the IM and using the EPVA techniques, these harmonics are seen as AC ripples in a rotating Park currents components that is conventionally a DC (Cruz and Cardoso, 2001).

As observed for the waveform of the stationary Park currents component for lower faults (1% ITSC fault in Figure 4.12b), the difference of the waveform compared to the non-faulty stationary Park currents (0% ITSC fault in Figure 4.11b) is not very visible. This is a major limitation of the stationary Park current waveform in studying faults of lower magnitude. Contrarily, when the comparison of the rotating Park currents waveform for 0% (in Figure 4.11a) and 1% (in Figure 4.12a) was made, its pure DC wave pattern for no fault began having AC ripples for as low as 1% ITSC fault. Higher ITSC faults with increased ripples are shown in Figure 4.13 and Figure 4.14 for steady-state stationary and rotating Park currents components respectively.

### 4.2.4 Visualized Park vector modulus

The EPVA technique has the advantage of diagnosing fault more clearly since it is based on diagrammatic visualization of the locus of the Park vector Modulus described in section 3.3. This technique is an online technique (that is, is implemented while the

machine is in operation to capture the relevant current data even as the machine is operational). Hence, it is expected that the transient state of the IM must have been overcome since the machine is already in operation.

As shown in Figure 4.15a, under no-fault condition (that is, ITSC fault = 0%), and without removing the transient or oscillating currents, the locus of the PVM contains multiple circular spiral patterns. Comparing the plot to a case of 1% ITSC faults as shown in Figure 4.15b, there is no clear difference between the two plots. Hence, using these raw data (without removing the transient currents or other transient harmonics) makes it difficult to use the visualized PVP to diagnose faults since it contains transient currents and transient harmonics.

When, by the means of matrix slicing, the oscillating or starting torque harmonics have been removed, the Park current components only contain steady-state current values (a state that suggests the machine is already functioning steadily before the fault occurs) and the PVP as shown in Figure 4.16a produced a perfectly circular pattern. Compared with the case of 1% ITSC fault as shown in Figure 4.16b, the deviation can be seen in the plot as a slight elliptical pattern.

The PVP for a higher level of faults become more elliptical as the fault level increases. As shown in Figure 4.17a – d, the PVP distortion is directly proportional to the degree of ITSC fault in the IM. It also shows that the size of the PVP increases as the fault level increases. This is the result of increasing short-circuit currents in the IM.

Some very unique PVP patterns begin to develop when the fault level increases to 6% and 7% as shown in Figure 18a – b respectively. The transient state begins to reappear significantly in the PVP plot. This indicates that for such a level of faults, the transient

currents have crossed the boundary point "Y" which was earlier selected as the signal point for steady-state operation.

Beyond the 8% ITSC faults, and maintaining the same simulation time and transient time, the transient currents become more in the IM and the motor is no longer operating in a steady state as shown in Figure 4.19a and Figure 4.19b. The thickness of the PVP at 9% and 10% makes it impossible to differentiate between the two.

### 4.2.5    Fault severity computation

To compute the fault severity, the mean, variance, standard deviation and RMSE of the PVM were computed as shown in Table 4.1.

The result of the computation shows that at 0% ITSC faults in the IM, the mean PVM, which measures the eccentricity of the circular pattern is 5.5620A. This value is constant as the shape of the PVP forms a perfectly circular pattern. As the percentage of the ITSC fault increases, the mean PVM begin to increase demonstrating the increase in fault current harmonic in the IM.

To know for sure if a calculated mean value of the PVM is the mean when there is no fault in the IM, the variance and the standard deviation can be used to measure that. Variance measures the extent of a deviation of a set of data from their mean values and the standard deviation measure the dispersion of a set of data from their mean values. The result shows that for 0% ITSC fault, the variance and standard deviation are 0, meaning the set of PVM data used to compute the mean are all equal and have no deviation or dispersion from each other. That accounts for the perfect circular PVP, where the PVM (which is the radius of the plot) is constant as the IM operates. But for the case of other levels of faults, the variance and standard deviation begin to vary. This confirms that the

74

PVM values have some variations and as can be seen from the PVP, the shapes are elliptical instead of the perfect circular pattern seen in the case of no fault.

The results of the variance and standard deviation validate the shape of the PVP but could not be used to finally pinpoint the exact percentage of faults within the system. As noticed from the 7% - 8% ITSC faults, these values increase rapidly and dropped lower for 9% and 10 % ITSC faults which are higher faults level. This is because variance and standard deviation only measure dispersion within the means PVM of each fault level. From the PVP shape of 9% and 10% ITSC faults shown in Figure 4.19b and c respectively, the PVM is within fairly circular patterns although the faults level and currents are high. So the system of variance and standard deviation cannot accurately compute the severity in terms of high fault currents. They only indicate that there are deviations in the PVM values and that shows the PVP plot is elliptical.

To be able to compare any scenario of ITSC fault in the IM with the original state of no ITSC fault, so as to tell the level to which the ITSC has caused the machine to deviate from the original, the RMSE values were computed. The RMSE value is used to check the errors in the PVM data at a particular fault level against the PVM datasets at 0% ITSC fault. When the data set at 0% ITSC fault were compared to each other, it shows 0, meaning there is no error in the data as well as no error in the IM at that state. However, when other values of PVM were compared with the value of PVM at 0% ITSC, the RMSE values indicate errors which increase as the fault level increase. The more the deformity of the PVP, the more the RMSE values vary indicating the level of decorrelation the PVP has from the perfect circular PVP when there is no fault.

A graph of mean PVM and RMSE versus ITSC faults is shown in Figure 4.20 under no-load conditions. This plot shows that the mean PVM and RMSE are linear and there is no

massive deviation as the fault progresses from 1% - 5% ITSC faults. The plot of RMSE is linear and fairly low up to 6% ITSC faults at "A" where it begins to show a massive difference in the values of RMSE. However, the mean PVM still maintain linearity within fair values up to 7% ITSC faults at "B" before it shows a massive difference in the mean PVM values. This shows that while the mean PVM may be within close values like points "A" and "B", the deviation in the IM is significant. What appears as not severe by the mean PVM plot is severe when the RMSE plot is considered. The RMSE plot is more sensitive to indicate points of massive differences which proves that it is more accurate to measure severity than using mean PVM values.

In Figure 4.21, under the no-load condition, the plot of variance and standard deviation versus the percentage of ITSC faults shows similarities in behaviour. With the increase in fault level, the value of variance and standard deviation maintain a fairly low linear increment up to 6% of ITSC fault at point "A". From point "A", the variance is seen to deviate massively up to point "C" at 8% ITSC faults (also, the standard deviation has its peak value at point "C") and then decline to lower values at point "D" and "E". These plots show that the variance and standard deviation do not maintain linearity throughout the considered ITSC faults (that is, 0% - 10%) and the results cannot be used to measure severity rather is best used to confirm deviation and dispersion in the PVM values.

As shown in Table 4.2, the IM mathematical model was simulated with a rated load of 5Nm load torque. This value was selected as an arbitrary value to observe any changes in the mean PVM, variance, standard deviation and RMSE values when the IM is used to drive a load. As shown in the results, under load condition of 5Nm torque, at 0% ITSC fault, the mean PVM is 6.0275A which is slightly higher than what was obtained when there is no load on the IM (that is, mean PVM at 0%, and no-load is 5.5620A in Table

76

4.1). This increased value shows that the IM draws more currents when a load is connected to it and the circumference of the PVP will be wider since it is directly proportional to the PVM values. The values of variance, standard deviation and RMSE at 0% ITSC faults are 0, which shows that there is no deviation or ITSC fault in the machine. However, the mean PVM shows the current in the IM has increased because the IM is doing more work and pulling a lot of current in driving the load. Such a higher current in the system will affect the IM more severely if an ITSC fault occurs in the IM than it would affect it when there is no load. This is shown in Figure 4.22. Using the RMSE plot, the point from which the massive deviation started is at "M" which is 5% ITSC faults under a rated load condition as compared to 6% under the no-load condition. This shows that with more current in the IM when it is driving a load, if an ITSC fault occurs, the massive breakdown is at a much lower ITSC fault. A comparison of the plots of the mean PVM and RMSE for no-load and load conditions as shown in Figure 4.24a and Figure 4.24b respectively, confirm that there is much more current in the IM during load condition, and the massive breakdown starts at a much earlier ITSC fault than what is experienced when no load is attached to the IM.

The results of this simulation with rated load clearly show that load driven by the IM affects the severity of the ITSC fault in the motor.

The plot of variance and standard deviation for the load condition is very similar to that of the no-load condition. It is linear and fairly low up to 5% ITSC fault, then, massively deviated from 5% to its peak at point "B" which is 7% before declining to point "C" at 8% ITSC fault.

In summary, in this chapter, the mathematical model of a three-phase IM was simulated with specified motor parameters and the results were presented. The IM model was

defective with ITSC fault of various percentages. The impacts of the fault on current, torque and speed characteristics were studied. It was observed that ITSC faults introduce harmonics or ripples in the current, torque and speed characteristics which completely affect the IM behaviour. To diagnose the fault, the PVP distortion was used. With PVP perfectly circular, the IM is normal, however, when the PVP is distorted the IM is faulty. To measure the level of distortion, the deviation, dispersion and correlation of the PVM corresponding to each PVP were computed. The combined results of PVP, variance, standard deviation and RMSE better help diagnose and tell the severity.

## CHAPTER FIVE

## 5.0        CONCLUSION AND RECOMMENDATION

## 5.1    Conclusions

Based on the results of this research, the following conclusions were drawn:

The mathematical equations of dynamic behaviours of an IM provided the means for the IM behaviour to be effectively studied by varying the winding properties from 0% - 10% shorten turns.

The behaviour of the IM in terms of its torque, rotor speed and winding current when subjected to different ITSC fault levels shows that the ITSC faults prolonged the transient state of the IM (or delay its steady state) from 0.7s to more than 3s, increased the torque values and created AC ripples in the torque, speed and current wave patterns.

The diagnosed ITSC faults proved that observing the shape of the visualized PVP was effective in diagnosing ITSC faults.

Fault severity in the IM measured in terms of means, variance and standard deviation of the PVM proved to be inaccurate yet confirmed there is a fault. However, the RMSE effectively compared the state where there is a fault with a state where there is no fault. The combined use of these tools (means, variance, standard deviation and RMSE) gives a more sophisticated analysis.

## 5.2    Recommendations

Based on the findings of this research, the following recommendations were made.

In this research, the ratio of shortened turns to the total number of turns was applied. Further study should be conducted to include the actual number of shortened turns in other to improve on the accuracy.

This research was based on simulation. The methodology adopted should be extended to fault diagnosis on a practical three-phase induction motor.

## 5.3    Contribution to Knowledge

This thesis has contributed the following knowledge to the field of research:

The dynamic performance of a three-phase Induction Motor was successfully modelled and simulated using SIMULINK and MATLAB environment.

The Enhanced Park Vector Approach applied enables diagnosis of inter-turn short circuit winding fault for as low as 1% shortened turns up to 10% indicating its effectiveness for faults diagnosis.

The study has established that the presence of inter-turn short circuit fault diagnosed prolonged the transient state of the Induction Motor from 0.7s to more than 3s, increased the torque values and created AC ripples in the torque, speed and current wave patterns.

## 5.4    Suggestions for Further Studies

In line with this research methodology, the following suggestions were made for further studies:

The mathematical model derived from this research was simulated under no-load and rated load torque of 5Nm. Further study could include the diagnosis of fault in an IM with variable loads conditions to study the impact of ITSC on torque, speed, current and PVP.

Machine learning EPVA-based techniques could be combined with pattern recognition features for quick and automated diagnosis of ITSC in a three-phase IM.

# REFERENCES

Afshar, M., Tabesh, A., Ebrahimi, M., & Khajehoddin, S. A. (2019). Stator short-circuit fault detection and location methods for brushless DFIMs using nested-loop rotor slot harmonics. *IEEE Transactions on Power Electronics, 35*(8), 8559-8568.

Aggarwal, A., & Strangas, E. G. (2019). Review of detection methods of static eccentricity for interior permanent magnet synchronous machine. *Energies, 12*(21), 4105.

Agyare, O. R., Asiedu-Asante, A. B., & Biney, A. R. (2019). *Fuzzy Logic Based Condition Monitoring of a 3-Phase Induction Motor.* Paper presented at the 2019 IEEE AFRICON.

Akar, M., & Gercekcioglu, H. S. (2017). Instantaneous power factor signature analysis for efficient fault diagnosis in inverter fed three phased induction motors. *International Journal of Hydrogen Energy, 42*(12), 8338-8345.

Al-Deen, K. N., Hummes, D., Fruth, B., Caironi, C., Ghaffar, A. A., & Karas, M. (2018). *Signature Analysis as a Medium for Faults Detection in Induction Motors.* Paper presented at the 2018 International Conference on Computing Sciences and Engineering (ICCSE), IEEE.

Alaoui, L. C., Drid, S., & Bouslimani, S. (2015). *An Extended Park's Vector Approach For The Detection Of Inter-Turn Faults In Induction Motor.* Paper presented at the 2015 International Conference on Automatic control, Telecommunications and Signals (ICATS15), Algeria.

Ali, M. Z., Shabbir, M. N. S. K., Liang, X., Zhang, Y., & Hu, T. (2019). Machine learning-based fault diagnosis for single-and multi-faults in induction motors using measured stator currents and vibration signals. *IEEE Transactions on Industry Applications, 55*(3), 2378-2391.

Alloui, A., Laadjal, K., Sahraoui, M., & Cardoso, A. J. M. (2022). Online Interturn Short-Circuit Fault Diagnosis in Induction Motors Operating Under Unbalanced Supply Voltage and Load Variations, Using the STLSP Technique. *IEEE Transactions on Industrial Electronics, 70*(3), 3080-3089.

AlShorman, O., Alkahatni, F., Masadeh, M., Irfan, M., Glowacz, A., Althobiani, F., . . . Glowacz, W. (2021). Sounds and acoustic emission-based early fault diagnosis of induction motor: A review study. *Advances in Mechanical Engineering, 13*(2), 1687814021996915.

Altaf, S., Mehmood, M., & Imran, M. (2018). Implementation of efficient artificial neural network data fusion classification technique for induction motor fault detection.

Amanuel, T., Ghirmay, A., Ghebremeskel, H., Ghebrehiwet, R., & Bahlibi, W. (2021). Design of Vibration Frequency Method with Fine-Tuned Factor for Fault Detection of Three Phase Induction Motor. *Journal of Innovative Image Processing, 3*(01), 52-65.

Anish Kumar, J., Jothi Swaroopan, N., & Shanker, N. (2022). Induction motor's rotor slot variation measurement using logistic regression. *Automatika, 63*(2), 288-302.

Antonino-Daviu, J., Fuster-Roig, V., Park, S., Park, Y., Choi, H., Park, J., & Lee, S. B. (2020). Electrical monitoring of damper bar condition in salient-pole synchronous motors without motor disassembly. *IEEE Transactions on Industry Applications, 56*(2), 1423-1431.

Appana, D. K., Prosvirin, A., & Kim, J.-M. (2018). Reliable fault diagnosis of bearings with varying rotational speeds using envelope spectrum and convolution neural networks. *Soft Computing, 22*(20), 6719-6729.

Arunachalam, S., & Arumugam, S. (2018). Harmonic Analysis of Fractional Order PID Controlled Induction Motor with PV Based SAF. *Journal of Electrical Engineering, 18*(4), 9-9.

Ashok, K., Li, D., Gebraeel, N., & Divan, D. (2021). Online detection of inter-turn winding faults in single-phase distribution transformers using smart meter data. *IEEE Transactions on Smart Grid, 12*(6), 5073-5083.

Beale, C., Niezrecki, C., & Inalpolat, M. (2020). An adaptive wavelet packet denoising algorithm for enhanced active acoustic damage detection from wind turbine blades. *Mechanical systems signal processing, 142*, 106754.

Bharti, S., Sinha, A., Samantaray, A., & Bhattacharyya, R. (2020). The Sommerfeld effect of second kind: passage through parametric instability in a rotor with non-circular shaft and anisotropic flexible supports. *Nonlinear Dynamics, 100*(4), 3171-3197.

Bhattacharyya, S., Sen, D., Adhvaryyu, S., & Mukherjee, C. (2015). Induction motor fault diagnosis by motor current signature analysis and neural network techniques. *Journal of Advanced Computing Communication Technologies, 3*(1), 12-18.

Bouras, A., Bouras, S., & Kerfali, S. (2018). Prediction of the mass unbalance of a variable speed induction motor by stator current multiple approaches. *gTurkish Journal of Electrical Engineering & Computer Sciences, 26*(2), 1056-1068. doi:10.3906/elk-1702-58

Burriel-Valencia, J., Puche-Panadero, R., Martinez-Roman, J., Sapena-Bano, A., & Pineda-Sanchez, M. (2017). Short-frequency Fourier transform for fault diagnosis of induction machines working in transient regime. *IEEE Transactions on Instrumentation, 66*(3), 432-440. doi:10.1109/TIM.2016.2647458

Burriel-Valencia, J., Puche-Panadero, R., Martinez-Roman, J., Sapena-Bano, A., & Pineda-Sanchez, M. (2018a). Fault Diagnosis of Induction Machines in a Transient Regime Using Current Sensors with an Optimized Slepian Window. *Sensors 18*(1). doi:10.3390/s18010146

Burriel-Valencia, J., Puche-Panadero, R., Martinez-Roman, J., Sapena-Bano, A., Pineda-Sanchez, M., Perez-Cruz, J., & Riera-Guasp, M. (2018b). Automatic fault diagnostic system for induction motors under transient regime optimized with expert systems. *Electronics, 8*(1), 6.

Chandra, D. S., & Rao, Y. S. (2019). Fault diagnosis of a double-row spherical roller bearing for induction motor using vibration monitoring technique. *Journal of Failure Analysis Prevention, 19*(4), 1144-1152.

Choqueuse, V., & Benbouzid, M. (2015). Induction machine diagnosis using stator current advanced signal processing *International Journal on Energy Conversion, 3*(3), 76–87.

Choudhary, A., Goyal, D., Shimi, S. L., & Akula, A. (2019). Condition monitoring and fault diagnosis of induction motors: A review. *Archives of Computational Methods in Engineering, 26*(4), 1221-1238.

Chouidira, I., Khodja, D. E., & Chakroune, S. (2021). Fuzzy logic based broken bar fault diagnosis and behavior study of induction machine.

Corne, B., Vervisch, B., Derammelaere, S., Knockaert, J., & Desmet, J. (2018). The reflection of evolving bearing faults in the stator current's extended park vector approach for induction machines. *Mechanical Systems Signal Processing, 107*, 168-182.

Cruz, S. M., & Cardoso, A. M. (2001). Stator winding fault diagnosis in three-phase synchronous and asynchronous motors, by the extended Park's vector approach. *IEEE Transactions on Industry Applications, 37*(5), 1227-1233.

De Sousa, P. H. F., Navar de Medeiros, M., Almeida, J. S., Rebouças Filho, P. P., & de Albuquerque, V. H. C. (2019). Intelligent incipient fault detection in wind turbines based on industrial IoT environment. *Journal of Artificial Intelligence Systems, 1*(1), 1-19.

Dongare, U. V., Umre, B. S., & Ballal, M. S. (2020). *Mathematical Modeling and Simulation of an Induction Motor with Stator Inter-Turn Faults.* Paper presented at the 2020 IEEE First International Conference on Smart Technologies for Power, Energy and Control (STPEC).

Drakaki, M., Karnavas, Y. L., Karlis, A. D., Chasiotis, I. D., & Tzionas, P. (2020). Study on fault diagnosis of broken rotor bars in squirrel cage induction motors: a multi-agent system approach using intelligent classifiers. *IET electric power applications, 14*(2), 245-255.

Faiz, J., & Moosavi, S. M. M. (2016). Eccentricity fault detection – From induction machines to DFIG—A review. *Renewable and Sustainable Energy Reviews, 55*, 169-179. doi:https://doi.org/10.1016/j.rser.2015.10.113

Farzin, N., Vakilian, M., & Hajipour, E. (2019). *Transformer Practical Turn-to-Turn Fault Detection Performance using Negative Sequence and Space Vector-Based Methods*. Paper presented at the 2019 International Conference on Protection and Automation of Power System (IPAPS), Sharif University of Technology, Tehran.

Gangsar, P., & Tiwari, R. (2017). Comparative investigation of vibration and current monitoring for prediction of mechanical and electrical faults in induction motor based on multiclass-support vector machine algorithms. *Mechanical Systems and Signal Processing, 94*, 464-481.

Gangsar, P., & Tiwari, R. (2019). Diagnostics of mechanical and electrical faults in induction motors using wavelet-based features of vibration and current through support vector machine algorithms for various operating conditions. *Journal of the Brazilian Society of Mechanical Sciences Engineering, 41*(2), 1-25.

Gangsar, P., & Tiwari, R. (2020). Signal based condition monitoring techniques for fault detection and diagnosis of induction motors: A state-of-the-art review. *Mechanical systems signal processing, 144*, 106908.

Gritli, Y., Rossi, C., Casadei, D., Filippetti, F., & Capolino, G.-A. (2017). A diagnostic space vector-based index for rotor electrical fault detection in wound-rotor induction machines under speed transient. *IEEE Transactions on Industrial Electronics, 64*(5), 3892-3902.

Gyftakis, K. N., & Cardoso, A. J. M. (2020). Reliable Detection of Stator Inter-Turn Faults of Very Low Severity Level in Induction Motors. *IEEE Transactions on Industrial Electronics*.

Gyftakis, K. N., Cardoso, A. J. M., & Antonino-Daviu, J. A. (2017). Introducing the Filtered Park's and Filtered Extended Park's Vector Approach to detect broken rotor bars in induction motors independently from the rotor slots number. *Mechanical systems signal processing, 93*, 30-50.

Gyftakis, K. N., & Cardoso, A. M. (2017). *A new space vector approach to detect stator faults in induction motors*. Paper presented at the 2017 IEEE Workshop on Electrical Machines Design, Control and Diagnosis (WEMDCD), IEEE.

Gyftakis, K. N., & Marques-Cardoso, A. J. (2019). *Reliable Detection of Very Low Severity Level Stator Inter-Turn Faults in Induction Motors*. Paper presented at the IECON 2019-45th Annual Conference of the IEEE Industrial Electronics Society, IEEE.

Gyftakis, K. N., Spyropoulos, D. V., Arvanitakis, I., Panagiotou, P. A., & Mitronikas, E. D. (2020). *Induction motors torque analysis via frequency extraction for reliable broken rotor bar detection*. Paper presented at the 2020 International Conference on Electrical Machines (ICEM), IEEE.

Gyftakis, K. N., Spyropoulos, D. V., Kappatou, J. C., & Mitronikas, E. D. (2013). A novel approach for broken bar fault diagnosis in induction motors through torque monitoring. *IEEE transactions on energy conversion, 28*(2), 267-277.

Halder, S., Bhat, S., & Dora, B. (2022). Start-up transient analysis using CWT and ridges for broken rotor bar fault diagnosis. *Electrical Engineering*, 1-12.

Hameed, A., Gul, S. T., & Khan, A. Q. (2016). *A Park's vector approach using process monitoring statistics of principal component analysis for machine fault detection*. Paper presented at the 2016 International Conference on Emerging Technologies (ICET), IEEE.

Han, Q., Ding, Z., Xu, X., Wang, T., & Chu, F. (2019). Stator current model for detecting rolling bearing faults in induction motors using magnetic equivalent circuits. *Mechanical systems signal processing, 131*, 554-575.

Hemamalini, S. (2018). Rational-Dilation Wavelet Transform Based Torque Estimation from Acoustic Signals for Fault Diagnosis in a Three-Phase Induction Motor. *IEEE Transactions on Industrial Informatics, 15*(6), 3492-3501.

Imoru, A., Nelwamondo, F., Jimoh, A.-G., & Ayodele, T. (2021). A neural network approach to detect winding faults in electrical machine. *International Journal of Emerging Electric Power Systems, 22*, 31–41. doi:10.1515/ijeeps-2020-0161

Imoru, O., Nelwamondo, F., Jimoh, A. A., & Marwala, T. (2018). *Diagnosis of Shorted-Turns Faults in Electrical Machine using Neural Network*. Paper presented at the The 26th World Congress on Engineering and Computer Science (WCECS 2018), San Francisco, USA.

Irfan, M. (2019). Modeling of fault frequencies for distributed damages in bearing raceways. *Journal of Nondestructive Evaluation, 38*(4), 1-10.

Irfan, M., Saad, N., Ibrahim, R., & Asirvadam, V. S. (2015). An on-line condition monitoring system for induction motors via instantaneous power analysis. *Journal of Mechanical Science and Technology, 29*(4), 1483-1492.

Irfan, M., Saad, N., Ibrahim, R., & Asirvadam, V. S. (2017). Condition monitoring of induction motors via instantaneous power analysis. *Journal of Intelligent Manufacturing, 28*(6), 1259-1267.

Ishkova, I., & Vítek, O. (2016). Detection and classification of faults in induction motor by means of motor current signature analysis and stray flux monitoring. *Przeglad Elektrotechniczny, 92*(4), 166-170.

Jia, F., Lei, Y., Lin, J., Zhou, X., & Lu, N. (2016). Deep neural networks: A promising tool for fault characteristic mining and intelligent diagnosis of rotating machinery with massive data. *Mechanical systems signal processing, 72*, 303-315.

Jiang, C., Li, S., & Habetler, T. G. (2017). *A review of condition monitoring of induction motors based on stray flux*. Paper presented at the 2017 IEEE Energy Conversion Congress and Exposition (ECCE).

Jung, J., Park, Y., Lee, S. B., Cho, C.-H., Kim, K., Wiedenbrug, E. J., & Teska, M. (2017). Monitoring journal-bearing faults: Making use of motor current signature analysis for induction motors. *IEEE Industry Applications Magazine, 23*(4), 12-21.

Kompella, K. D., Rao, M. V. G., & Rao, R. S. (2018). Bearing fault detection in a 3 phase induction motor using stator current frequency spectral subtraction with various wavelet decomposition techniques. *Ain Shams Engineering Journal, 9*(4), 2427-2439.

Krause, P. C., Wasynczuk, O., Sudhoff, S. D., & Pekarek, S. D. (2013). *Analysis of electric machinery and drive systems* (Vol. 75): John Wiley & Sons.

Kudelina, K., Vaimann, T., Rassõlkin, A., & Kallaste, A. (2021). *Impact of Bearing Faults on Vibration Level of BLDC Motor*. Paper presented at the IECON 2021–47th Annual Conference of the IEEE Industrial Electronics Society.

Kumar, R., Cirrincione, G., Cirrincione, M., Tortella, A., & Andriollo, M. (2018). *Induction machine fault diagnosis using stator current subspace spectral estimation.* Paper presented at the 2018 21st International Conference on Electrical Machines and Systems (ICEMS).

Lashkari, N., Poshtan, J., & Azgomi, H. F. (2015). Simulative and experimental investigation on stator winding turn and unbalanced supply voltage fault diagnosis in induction motors using artificial neural networks. *ISA transactions, 59*, 334-342.

Li, Y., Feng, K., Liang, X., & Zuo, M. J. (2019). A fault diagnosis method for planetary gearboxes under non-stationary working conditions using improved Vold-Kalman filter and multi-scale sample entropy. *Journal of Sound Vibration, 439*, 271-286.

Liu, J., & Shao, Y. (2018). Overview of dynamic modelling and analysis of rolling element bearings with localized and distributed faults. *Nonlinear Dynamics, 93*(4), 1765-1798.

Liu, Y., Chen, Z., Wang, K., & Zhai, W. (2022). Surface wear evolution of traction motor bearings in vibration environment of a locomotive during operation. *Science China Technological Sciences, 65*(4), 920-931.

Liu, Z., Wang, X., & Zhang, L. (2020). Fault diagnosis of industrial wind turbine blade bearing using acoustic emission analysis. *IEEE Transactions on Instrumentation Measurement, 69*(9), 6630-6639.

Malla, C., & Panigrahi, I. (2019). Review of condition monitoring of rolling element bearing using vibration analysis and other techniques. *Journal of Vibration Engineering Technologies, 7*(4), 407-414.

Mani, S., Kafil, M., & Ahmadi, H. (2021). Implementation of Instantaneous Power Spectrum Analysis for Diagnosis of Three-Phase Induction Motor Faults Under Mechanical Load Oscillations; Case Study of Mobarakeh Steel Company, Iran. In *Advances in Condition Monitoring and Structural Health Monitoring* (pp. 415-428). Springer: Singapore.

Maraaba, L., Al-Hamouz, Z., & Abido, M. (2018). An efficient stator inter-turn fault diagnosis tool for induction motors. *Energies, 11*(3), 653.

Marzebali, M. H., Faiz, J., Capolino, G.-A., Kia, S. H., & Henao, H. (2018). Planetary gear fault detection based on mechanical torque and stator current signatures of a wound rotor induction generator. *IEEE transactions on energy conversion, 33*(3), 1072-1085.

Meira, M., Ruschetti, C. R., Álvarez, R. E., & Verucchi, C. J. (2018). Power transformers monitoring based on electrical measurements: state of the art. *IET Generation, Transmission and Distribution, 12*(12), 2805-2815.

Mirzaeva, G., & Saad, K. I. (2018). Advanced diagnosis of stator turn-to-turn faults and static eccentricity in induction motors based on internal flux measurement. *IEEE Transactions on Industry Applications, 54*(4), 3961-3970.

Mohamed, M. A., Hassan, M. A. M., Albalawi, F., Ghoneim, S. S., Ali, Z. M., & Dardeer, M. (2021). Diagnostic Modelling for Induction Motor Faults via ANFIS Algorithm and DWT-Based Feature Extraction. *Applied Sciences, 11*(19), 9115.

Mostafaei, M., Faiz, J., Venikar, P. A., & Ballal, M. S. (2018). Turn- to- turn fault monitoring methods in electrical power transformers—State of the art. *International Transactions on Electrical Energy Systems, 28*(12), e2644.

Mustafa, M. O. (2015). *On fault detection, diagnosis and monitoring for induction motors.* Luleå tekniska universitet,

Nandi, S., Toliyat, H. A., & Li, X. (2005). Condition monitoring and fault diagnosis of electrical motors—A review. *IEEE transactions on energy conversion, 20*(4), 719-729.

Nath, A. G., Udmale, S. S., & Singh, S. K. (2021). Role of artificial intelligence in rotor fault diagnosis: A comprehensive review. *Artificial Intelligence Review, 54*(4), 2609-2668.

Oliveira, L. M., & Cardoso, A. J. M. (2016). Comparing power transformer turn-to-turn faults protection methods: negative sequence component versus space-vector algorithms. *IEEE Transactions on Industry Applications, 53*(3), 2817-2825.

Önel, I. Y., & Benbouzid, M. E. H. (2008). Induction motor bearing failure detection and diagnosis: Park and concordia transform approaches comparative study. *IEEE/ASME Transactions on mechatronics, 13*(2), 257-262.

Ostachowicz, W., Soman, R., & Malinowski, P. (2019). Optimization of sensor placement for structural health monitoring: A review. *Structural Health Monitoring, 18*(3), 963-988.

Ozigis, I., Oche, J., & Lawal, N. (2021). Locomotive engines and the future of railway automotive power in Africa: A review. *Nigerian Journal of Technology, 40*(4), 660-673.

Panagiotou, P., Arvanitakis, I., Lophitis, N., Antonino-Daviu, J. A., & Gyftakis, K. N. (2018). *Analysis of stray flux spectral components in induction machines under rotor bar breakages at various locations*. Paper presented at the 2018 XIII International Conference on Electrical Machines (ICEM), IEEE, Alexandroupoli, Greece.

Pezzani, C., Donolo, P., Castellino, A., Bossio, G., & De Angelo, C. (2010). *A new approach to the Park's vector for broken bars and load oscillation diagnosis on IM*. Paper presented at the 2010 IEEE International Conference on Industrial Technology, IEEE.

Pietrzak, P., & Wolkiewicz, M. (2021a). *Application of Support Vector Machine to stator winding fault detection and classification of permanent magnet synchronous motor.* Paper presented at the 2021 IEEE 19th International Power Electronics and Motion Control Conference (PEMC).

Pietrzak, P., & Wolkiewicz, M. (2021b). Comparison of selected methods for the stator winding condition monitoring of a PMSM using the stator phase currents. *Energies, 14*(6), 1630.

Poddar, S., & Tandon, N. (2019). Detection of particle contamination in journal bearing using acoustic emission and vibration monitoring techniques. *Tribology international, 134*, 154-164.

Quabeck, S., Shangguan, W., Scharfenstein, D., & De Doncker, R. W. (2021). Detection of broken rotor bars in induction machines using machine learning methods. *IEEJ Journal of Industry Applications*, 21000651.

Ramirez-Nunez, J. A., Antonino-Daviu, J. A., Climente-Alarcón, V., Quijano-López, A., Razik, H., Osornio-Rios, R. A., & Romero-Troncoso, R. D. J. (2018). Evaluation of the detectability of electromechanical faults in induction motors via transient analysis of the stray flux. *IEEE Transactions on Industry Applications, 54*(5), 4324-4332.

Ratnani, P. L., & Thosar, A. (2014). Mathematical modelling of an 3 phase induction motor using MATLAB/Simulink. *International Journal Of Modern Engineering Research, 4*(6), 62-67.

Razavi-Far, R., Hallaji, E., Farajzadeh-Zanjani, M., Saif, M., Kia, S. H., Henao, H., & Capolino, G. A. (2018). Information fusion and semi-supervised deep learning scheme for diagnosing gear faults in induction machine systems. *IEEE Transactions on Industrial Electronics, 66*(8), 6331-6342.

Sadeghi, I., Ehya, H., & Faiz, J. (2017). *Eccentricity fault indices in large induction motors an overview*. Paper presented at the 2017 8th Power Electronics, Drive Systems & Technologies Conference (PEDSTC), IEEE.

Salameh, J. P., Cauet, S., Etien, E., Sakout, A., & Rambault, L. (2018). Gearbox condition monitoring in wind turbines: A review. *Mechanical systems signal processing, 111*, 251-264.

Samir, H., Omar, T., & Rachid, I. (2008). Generalized two axes model of a squirrel-cage induction motor for rotor fault diagnosis. *Serbian journal of electrical engineering, 5*(1), 155-170.

Sang-Hoon, K. (2017). Modeling of Alternating Current Motors and Reference Frame Theory. *Electric Motor Control*.

Sapena-Bano, A., Martinez-Roman, J., Puche-Panadero, R., Pineda-Sanchez, M., Perez-Cruz, J., & Riera-Guasp, M. (2018). Induction machine model with space harmonics for fault diagnosis based on the convolution theorem. *International Journal of Electrical Power & Energy Systems, 100*, 463-481.

Sapena-Bano, A., Pineda-Sanchez, M., Puche-Panadero, R., Perez-Cruz, J., Roger-Folch, J., Riera-Guasp, M., & Martinez-Roman, J. (2015). Harmonic order tracking analysis: A novel method for fault diagnosis in induction machines. *IEEE transactions on energy conversion, 30*(3), 833-841.

Sapena-Bano, A., Riera-Guasp, M., Puche-Panadero, R., Martinez-Roman, J., Perez-Cruz, J., & Pineda-Sanchez, M. (2016). Harmonic order tracking analysis: A speed-sensorless method for condition monitoring of wound rotor induction generators. *IEEE Transactions on Industry Applications, 52*(6), 4719-4729.

Sarikaya, T., Polat, A., & Ergene, L. (2019). *Diagnosis of Different Eccentricity Faults in Induction Motors Based on Electrical and Magnetic Signatures and Unbalanced Magnetic Pull.* Paper presented at the 2019 International Aegean Conference on Electrical Machines and Power Electronics (ACEMP) & 2019 International Conference on Optimization of Electrical and Electronic Equipment (OPTIM).

Sharma, A., Chatterji, S., & Mathew, L. (2017). *A novel Park's Vector Approach for Investigation of Incipient Stator Fault Using MCSA in Three-Phase Induction Motors.* Paper presented at the 2017 International Conference on Innovations in Control, Communication and Information Systems (ICICCI), IEEE.

Sharma, A., Verma, P., Mathew, L., & Chatterji, S. (2018). *Using motor current analysis for broken rotor bar fault detection in rotary machines.* Paper presented at the 2018 3rd International Conference on Communication and Electronics Systems (ICCES).

Sheikh, M. A., Bakhsh, S. T., Irfan, M., Nor, N. b. M., & Nowakowski, G. (2022). A Review to Diagnose Faults Related to Three-Phase Industrial Induction Motors. *Journal of Failure Analysis Prevention, 22*(4), 1546-1557.

Shin, J., Park, Y., & Lee, S. B. (2021). Flux-based detection and classification of induction motor eccentricity, rotor cage, and load defects. *IEEE Transactions on Industry Applications, 57*(3), 2471-2480.

Singh, A. K. (2019). *Condition Monitoring and Fault Diagnosis Techniques of Electric Machines.* Paper presented at the 2019 3rd International Conference on Recent Developments in Control, Automation & Power Engineering (RDCAPE).

Stief, A., Ottewill, J. R., Baranowski, J., & Orkisz, M. (2019). A PCA and two-stage Bayesian sensor fusion approach for diagnosing electrical and mechanical faults in induction motors. *IEEE Transactions on Industrial Electronics, 66*(12), 9510-9520.

Sunal, C. E., Dyo, V., & Velisavljevic, V. (2022). Review of machine learning based fault detection for centrifugal pump induction motors. *IEEE Access, 10*, 71344-71355.

Tallam, R. M., Habetler, T. G., & Harley, R. G. (2002). Transient model for induction machines with stator winding turn faults. *IEEE Transactions on Industry Applications, 38*(3), 632-637.

Tavner, P. (2008). Review of condition monitoring of rotating electrical machines. *IET electric power applications, 2*(4), 215-247.

Verma, A. K., Radhika, S., & Padmanabhan, S. V. (2018). *Wavelet based fault detection and diagnosis using online mcsa of stator winding faults due to insulation failure*

*in industrial induction machine.* Paper presented at the 2018 IEEE Recent Advances in Intelligent Computational Systems (RAICS).

Wang, T., Han, Q., Chu, F., & Feng, Z. (2019). Vibration based condition monitoring and fault diagnosis of wind turbine planetary gearbox: A review. *Mechanical systems signal processing, 126*, 662-685.

Wang, Z., Yao, L., & Cai, Y. (2020). Rolling bearing fault diagnosis using generalized refined composite multiscale sample entropy and optimized support vector machine. *Measurement, 156*, 107574.

Wen, L., Li, X., Gao, L., & Zhang, Y. (2017). A new convolutional neural network-based data-driven fault diagnosis method. *IEEE Transactions on Industrial Electronics, 65*(7), 5990-5998.

Yadav, O. P., Joshi, D., & Pahuja, G. (2013). Support Vector Machine based Bearing Fault Detection of Induction Motor. *1*, 34-39.

Yang, Z., Shang, F., Brown, I. P., & Krishnamurthy, M. (2015). Comparative study of interior permanent magnet, induction, and switched reluctance motor drives for EV and HEV applications. *IEEE Transactions on Transportation Electrification, 1*(3), 245-254.

Zhang, P., Du, Y., Habetler, T. G., & Lu, B. (2011). A Survey of Condition Monitoring and Protection Methods for Medium-Voltage Induction Motors. *IEEE Transactions on Industry Applications, 47(1)*, 34–46. doi:10.1109/tia.2010.2090839

APPENDIX A

M-FILE FOR PLOTTING TORQUE, SPEED AND TORQUE-SPEED

CHARACTERISTICS

```
%% CLEAR COMMAND WINDOW AND FIGURES

clc; clf;

%% EXTRACT TORQUE AND SPEED TIMESERIES DATA at m = 0% ITSC Fault

torque_m0 = out.get('Torque');      % m = 0%

speed_m0 = out.get('speed');        % m = 0%

%% PLOT THE GRAPH OF TORQUE AND SPEED

suplot(2,1,1);                 %plot on row 1

plot(torque_m0);               %plot torque at m = 0%

hold on;

xline(0.5851, '--');           %transient state at X

hold on;

xline(0.7, '--');              %transient state at Y

ylim([0,120]);                 %set y-axis range values

xlim([0,1]);                   %set x-axis range values

ylabel('Torque (N.m)');        %set y-axis label

xlabel('Time (seconds)');      %set x-axis label


subplot(2,1,2);                %plot on row 2

plot(speed_m0);                %plot torque at m = 0%

hold on;

xline(0.5851, '--');           %transient state at X

hold on;
```

```matlab
xline(0.7, '--');              %transient state at Y

ylim([0,1600]);                %set y-axis range values

xlim([0,1]);                   %set x-axis range values

ylabel('Speed (rpm)');         %set y-axis label

xlabel('Time (seconds)');      %set x-axis label


%Simulate the IM Model for m = 1, 2, 3,...,10% ITSC

%change X in torque_mX and speed_mX, where X = each value of m

%Repeat this code for each value of m


%% PLOT TORQUE-SPEED CHARACTERISTICS

% Comment the upper subplot and uncomment this code

% plot(speed_m0.XData, torque_m0.XData); %torque-speed Xteristic at m = 0%

% xlim([0,1600]);

% ylim([0,120]);

% xlabel('Speed (rpm)');

% ylabel('Torque (N.m)');

%% SAVE TORQUE and SPEED DATA

% after running the code for m = 10%, uncomment and run the code to save

% torque = [torque_m0, torque_m1, torque_m2, torque_m3, torque_m4, torque_m5,

torque_m6, torque_m7, torque_m8, torque_m9, torque_m10];

% speed = [speed_m0, speed_m1, speed_m2, speed_m3, speed_m4, speed_m5,

speed_m6, speed_m7, speed_m8, speed_m9, speed_m10];

% save('speed_torque.mat', 'torque', 'speed');
```

# APPENDIX B

## M-FILE FOR PLOTTING STATIONARY AND ROTATING PARK CURRENTS

```matlab
%% CLEAR COMMAND WINDOW AND FIGURE

clc; clf;

%% EXTRACT STATIONARY PARK CURRENT COMPONENTS

Idqss_m0 = out.get('Idqss');

%% EXTRACT ROTATING PARK CURRENT COMPONENTS

Idqs_m0 = out.get('Idqs');

%% EXTRACT SIMULATION TIME

t = out.get('tout');

%% PLOT STATIONARY PARK CURRENTS

subplot(2,1,1);                                     %plot on row 1

plot(t, Idqss_m0);                                  %plot at m = 0%

ylim([0,120]);                                      %set y limit

xlim([0,1]);                                        %set x limit

hold on;

xline(0.5851, '--');                                %mark X point

hold on;

xline(0.7, '--');                                   %mark Y point

xlabel('Simulation Time (seconds)');                %x label

ylabel('Stator Currents in αβ Reference Frame (A)'); %y label

 %% PLOT ROTATING PARK CURRENTS

subplot(2,1,1);                                     %plot on row 1

plot(t, Idqs_m0);                                   %plot at m = 0%

ylim([0,120]);                                      %set y limit
```

94

```matlab
xlim([0,1]);                                        %set x limit

hold on;

xline(0.5851, '--');                                %mark X point

hold on;

xline(0.7, '--');                                   %mark Y point

xlabel('Simulation Time (seconds)');                %x label

ylabel('Stator Currents in DQ Reference Frame (A)');  %y label


%Simulate the IM Model for m = 1,2,3,...,10% ITSC

%change X in Idqss_mX and Idqs_mX, where X = each value of m

%Repeat this code for each value of m

%% SAVE STATIONARY and ROTATING PARK CURRENTS

% after running the code for m = 10%, uncomment this code and run the code to save

the %variables

% Idqss = [Idqss_m0, Idqss_m1, Idqss_m2, Idqss_m3, Idqss_m4, Idqss_m5, Idqss_m6,

Idqss_m7, Idqss_m8, Idqss_m9, Idqss_m10];

% Idqs = [Idqs_m0, Idqs_m1, Idqs_m2, Idqs_m3, Idqs_m4, Idqs_m5, Idqs_m6,

Idqs_m7, Idqs_m8, Idqs_m9, Idqs_m10];

% save('park_currents.mat', 'Idqss', 'Idqs', 't');
```

# APPENDIX C

## M-FILE FOR EXTRACTING AND PLOTTING STEADY-STATE STATIONARY AND ROTATING PARK CURRENTS

```
%% CLEAR COMMAND WINDOW, FIGURE, VARIABLES

clc; clf; clear;

%% LOAD PARK CURRENT DATA

load park_currents.mat;

%% EXTRACT THE STEADY STATE CURRENT AT 0.7SECS

s_Idqss = Idqss(7000:end, :);  %steady-state stationary Park current at 0.7sec

s_Idqs = Idqs(7000:end, :);    %steady-state rotating Park current at 0.7sec

ts = t(7000:end, :);           %steady time

%% MULTIPLE PLOT OF ALPHA_BETA CURRENTS

row = 5; cols = 2; j=1;

r = 1; c = 3;

figure(1);                     %save this plot as Figure (1)

for x=1:4

   subplot(row,cols,j);

   plot(ts,s_Idqss(:,r:c));

   ylim([-15,15]);

   xlim([0.7,1]);

   j=j+2;

   r=r+3;

   c=c+3;

   hold on;

end
```

```matlab
j=2;

for x=1:4

    subplot(row,cols,j);

    plot(ts,s_Idqss(:,r:c));

    ylim([-15,15]);

    xlim([0.7,1]);

    j=j+2;

    r=r+3;

    c=c+3;

end

xlabel('Time (seconds)');

ylabel('Stator Currents in αβ (A)');

%% MULTIPLE PLOTS OF THE ROTATING PARK CURRENT

row = 5; cols = 2; j=1;

r = 1; c = 2;

figure(2);                %save this plot as Figure (2)

for x=1:4

    subplot(row,cols,j);

    plot(ts,s_Idqs(:,r:c));

    ylim([-15, 15]);

    xlim([0.7, 1]);

    j=j+2;

    r=r+3;

    c=c+3;

    hold on;
```

```
end

j=2;

for x=1:4

    subplot(row,cols,j);

    plot(ts,s_Idqs(:,r:c));

    ylim([-15, 15]);

    xlim([0.7, 1]);

    j=j+2;

    r=r+3;

    c=c+3;

end

xlabel('Time (seconds)');

ylabel('Stator Currents in dq0 (A)');

%% SAVE THE STEADY-STATE CURRENTS

save('steady_state_current.mat', 's_Idqss', 's_Idqs');
```

# APPENDIX D

## M-FILE FOR PLOTTING PVP, COMPUTING PVM, MEAN, VARIANCE, STANDARD DEVIATION, AND RMSE

```
%% CLEAR COMMAND WINDOW, VARIABLES, FIGURES

clc; clear; clf;

%% LOAD STEADY-STATE CURRENT DATA

load steady_state_current.mat;

%% EXTRACT stationary current at m = 0;

r = 1; c = 2;                      %set the columns for Idss and Iqss respectively

s_Idss_m0 = s_Idqss(:,r);          %extract steady-state Idss at m = 0

s_Iqss_m0 = s_Idqss(:,c);          %extract steady-state Iqss at m = 0

%% PLOT THE PARK VECTOR PLOT (PVP) at m = 0%

plot(s_Idss_m0, s_Iqss_m0);

hold on

plot(0,0, '+')                     %plot a zero origin

xlim([-15, 15]);                   %set x limit

ylim([-15, 15]);                   %set y limit

xlabel('Stator Stationary d-Current (Idss) in Ampere (A)');

ylabel('Stator Stationary q-Current (Iqss) in Ampere (A)');

%% CALC. PVM at m = 0

[theta, PVM_m0] = cart2pol(s_Idss_m0, s_Iqss_m0);

meanPVM = mean(PVM_m0);            %calculate mean

varPVM = var(PVM_m0);             %calculate variance

stdPVM = std(PVM_m0);            %calculate standard deviation

RMSE = sqrt(mean((PVM_m0-PVM_m0).^2));  %Calculate RMSE
```

%Simulate the IM Model for m = 1,2,3,....,10% ITSC

%change X in torque_mX and speed_mX, where X = each value of m

%increment r and c by 3 for each value of m

%except for RMSE at m = 1, RMSE = sqrt(mean((PVM_m1-PVM_m0).^2));

%Repeat this code for each value of m